Alexey Sharov, Dr. techn.

Dynamical behaviour of solar convection over an activity cycle

MASTER'S THESIS

to achieve the university degree of

Diplom-Ingeneur

Master's degree programme: Space Sciences and Earth from Space

Submitted to

Graz University of Technology

Supervisor

Univ.-Prof. Dr.phil. Arnold Hanslmeier

University of Graz, Institute of Physics

Department of Geophysics, Astrophysics and Meteorology

Graz, March, 2020

Affidavit

I declare that I have authored this thesis independently, that I have not used other than the declared sources/resources, and that I have explicitly indicated all material which has been quoted either literally or by content from the sources used. The text document uploaded to TUGRAZonline is identical to the present master‘s thesis.

Date	Signature

Table of Contents

Annex

Abstract

The present thesis deals with the investigation of solar surface convection and the variability of solar granulation over a cycle of solar activity. The unprecedented series of space-borne imagery taken by the Hinode Solar Optical Telescope in 2006 - 2016 and the time series of daily sunspot numbers (SSN) from the Royal Observatory of Belgium have provided a solid experimental basis and factual material for initial theoretical and comprehensive empirical studies of the dynamic behaviour of solar granulation in relation to sunspot activity.

An initial theoretical study based on the mixing-length theory was carried out and the first analytical formulations showing the inverse proportionality between the local flux of the convective energy and the granular size were written and discussed. The definitions of granules and granular cells in solar surface convection were critically reviewed, and the use of granular cells for morphometric measurements was preferred. Further research focussed on the development of an efficient algorithm for the automatic identification of granular cells in Hinode images, its implementation and practical application to the precise morphometric measurements and the temporal cross-correlation analysis of the results with the SSN time series.

An effectual marker-controlled watershed (MCW) algorithm for the automatic segmentation and identification of granules and granular cells in the Hinode imagery was designed, implemented, tested and practically applied to the granulation measurements and analyses. In the course of the study, the execution time for a Hinode full-frame image was reduced from 15 to 2.5 seconds. The processing efficiency of the WCM method was tested and rated as superior to other working analogues for the photometric segmentation of solar granulation images.

A total of 7 image sequences with 30-, 27- and 1-day cadence, which all contained 710 high-resolution Hinode images, were compiled, homogenized, processed and corrected for the variable Sun-Earth distance. The resultant granulation parameters, including mean area, perimeter, equivalent diameter, and contrast were analysed, validated and compared to monthly and daily sunspot numbers using methods of statistical control and cross-correlation analysis. The typical size of granules was measured at 1.37 arcseconds or 995 km on the solar surface, while the mean equivalent diameter of granular cells was given as 2.06 arcseconds or 1495 km, which was in good agreement with the results of other researchers.

The existence of a statistically significant temporal correlation between the solar granulation scale and the SSN index over the entire 10-year Hinode operation period could not be determined due to variable instrumental effects and heterogeneous quality of the long-term Hinode image series. Instead, an essential anti-correlation was measured between the mean size of granular cells and the daily SSN for the shorter time intervals of four months, which were characterized with the optimal orbital conditions for the imaging of solar granulation.

Herewith, an important scientific question regarding the inverse relationship between the granulation scale and sunspot numbers was positively resolved. The approximately 14-day delay in the cause-effect relationship between the SSN and the granulation scale was revealed with the cross-correlation analysis and a plausible explanation for this delay was given. New in-depth knowledge about the solar surface convection and the dynamic behaviour of solar granulation over an activity cycle was summarized, documented and presented in the form of the present master's thesis.

Kurzfassung

Die vorliegende Arbeit befasst sich mit der Untersuchung der Konvektion auf der Sonnenoberfläche und der Variabilität der Sonnengranulation über einen Zyklus der Sonnenaktivität. Die beispiellose Reihe von Weltraumbildern, die das Hinode Solar Optical Telescope von 2006 bis 2016 aufgenommen hat und die Zeitreihen der täglichen Sonnenfleckenzahlen (SSN) des Königlichen Observatoriums von Belgien dienten als eine solide experimentelle Grundlage und als Faktenmaterial für erste theoretische und umfassende empirische Untersuchungen des dynamischen Verhalten der Sonnengranulation in Bezug auf die Sonnenfleckenaktivität.

Eine kurze theoretische Studie basierend auf der Mischlängentheorie wurde durchgeführt und die ersten analytischen Formulierungen, die die inverse Proportionalität zwischen dem lokalen Fluss der konvektiven Energie und der Granulargröße zeigen, wurden geschrieben und diskutiert. Die Definitionen von Granula und Granularzellen in der Konvektion auf der Sonnenoberfläche wurden kritisch überprüft, und die Verwendung von Granularzellen für morphometrische Messungen wurde bevorzugt. Weitere Forschung konzentrierten sich auf die Entwicklung eines effizienten Algorithmus zur automatischen Identifizierung von Granularzellen in Hinode-Bildern, dessen Implementierung und praktische Anwendung für präzise morphometrische Messungen und die zeitliche Kreuzkorrelationsanalyse der Ergebnisse mit den SSN-Zeitreihen.

Ein effektiver markergesteuerter Wassereinzugsgebietsalgorithmus (MCW) zur automatischen Segmentierung und Identifizierung von Granules und Granularzellen in den Hinode-Bildern wurde entworfen, implementiert, getestet und praktisch auf die granulometrischen Messungen und Analysen angewendet. Im Verlauf der Studie wurde die Ausführungszeit für ein Hinode-Vollbild von 15 auf 2,5 Sekunden reduziert. Die Verarbeitungseffizienz der WCW-Methode wurde getestet und anderen Arbeitsanaloga für die photometrische Segmentierung von Sonnengranulationsbildern als überlegen eingestuft.

Insgesamt 7 Bildsequenzen mit einer Aufnahmefrequenz von 30, 27 und 1 Tag, die 710 hochauflösende Hinode-Bilder enthielten, wurden zusammengestellt, homogenisiert, verarbeitet und um den variablen Abstand zwischen Sonne und Erde korrigiert. Die resultierenden Granulationsparameter, einschließlich der mittleren Fläche, des Umfangs, des äquivalenten Durchmessers und des Kontrasts, wurden analysiert, validiert und mit monatlichen und täglichen Sonnenfleckenzahlen unter Verwendung von Methoden der statistischen Kontrolle und Kreuzkorrelationsanalyse verglichen. Die typische Größe von Granula wurde bei 1,37 Bogensekunden oder 995 km auf der Sonnenoberfläche gemessen, während der mittlere äquivalente Durchmesser von Granularzellen mit 2,06 Bogensekunden oder 1495 km angegeben wurde, was gut mit den Ergebnissen anderer Forscher übereinstimmte.

Das Vorhandensein einer statistisch signifikanten zeitlichen Korrelation zwischen der Sonnengranulationsskala und dem SSN-Index über den gesamten 10-jährigen Hinode-Betriebszeitraum konnte aufgrund variabler instrumenteller Effekte und heterogener Qualität der langfristigen Hinode-Bildserien nicht festgestellt werden. Stattdessen wurde eine wesentliche inverse Korrelation zwischen der mittleren Größe der Granulationszellen und der täglichen SSN für die kürzeren Zeitintervalle von vier Monaten gemessen, die mit den optimalen Umlaufbedingungen für die Abbildung der Sonnengranulation charakterisiert wurden.

Hiermit wurde eine wichtige wissenschaftliche Frage bezüglich der umgekehrten Beziehung zwischen der Granulationsskala und den Sonnenfleckenzahlen positiv gelöst. Die etwa 14-tägige Verzögerung der Ursache-Wirkungs-Beziehung zwischen der SSN und der Granulationsskala wurde mit der Korrelationsanalyse aufgedeckt und eine plausible Erklärung für diese Verzögerung gegeben. In der vorliegenden Masterarbeit wurden neue fundierte Kenntnisse über die Konvektion auf der Sonnenoberfläche und das dynamische Verhalten der Sonnengranulation über einen Aktivitätszyklus zusammengefasst, dokumentiert und präsentiert.

Acknowledgements

The results of all long-term efforts undertaken for this study and included in this thesis could not be obtained by one person alone. They required the beliefs, hopes, thoughts and actions of an entire group of persons of different ages, professions and social status. It is therefore a great pleasure to personally name all the people who have kindly supported me in preparing and completing this work.

First of all I would like to warmly thank Professor Arnold Hanslmeier from the Institute of Geophysics, Astrophysics and Meteorology (IGAM), University of Graz for introducing me into the topic of solar physics and acting as my supervisor and whom I consider to be one of the best teachers in my life. The Hinode* scenes that he generously made available to me for the empirical work were the most remarkable, amazing and fascinating scientific pictures I have ever seen. Sincere interest and curiosity, which were awakened with these images, were the main drivers for the present study. All the useful training, memorable deliberations, critical comments and valuable advices that I have received from all colleagues in the Astrophysical Department of IGAM are greately appreciated.

I am very thankful to Prof. M.Schardt and Dr. H.Mayer, my direct superiors at the Institute for Inormation and Communication Technologies (DIGITAL), Joanneum Research in Graz who enabled me to complete my studies in “Space Sciences” and tolerated some delays in the implementation of my main research work at the Institute. I would also like to thank Dipl.Ing. M.Schneeberger from the same institute, who helped me a lot with the algorithmic design and optimization of the SOGIS software for the automatic segmentation of solar granulation in numerous Hinode images. The software's high processing efficiency was largely achieved thanks to his advices and corrections. He is a real guru in software engineering.

I was especially impressed by the long-term technical and mental support provided by Amtsrat Ing. W.Krämer, head of the Data Centre at the Institute of Geodesy, Graz University of Technology. He coordinated my daily work in the data centre, including weekends, to my complete satisfaction. I am happy to count him as a faithful friend.

The importance of statistical methods for the granulometric processing of Hinode image time series is undeniable, and the knowledge and skills derived from the course "Statistical Methods for Processing Data Time Series" given at the TU Graz by Dr. C.Lothka were very useful. Dr. H.Ganster, Dr. R.Perko, DI. J-P.Andreu, DI. H.Gallaun, MSc. P.Miletich, Bakk. G.Jakob and Ing. A.Wimmer from Joanneum Research, who took part in numerous discussions about solar granulation and surface convection during our coffee breaks and encouraged me to complete this study, are kindly acknowldeged. The last, but most hearty thanks are addressed to all members of my family, my wife Tatiana, my sons Nikita and Roman, my daughter Eugenia, my son-in-law Thomas and my little grandson Yuriy, who each supported me in this work in their own way. Thank you so much!

*) Hinode is a joint Japan/US/UK satellite solar observatory led by the Japanese Aerospace Exploration Agency’s (JAXA). Daily and monthly mean time series of sunspot numbers (SSN) for the period of Hinode operation in 1996 – 2016 were derived from the SILSO archive of the World Data Centre for SSN at the Royal Observatory of Belgium. The implementation of segmentation algorithm was done using the MATLAB numerical computing environment and programming language v.2017b. The entire data processing was carried out using a student PC No. 9 in the TUG Data Centre in Steyrergasse 30, 8010 Graz.

"The source of solar activity is the magnetic field. The source of the magnetic field is not known"
(D.Gough 2000)

Introduction

0.1 Problematics

In modern heliophysics, there are three arduous scientific problems related to solar surface convection: the problem of radiation boundary and radiative cooling at the sun's surface as the main mechanism that controls solar convection, the problem of strong stratification in the uppermost layer of the convection zone and the problem of convection cyclicity[1] in relation to the solar activity cycle (Hanslmeier 2007). The latter problem is addressed in the present study.

Thermal convection and radiation are two principal constituents of the solar activity. The dynamic balance and interplay between these two energy transfer processes are expressed at the solar surface in the form of photospheric granulation. The study of photospheric granulation is therefore of fundamental importance for a better understanding of both the behaviour of solar surface convection and the mechanism of the solar photospheric radiation.

Properties of solar surface convection and granulation can be related to magnetohydrodynamic processes in solar interiors. Solar magnetism is not a main cause of photospheric granulation, however. Numerical simulations of solar granulation show that the granular pattern is mainly a surface phenomenon driven by effective radiative cooling in the photosphere (Nordlund 2009).

Solar granulation is a widespread, directly observable convection pattern that, apart from sunspots, occupies the entire surface of the Sun. Fluctuations of the horizontal size and optical contrast of solar granulation can be directly observed, precisely measured, statistically parameterized and related to indices of solar activity. 35 years ago a scientific hypothesis was devised that the size of solar granulation varies with solar magnetic activity and can therefore serve as an indicator of this activity (Macris et al. 1984, Muller & Roudier 1984). Since then, this hypothesis was neither ultimately proved nor negated.

Traditionally, solar magnetic activity is characterized by daily sunspot numbers (SSN), which have been recorded regularly for over 200 years. Accordingly, numerous studies have been carried out that focussed on determining the cause-and-effect relationship between the SSN and granulation parameters, yet without definitive success (Hanslmeier et al 2010).

The latest granulometric study by (Muller et al. 2018) using seeing-free image series obtained in the blue continuum channel (450.45 nm) from the 50-cm Hinode optical telescope with a consistent angular resolution of 0.2 '', i.e. near the diffraction limit, also could not come to a decisive conclusion about the existence of the long-term relationship between the variability of the granulation scale and/or contrast and the sunspot activity. Various instrumental effects, including orbital, thermal, mechanical and optoelectronic impacts on the long-term quality and homogeneity of the Hinode image time series were noted as the main factors that make it

[1] Cyclicity is the quality or state of something that occurs or moves in cycles (Webster's Dictionary 2019).

difficult to identify such a relationship, and it was concluded that “the variation of photospheric granulation related to 11-year solar cycle remains an open issue”.

Indeed, the search for the relationship between solar surface convection and magnetic activity is not easy, both theoretically and empirically, because it involves a variety of processes and interactions that are complex and indirect. The use of the SSN index for correlation studies regarding solar convection activity is subject to a fundamental restriction. During long periods of minimal activity in the solar cycle, the SSN index often reaches zero values and no correlation analysis between the granulation parameters and SSN is possible. At maximum activity, the occurrence of numerous sunspots and pores essentially influences the photometric quality of granulation images, which means that the corresponding images have to be excluded from the analysis. This causes data gaps and makes image time series irregular.

Moreover, the distortion of the granulation shape in magnetically active areas on the solar surface brings about additional difficulties in the granulometric analysis. Fortunately, in the quiet-sun area at the disk centre, the influence of magnetic fields on the granulation pattern can be neglected (Hanslmeier et al. 2009). Therefore, the research concept of the present study is to investigate the variability of granulation parameters in quiet-sun region at the solar disk centre over seasons with medium solar activity. Granulometric analysis of quiet-sun images represents a unique situation in which almost all image details are relevant for the analysis.

The unprecedented series of almost 4000 space-borne images taken by the Hinode Solar Optical Telescope in 2006 - 2016 and the time series of daily sunspot numbers from the Royal Observatory of Belgium have constituted the comprehensive experimental data set for studying the dynamic behaviour of solar granulation in relation to sunspot activity. When asked by Prof. Hanslmeier, my supervisor: "Would it be possible to find out this relationship?" I only replied "Whoever searches will always find". I hoped for the first time to quantify this relation.

At that time, however, I was not so sure because I had to develop an efficient algorithm for the photometric segmentation of these images, to implement and apply it to the automatic identification of granular cells and measurement of their morphometric parameters, including granular area, perimeter, and contrast, frame by frame, granule by granule. A good decision was to select several representative image sequences with different cadence, which were obtained in the seasons of the best Hinode performance. Occasionally, these seasons corresponded with the seasons of medium solar activity.

Another fortunate factor in this study was that I got complete freedom of action (carte blanche) in terms of methodology and data processing software. Therefore, I was able to use MATLAB software package which I learned and liked during my master’s degree at the Graz University of Technology. The importance of statistical methods for the granulometric processing of Hinode image time series is undeniable, and the knowledge and skills derived from the course "Statistical Methods for Processing Data Time Series" given by Dr. Lothka were very useful.

A rather vague photometric definition of granules found in the literature (Hirzberger 2002, Yu et al. 2011, Takayoshi 2018) and the lack of additional data, e.g. the vertical flow velocities of the granular matter were a kind of challenge to be solved. Therefore, the present study focussed on the precise morphometric analysis of granular cells. This reduced the efforts for data processing and physical interpretation of the results. The morphometric parameters of

granules were also measured in this work, albeit to a lesser degree, mainly for comparison with the results of other researchers and for the validation of mines.

Further details of the present research can be found in the next section, which gives the outline of the thesis, and in the following sections. The author hopes that the all subsequent chapters of this thesis will live up to your expectations. He will be pleased to receive your comments and suggestions regarding the contents and quality, comments on possible improvements and, of course, incentives to greater efforts.

0.2 Outline of the thesis

The *main goal* of the present study is to investigate the variability of solar granulation related to the solar activity cycle with the aid of image series taken by the Hinode Solar Optical Telescope in 2006 - 2016. The *working hypothesis* states that there exist a basic physical relationship and a statistically significant temporal correlation between the solar granulation scale and the sunspot number (SSN) index. The conjectural correctness of this hypothesis constitutes the scientific problem of the present study.

In order to achieve the main goal and to prove or disprove the working hypothesis, the next research and development tasks had to be solved:

- to review main theoretical and methodological concepts in the area of solar granulation observations, to identify the state of the art, technical problems and possible solutions;
- to study basic characteristics and artefacts of the high-resolution Hinode broadband filtergrams obtained in the blue continuum channel at 450.45 nm at the disk centre;
- to select relevant image data from the IGAM archive and to inspect their quality;
- to construct several regular Hinode image time series (HITS) with ~120 images each;
- to form SSN time series corresponding to HITS from the SILSO archive;
- to design, to implement and to validate an efficient algorithm for HITS segmentation and morphometric analysis;
- to perform relevant image corrections for the sake of homogenization of HITS;
- to process HITS, one by one and to measure morphological properties of the solar granulation including granular area, perimeter and contrast in the quiet-sun region at the disk centre over the activity cycle and to estimate their statistical variations;
- to critically evaluate and to interpret correlation measures between the granular scale and SSN, and between different HITS with 1-day, 27-day and 30-day time intervals;
- to clearly present, to validate and to discuss the results;
- to summarize new in-depth knowledge gained in the study frameworks.

One of further objectives is to author a scientific paper as the result of the study. The present study is quite ambitious with respect to both, the scientific level and programmatic / technical realisation of the research study. An important scientific question and several technological problems related to the automatic processing of ‘big data’ in a limited period of time will be solved in the course of the study. The duration of the work was planned to be 8 months or 800 working hours in the period of August 2019 – March 2020.

Chapter 1. Solar Activity, Convection and Granulation

1.1 Solar activity cycle

Studies of solar activity and the solar activity cycle represent an area of active research that is of particular interest and practical relevance for solar physics, astrophysics and geophysics and because of its direct influence on space weather and climate predictions is of crucial importance for the human race. But what is solar activity? According to (Godoli & Allen 1964) the term "solar activity" refers to *all* solar phenomena which vary systematically with the solar cycle of about 11 years[2]. In other words, this is an overall complex of phenomena that occur on the Sun and characterize the substantial variability of solar basic processes and properties[3]. Solar activity is manifested in enormous energy releases, such as solar flares and coronal mass ejections, and essentially determines the plasma conditions in the entire heliosphere and solar interiors (Zaqarashvili et al. 2015). The number and size of sunspots, the amount of solar radiation, solar oscillations, solar wind and other solar phenomena are all affected by the solar activity cycle. The source of solar activity is the magnetic field (Gough 2000).

Accordingly, the 11-year sunspot cycle is related to the full 22-year cycle of solar magnetic activity called the Hale cycle after its discoverer. Both cycles are thought to be a result of the variable efficiency of solar dynamo action that is responsible for the generation and reversal of the cyclic global magnetic field in the solar interior and at the solar surface. The oscillations of solar magnetic field amounting to the exchange of energy between poloidal and toroidal magnetic field components with a periodicity of 22 years is referred to as Babcock–Leighton solar dynamo cycle (Cameron & Schüssler 2015).

The duration of solar cycles varies from cycle to cycle. Starting from 1755, each sunspot cycle is counted from the moment of the minimum level of solar activity, i.e. minimum number of sunspots, to the next minimum. During the period of solar minimum, the main activity events such as flares, coronal mass ejections, solar radio noise or terrestrial auroras occur less frequently than at maximum. Some observables, such as the amplitude of solar oscillations and the intensity of cosmic-ray showers in the Earth' atmosphere act in antiphase with the sunspot cycle.

Although the cycle of solar activity has been studied for a long time, it is not well understood today. No wonder that the activity forecasts for the current 24th cycle turned out to be wrong (Balogh et al. 2014). The number of indicators of solar activity gradually increases with the progress of solar observation, whereas the concept of solar activity becomes very complex. The magnetic indicators of solar activity behave differently in the northern and southern hemispheres of the Sun. They are said to be somewhat asynchronous and asymmetric, which complicates the causal analysis of solar activity. The relationships between the variability of solar observables and the natural causes of this variability are neither simple nor linear (Ermolli et al. 2014). The nature of the solar dynamo is just one example of such complexity.

[2] The 11-year cycle of solar activity is also called the sunspot cycle or the Schwabe cycle.

[3] Arguably, solar activity also includes aperiodic events, but it should not be confused with evolution.

We can assume that solar activity includes cyclic magnetic activity, radiation activity, and convection activity[4]. One should be aware, however, that the terms of solar magnetic activity and radiation activity are well known and well established, while the concept of solar convection activity is not yet generally accepted and remains a literary construct. This is due to the deficiency of reliable information on the dynamics of the solar convection zone and the lack of measurable properties or proxies that might represent the solar convection activity on an operational level. It is also not entirely clear how the dynamic behaviour of solar surface convection is related to the global magnetic activity of the Sun. There are theoretical justifications and observational indications for such a dependency, but the reason and the mechanism of this dependency have not yet been fully defined and/or explained. So far, there exist no activity indices derived from or related to the solar surface convection activity[5].

Traditionally, solar activity is characterized by activity indices, which are derived from direct systematic observations of the solar atmosphere, including the photosphere, chromosphere, and corona. The sunspot number (SSN), the sunspot area, the total solar irradiance (TSI), the solar effective temperature, the radio flux at 10.7 cm and the flare index are the indices that are most widely used to describe long-term solar activity. Geophysical indices are not included.

The standard expression for the SSN index is given with the Wolf number

$$R = k \cdot (10 \cdot g + f) \tag{1}$$

containing the number of sunspot groups *g*, the total number of individual spots *f* and a reduction coefficient *k* of order unity depending on the instrument and observing technique used at each observatory. Regular measurements of SSN have been going on for over 200 years. Figure 1 represents daily SSN time series for the period of 1996 - 2019 (at the left) and SSN mean monthly values for the period of 1995 – 2019 (at the right). The amplitude of daily SSN variability is significantly larger than that of monthly mean variability. The source data for SSN are the revised International Sunspot Numbers (ISN v2.0) available at the Royal Observatory of Belgium, http://www.sidc.be/silso/datafiles .

Daily SSN values and monthly means are highly scattered and, usually, the 13-month smoothed monthly SSN is used as the main index of solar activity. Various solar parameters and almost all activity indices are statistically related and correlate well with the sunspot number[6], which, along with the simplicity, accuracy and duration of SSN observations, makes this index very popular in statistical studies of solar activity. A correlation between magnetic activity and solar luminosity was studied in (Spiegel & Weiss 1980). Generally, solar luminosity increases with solar activity. It was revealed, however, that solar luminosity decreases by as much as 0.3% on a 10-day timescale when large groups of sunspots occupy the solar surface. Besides, it was recognized that the equivalent width of some photospheric lines[7] and the line flux vary with the change in solar activity (Livingston 1983, White et al. 1987).

[4] Presumably, it includes also rotational and even gravitational activity.

[5] Helioseismology provide proxies for the structure of convection zone, including rotation and density stratification.

[6] The main reason for the close relationship between solar indices is their dependence on the same process - variations in the solar magnetic field.

[7] As the Ca II K line.

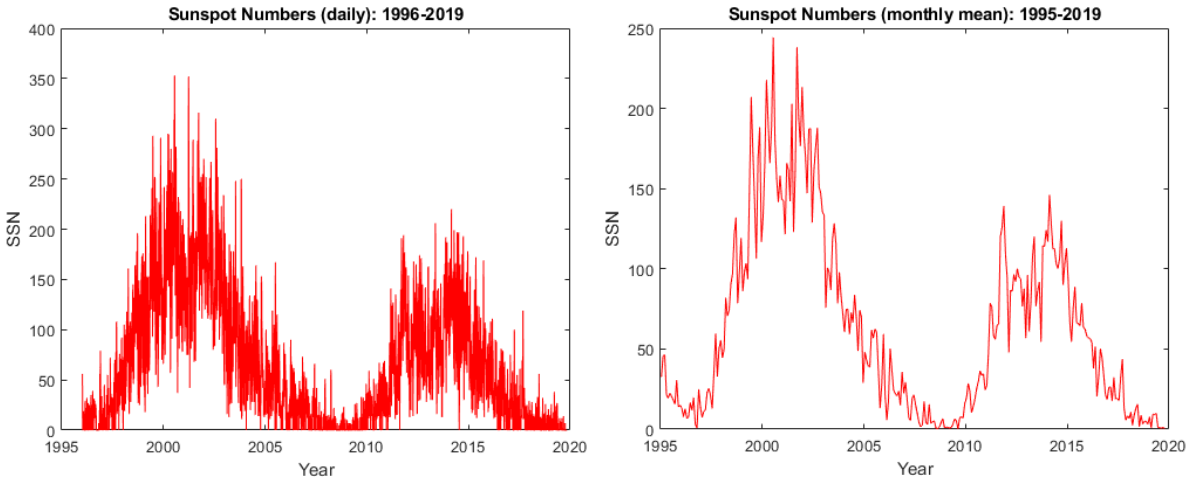

Figure 1. Daily SSN (left) and monthly mean SSN (right) values for the period of 1995 – 2019

Morphometric analysis of solar photographs with visually identified granules showed that the granulation scale varies in antiphase with the sunspot number (Macris et al. 1984). The mean distance between photospheric granules decreases with increasing activity. Controversially, it was found that granulation contrast varies nearly in phase with the solar cycle, being lower at the maximum of activity (Muller at al. 2007). The overall correlation between the magnetic properties of granules and the convection flow was investigated in (Jin et al. 2009). The global magnetic field changes sign every 11 years and the reversal of polar magnetic fields occurs when the SSN index attains maximum, while the polarity reversal of sunspots occurs at the beginning of a new cycle. Also p-mode frequencies of seismic oscillations change with the solar cycle, the frequencies being greatest at sunspot maximum. The amplitude of solar 5-min oscillations is higher at the solar minimum.

Using data from the Global Oscillations Network Group (GONG) for the period of 1995 - 1998 (Antia & Basu 2000) tried to detect changes in the convection zone structure by studying variability of solar oscillation frequencies with solar activity. Hitherto they have found no evidence of a change in the convection zone depth or extent of overshoot below the convection zone during the solar cycle. Nonetheless, there is a firm belief that the entire structure of the convection zone changes with the solar cycle (Gough 2000).

Yet, there is a limitation to the use of the SSN index for correlation studies with regard to solar convection activity. During long periods of minimal activity in the solar cycle, the SSN index often reaches zero values, as it was in the period of 2006-2010[8] (Fig. 1), while the solar activity remains well above its zero level. In such cases no correlation analysis between the SSN index and the plasma convection parameters is possible and other activity indices, e.g. the total solar irradiance or the 10.7-cm radio flux should be used instead of SSN. Yet, the TSI peak-to-peak variations over the entire activity cycle attain only 0.14% at maximum and are not well suited for studying solar activities over medium-term time intervals. The 10.7-cm radiation comes mainly from the regions with strong magnetic fields in the lower corona and on the solar

[8] During the long solar minimum between cycles 23 and 24 in 2006-2010, the SSN index got null values on 794 days.

surface[9], i.e. either far from the convection zone or/and under completely different plasma conditions compared to the quite-sun areas of surface convection. Both indices are therefore difficult to compare with plasma parameters in the convection zone. It is also difficult to understand their physical relationships, if any, with solar convection.

Naturally, there is a need for a measurable and reliable physical parameter or some cyclic proxy that provides, on the one hand, comparability with the SSN index, proximity of native conditions and interdependence with plasma conditions in the convection zone, on the other. Moreover, it is desirable to have such cyclic proxies that change differently with time, that is, have different periods or act in antiphase with the SSN index (Bruevich & Yakunina 2013). These conditions can be met, at least in part, by comparing the granulation properties and their variability with the SSN index over the solar activity cycle. If a stable relationship between the surface convection parameters and the number of sunspots can be determined for the rising and descending branches of the activity cycle, this dependency can also be extrapolated to the minimum phase of the activity cycle, for example by entering negative SSN values.

1.2 Solar convection and granulation

Solar convection is an outward transfer of energy by the bulk movement of plasma within the upper third of the Sun's interior under the influence of thermal buoyancy. Convection is responsible for the circulation flow of gas masses wherein hot plasma ascends from the bottom of the convection zone toward the solar surface, cools down by radiating photons, loses its buoyancy, spreads sideways and descends to be heated again. In the long run the convective process ensures mixing and uniform heating of solar gases thus leading to plasma stratification. Due to the permanent income of energy from the core, circulation flows don't cease and are repeated endlessly long. This unceasing physical phenomenon determines the temperature and luminosity, structure, dynamics and characteristic appearance of the solar surface. Also 5-minute photospheric oscillations are driven by solar convection (Hanslmeier 2007).

The convection zone occupies the upper layer of solar interior extending from the solar surface down to a depth of approx. 200.000 km. The temperature in the convection zone varies between $6 \cdot 10^3$ °C at the top and $2 \cdot 10^6$ °C at the bottom. The position of the convection zone inside the Sun is shown in Figure 2. Gas masses in the convection zone are heated and ionized by energetic gamma- and x-rays coming from the radiative zone. The convection zone is a very turbulent medium. Hence convective cells[10] do not always rise or subside vertically, but often move along swirling trajectories. Convective cells originating at the top of the convection zone and overshooting into the photosphere represent the main energy carrier and structural element at the solar surface (Muller 1985).

Despite the relative constancy of the energy flux entering the convection zone, solar convection is a variable phenomenon because of its complex interplay with the magnetic field, radiation and rotation of the Sun. The interaction between the electrically charged plasma set in motion

[9] Even at solar minimum there is a non-zero 10.7-cm radio noise from thermal f-f emission (Balogh 2014).

[10] Convective cell or Bénard cell is a limited transient volume in which upward movement of hot plasma in the centre is balanced by downward motion of cooler plasma at the periphery.

and the solar differential rotation in the convection zone induces electrical currents and magnetic fields, both global and local, by means of dynamo action[11]. Solar global magnetic field is thought to be generated close to the base of the convection zone. Deep inside the convection zone the magnetic field is mostly horizontal and is in the frozen-in condition which means that magnetic field lines follow plasma motions and magnetic fields get moved around by convective flows (Pevtsov et al. 2011).

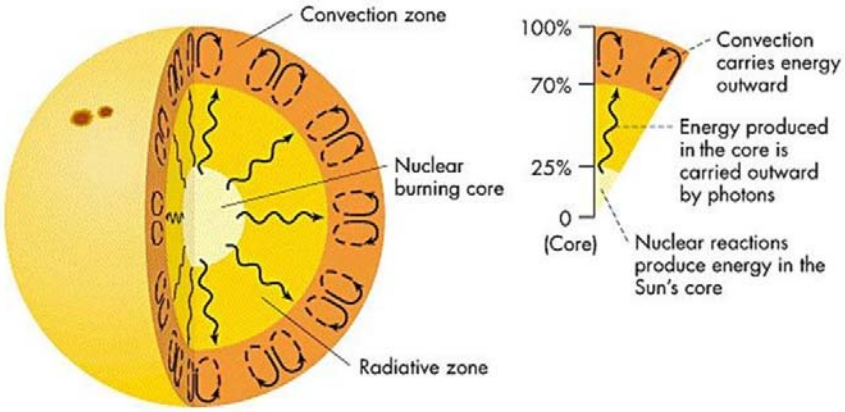

Figure 2. Sun interior structure (adopted from Hanslmeier, 2007)

Due to the joint action of the differential rotation of the Sun, turbulent convective flows and the Coriolis force the solar magnetic field is twisted into spirals, amplified and lifted up toward the solar surface. This action is referred to as alpha-omega dynamo process. In the upper layer of the convection zone the enhanced magnetic field changes direction, bursts through the solar surface and initiates the formation of pores and sunspots, being visible at the photosphere as dark features being essentially colder than the surrounding surface. The strength and structure of magnetic fields in the convection zone regulate the quantity and spatial distribution of pores and sunspots at the solar surface. The operation of the solar dynamo changes in response to variations in the transport of energy within the convection zone thereby influencing the period and the amplitude of the full magnetic cycle (Working Document 1983).

Solar convection and magnetism are closely interrelated and interact on a local and global level (Schüssler 2002, Cattaneo et al. 2003, Muller et al. 2018). The reverse dynamical effect of the internal magnetic field on the convective motion of plasma is the ability to channel the flow of ionized gases and to enhance, to attenuate or even to suppress the convection locally. Concentrated magnetic fields modify the convective flux by changing the mixing length[12] and distorting convective flows at the solar surface, preventing the horizontal expansion of convective cells, and inhibiting the heat flow to the surface from the convection zone below. All in all, magnetic field has a significant dynamical effect on the plasma convection.

The convection zone, aside from its uppermost layer is adiabatically stratified (Gough 2000). A sharp increase in the temperature gradient in the uppermost super-adiabatic layer of the convection zone leads to increasing convection instability and turbulent movements of the

[11] According to Maxwell's first law, the electrical current density in the plasma is the source of the magnetic field.

[12] Mixing length is a mean length of travel over which a gas parcel maintains its identity before being mixed with the surrounding plasma.

plasma. The top layer of the convection zone is therefore essentially turbulent. This turbulence affects the shapes and widths of the Fraunhofer spectral lines and can be detected thereby. Turbulent convection produces shocks and acoustic waves at the solar surface which result in solar oscillations and heat the lower atmosphere. Hence convection is an important driving force for the solar activity (Nordlund et al. 2009, Haslmeier et al. 2009).

Solar convection in deep layers is studied with indirect methods including helioseismology, theoretical modelling and numerical simulations. Solar *surface convection* can be observed directly with ground- and space-based telescopes thus providing sound observational constraints for indirect determinations and computer models of solar convection. Solar surface convection is a sort of cellular convection[13] which is confined to a shallow superficial layer and can be seen in the form of photospheric granulation. Apart from pores and sunspots, the entire photosphere is composed of convection cells called granules, which are believed to be the hot and bright tops of rising convective columns separated by darker intergranular lanes. The topology of solar surface convection is controlled by mass conservation. Warm upflows diverge and tend to be laminar, while cool downflows converge and tend to be turbulent (Stein 2012).

Solar granulation is a shallow phenomenon. Granulation cells have a vertical extent comparable with the thickness of the super-adiabatic layer in the uppermost part of the convection zone. In the photosphere, the gas pressure is greater than the magnetic pressure and the photospheric movements are mainly driven by convection. The convective energy in the vertical flow transforms into radiation and horizontal movements of granules at the solar surface. Radiative cooling efficiently regulates solar convection and complicates the analysis of convective motions in the photosphere[14]. All granular motions are a result of mass conservation and a balance between upward transportation of the internal energy and radiative cooling (Hanslmeier et al. 2006).

A very simple expression for the upper limit to the granulation size was given in (Nelson & Musman 1978) under the assumption that all the energy in the vertical flow goes into driving the horizontal motions of granules at the solar surface

$$d_h \cong 2\pi \cdot \frac{u}{v} \cdot H_\rho \,, \tag{2}$$

where $H_\rho \approx 100\ km$ is the scale height assuming that both density and vertical velocity vary exponentially through the sub-photospheric region. This approximate equation neglects the process of radiative cooling and shows that the horizontal size of granules d_h is proportional to the tangent ratio between horizontal *u* and vertical *v* velocities of convective cells.

From the mixing-length theory it is known that the horizontal size of convective cells is comparable with or nearly equal to the mixing length l_m. If both variables are related, it can be assumed that the size of solar granulation varies with l_m. This assumption is supported by a fairly isotropic structure of the granular pattern, which implies almost the same mixing length for all granular elements on the solar surface.

[13] Cellular convection is a periodic form of convection separated by stream surfaces across which there is little mixing of the plasma (AMS Glossary 2012).

[14] This is known as “radiative boundary problem”.

In the mixing-length theory one of fundamental equations is that describing the convective flux. The local flux of convective energy F_{conv} is given by (c.f. Hanslmeier et al. 2010)

$$\pi \cdot F_{conv} = \rho \cdot v \cdot c_p \cdot \Delta T \,, \tag{3}$$

where ρ is the local density, v - the local vertical velocity, c_p is the specific heat in a constant pressure process and ΔT is the local temperature difference between a convective cell and its surroundings. The Eq. (3) adopts that all convective cells in the considered region move with equal velocity.

The local temperature gradient ΔT depends on the mixing length l_m as (Schüssler 2002)

$$\Delta T = T \cdot (\nabla - \nabla_i) \cdot \frac{l_m}{H_p} \,, \tag{4}$$

where T is the mean temperature.

$$\nabla = \left|\frac{d\ln T}{d\ln P}\right|_{rad} \quad \text{and} \quad \nabla_i = \left|\frac{d\ln T}{d\ln P}\right|_{ad*} \tag{5}$$

are the radiative temperature gradient of a gas parcel and the (super-)adiabatic temperature gradient of the ambient medium respectively. The difference $(\nabla - \nabla_i)$ between these gradients determines the degree of convective stability of the plasma with respect to a local perturbation and is called the Schwarzschild criterion for convective instability. The positive value of $(\nabla - \nabla_i)$ means convective instability[15].

The pressure scale height H_p in the Eq. 4 is defined as

$$H_p = \frac{k \cdot T}{g \cdot \mu \cdot m_H} \,, \tag{6}$$

where T is the mean temperature, g is the solar gravity, k – Boltzmann constant and $\mu \cdot m_H$ is the average mass per particle with μ - mean molecular mass, i.e. an average number of amu's per particle; m_H – atomic mass of hydrogen.

Then the equation (3) can be rewritten in the next form

$$\pi \cdot F_{conv} = \rho \cdot v \cdot c_p \cdot T \cdot (\nabla - \nabla_i) \cdot \frac{l_m}{H_p} \,, \tag{7}$$

while the vertical velocity can be derived from Eq. (2) as

$$v \cong 2\pi \cdot \frac{u}{d_h} \cdot H_\rho \,. \tag{8}$$

The substitution of Eq. (8) in Eq. (7) with subsequent simplification for the sub-photospheric layer ($H_\rho \cong H_p$) provides a useful expression for the convective flow

$$F_{conv} \cong 2\,\rho \cdot u \cdot c_p \cdot T \cdot (\nabla - \nabla_i) \cdot \frac{l_m}{d_h} \,, \tag{9}$$

[15] Due to the sharp increase in the radiative temperature gradient $|dT/dr|_{rad}$ near the solar surface, the convection instability grows significantly and results in turbulent motions. In deeper layers, the convection zone is adiabatically stratified and homentropic (Gough 2000).

which shows the direct proportionality between the energy flux and the mixing length. The horizontal velocity of convection currents *u* increases with the convection flow to the solar surface. It can also be seen that the granular size d_h is inversely related with F_{conv}. Interactive effects between the granular size and the granular proper motion should also be taken into account.

The mixing length is often parameterized with an expansion parameter *α* and expressed simply as

$$l_m = \alpha H_p = \frac{T}{g} \cdot \frac{\alpha}{\mu \cdot m_H} \quad . \tag{10}$$

The second factor in the right part of Eq. (10) is a constant, and the equation shows that the mixing length varies inversely with the local gravity. The inclusion of spatiotemporal variations in local gravity could enliven the entire analysis, but would go beyond the scope of this study.

Another frequently used expression for the local flux of convective energy demonstrates the quadratic dependence of F_{conv} on *α* and ultimately on the mixing length (Kudritzki 2011).

$$F_{conv} = \rho \cdot c_p \cdot T \cdot \propto^2 \cdot \left(g \cdot \chi_p \cdot H_p\right)^{\frac{1}{2}} \cdot (\nabla - \nabla_i)^{\frac{3}{2}} , \quad \propto = l_m / H_p. \tag{11}$$

Note that Eq. (11) is stricter but more complex than Eq. (9).

In any case, the mixing-length theory cannot adequately describe convection at the solar surface because it does not account for the non-linearity of flows, compressibility effects and shocks. Nevertheless, such a description is useful because it demonstrates fundamental dependences between the convection flow and the granulation parameters. And it's easy to understand. With this, we can be more or less certain that the horizontal size of photospheric granules can be used as a proxy for energy transport in the solar convection zone.

1.3 Definition of granules and granular cells

Solar granulation is one of the most remarkable, astonishing and intriguing features of the photosphere. In contrast to sunspots, the granulation is always present on the Sun's surface. Systematic observations of solar granulation and precise measurements of its spatiotemporal characteristics on a local and global level form a solid basis for the investigation of periodic convective currents and cyclic magnetic fields with regard to the solar activity cycle.

The topology of solar surface convection is controlled by mass conservation. Warm upflows diverge and tend to be laminar, while cool downflows converge and tend to be turbulent (Stein 2012). Accordingly, the rising part of solar granules is located in the centre where the plasma is hotter. The outer edge of the granules is darker due to the cooler descending plasma. A typical granule is 1000 km or 1.4'' in diameter and nearly 0.8 million km² in area. The lifetime of an average granule is about 10 minutes. The amount of granules, their brightness, shape, size, and position change within certain limits all the time.

There may be tri- and quadrilateral, penta- and hexagonal granules as well as polygonal granules of quite irregular shape. In regions of quite Sun there are no very large, protrusive or widely separated granules and the granular size distribution is uniform. There are no "foreign bodies" either. To all appearance, all granules are of the same origin and material. This is

rather regular and tight pattern with even surface and homogeneous texture resembling tidy gravel beach covered with fine angular gravel with sharp edges. Some observers even noted crystalline structure of photospheric granules (Noever 1994).

Indeed, the rapid increase in opacity with depth due to the hydrogen ionization ensures high contrast and sharpness of the granulation pattern in optical imagery. Under large magnifications or in large-scale computer models the solar granular pattern looks like a scattering of golden nuggets with glittering and undulating shape. Yet, “all is not gold that glitters” and in reality, this is a continuously changing network of convective «bubbles» that grow, fragment, decay or explode and emerge again in a fairly short period of time.

The quiet-sun granulation is readily discernible in high-resolution optical images of the solar photosphere (Figure 3). The results of morphometric analysis depend on the granule definition, however. There are several different definitions depending on photometric, morphometric, altimetric and tachometric principles of the granulometric analysis.

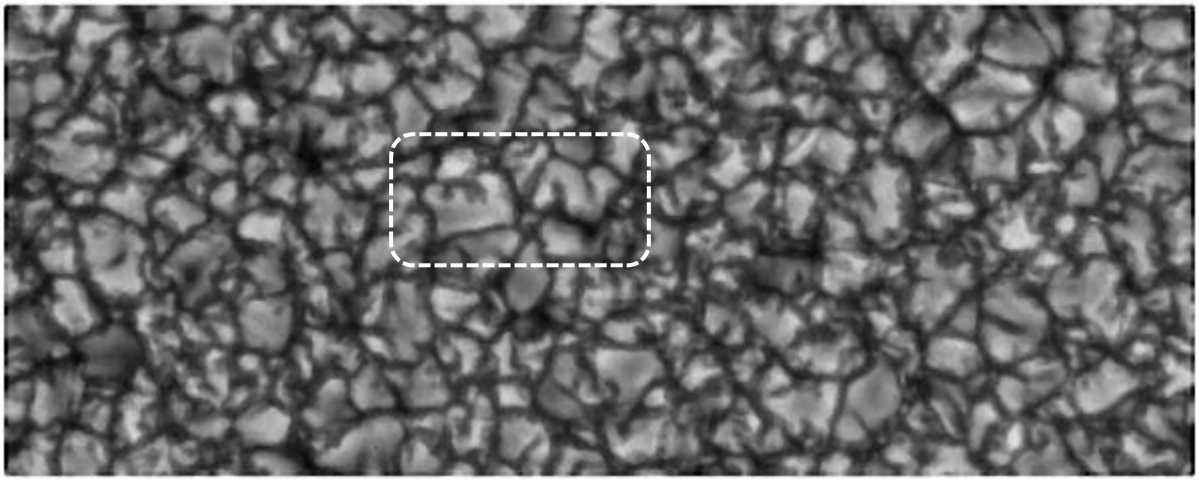

Figure 3. Granulation pattern in the Hinode blue continuum FG20080802 with elements of an “alphabet soup” (framed)

According to (Hirzberger 2001, Yu et al. 2011), a granule is a bright element of a granular pattern excluding the darker intergranular strip surrounding this element. A granular cell is a somewhat larger element including the granule and a half of the intergranular lane width around this granule (Bray et al. 1964, Müller et al. 2001). Then the granular area A_g is given as a difference between the total cell area A_c and the area of its surrounding part of the intergranular stripes A_s that is (cf. Hirzbereger 2002)

$$A_g = A_c - A_s\,. \tag{12}$$

In a quiet-sun region the total area of all granular cells entirely covering the field of view is equal to the field of view area

$$A_{FOV} = \sum_{i=1}^{n} A_{ci}\,, \tag{13}$$

where n is the total number of granular cells, which is equal to the total number of granules.

For the mean cell area, we can write

$$\overline{A_c} = \frac{A_{FOV}}{n}. \tag{14}$$

The boundary of a granular cell is a polyline that connects image pixels with locally minimal intensity values, while each granule is delimited with more diffuse and less perceptible boundary that extends over areas with gradually varying intensity. Hence the identification of a granular cell is more straightforward than that of a granule, especially in image time series with heterogeneous contrast. The variable contrast of solar granulation makes the granule definition uncertain and the precise measurement of A_g difficult.

Correspondingly, quite different empirical values of the normalized continuum intensity I_{cb} were reported for the boundary between granules and granular lanes. For example, (Takayoshi 2018) specifies the threshold as $I_{cb} = 0.98$, while (Haslmeier et al. 2000) give $I_{cb} = 1.0$, the latter being widely accepted value. In (Bovelet & Wiehr 2001) the typical fractional granular area is 60% of the field of view, while in (Hirzberger 2001) and (Roudier & Muller 1987) it is only 47.7% and 39%, respectively. This indicates that the total value of the granular area $\sum_{i=1}^{n} A_{gi}$ strongly depends on the image quality and the image processing method. It is therefore hardly reproducible in other studies. The number of structural elements N determined within the given area is a more stationary parameter that can be used to compare and verify the results of granulometric analysis obtained by different investigators.

Most granular cells feature a flat broad maximum of intensity and a narrower sharper intergranular lane (Nelson & Musman 1978). Also the results of hydrodynamic modelling show that the brightness of intergranular lanes decreases rapidly with the increase of their width (Gadun et al. 2000). In addition to the regular, dynamic and recurring appearance of granules in multitemporal images, which is typical of the convective pattern, Doppler shift measurements of the light from individual granules seen in spectrograms provide evidence for their vertical motion and their convective nature (Bahng & Schwarzschild, 1961).

In an attempt to improve the identification of granules and intergranular lanes of photospheric convection (Hirzbereger 2001) and then (Takayoshi 2018), in addition to the photometric thresholds, used flow maps showing the photospheric convection velocities overlaid on the granular pattern. The modified concept of a granule involving granulation contrast and flow velocity is illustrated in Figure 4 based on the classification scheme provided in (Takayoshi 2018). Here the intensity pattern was normalized by the mean intensity I_0 determined over the entire field of view.

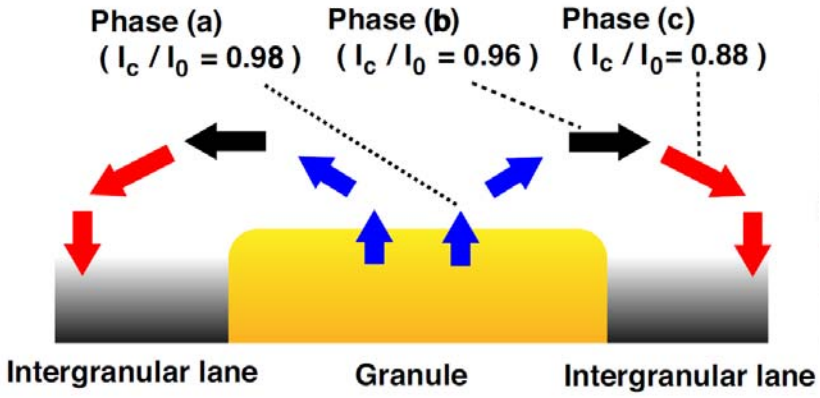

Figure 4. Modified physical concept of a granule (after Takayoshi 2018): phase a) pure vertical flow; phase b) horizontal flow; phase c): maximal flow velocity in descending motion

A reasonably good agreement between the granules and the areas of convective flow has been reported. Intensities and velocities of granules in the low photosphere correlated well. It was found that the distribution of intensity and velocity within the granular area depended on the granular size. In smaller structures, the maximum intensities and velocities are close to the granular barycentre, while in larger granules the maxima are shifted towards the granular boundaries. It was noted that there exists a transition zone between the granular and intergranular areas with a width of 0.5 arc sec, the latter being independent of the granular intensity (Hirzberger 2002). Some discrepancies due to intrinsic differences between broadband intensities and flow velocities were also mentioned. From a physical point of view this is more informed approach that ensures some improvement of granulometric estimations at the cost of increased complexity of the analysis.

There were no flow maps available for the present study, and we had to deal only with conventional broadband images of photospheric granulation. Hence we had to avoid precise delimitation of granular areas and, instead, concentrated on the precise morphometric analysis of granular cells. This allowed the efforts related with data processing and physical interpretation of the results to be reduced. Further relevant knowledge about the discovery, subsequent observations and morphometric analysis of solar granulation can be obtained from thorough historical reviews in (Bartholomew 1976, Spruit et al. 1990) and from the next section of this thesis.

1.4 Observations of solar granulation: history and state of the art

A number of case studies using methods of photogrammetric, spectral, morphological and correlation analysis of optical images have already been carried out to identify the dynamic behaviour of solar granulation in response to a change in solar activity. The earliest attempts to determine the relationship between the solar granulation scale and the amplitude or phase of the activity cycle were made by (Macris et al. 1984, Muller & Roudier 1984) with the aid of high-resolution photographs taken at the Pic-du-Midi Observatory. It was found that the size of photospheric granulation varies over the solar cycle, whereby the granules become smaller by 5% from solar minimum to solar maximum (Muller 1989). Relative variations in the total number of granules within the specified area attained 22%. Observations showed also that the granulation contrast varies in antiphase with the solar cycle, being lower at maxima of activity (Muller et al. 2007). The magnitude of the contrast variation between two maxima of 1980 and 1991 and the minimum of 1986 was given as 20%.

The Institute of Geophysics, Astrophysics and Meteorology (IGAM) at the University of Graz has been carrying out in-depth studies on granulation dynamics with image data from ground and space-based telescopes since 1996 (Hirzberger et al. 1999). State of the art 2D numerical models and hydrodynamic simulations showing general evolution and velocity fields of solar granulation were offered in (Gadun et al. 2000). Computer simulations showed that the average size of granules decreases with increasing mean strength of the solar magnetic field (Cattaneo et al. 2003). Also (Saldaña-Muñoz et al. 2004) carried out statistical investigations of granulation time series taken at Pic du Midi in 1978 – 1991 using methods of power spectra analysis. In this work, the authors came to the opposite conclusion about the increase in the number of small granules during the solar minimum, which contradicts the previous results.

Similar to the study by (Muller 1989), W. Pötzi discovered a reduction in the size of the granules during the solar maximum around 2001 in the sequence of G-band granulation filtergrams obtained from the Dutch Open Telescope. He noted that the mean area and perimeter of granules measured during the solar minimum of 2006 – 2007 were lesser scattered than those of solar maximum around 2001 (Pötzi 2009). Since then, the variation of solar convection over the solar activity cycle is being discussed with controversial results (Hanslmeier et al. 2010).

In fact, (Muller, Utz and Hanslmeier 2011) could not rule out statistically significant variation of solar granulation over an activity cycle with Hinode high-resolution images taken in the G-band and blue continuum window during the extended period of solar minimum in November 2006 – July 2010. Hence, the conclusion was, that the structure of solar granulation did not change during the minimum phase. Earlier determined trends were attributed to instrumental effects. In (Hanslmeier et al. 2012), authors explain the invariability of solar granulation parameters during the extended minimum of solar activity in 2006 - 2011 by small variation of the total solar irradiance.

Later on, the same authors showed that the scale of the solar granulation does increase and the contrast does decrease towards the poles, but not regularly. At latitudes of 60° both quantities became equal to those obtained at the solar disk centre. This irregular latitudinal variation of the granular pattern during the period of minimum solar activity in 2009 was explained by the differential rotation and the perturbation of meridional circulation around 60° (Muller, Hanslmeier and Utz, 2016).

A detailed granulometric investigation using seven Hinode optical image sets and the marker-controlled watershed algorithm for the automatic recognition and delineation of granules and granular cells was carried out by (Yu et al. 2011). The influence of local magnetic fields on the evolution of small, medium and large granules in the quiet-sun region near the disk centre was discussed and the variation of local magnetic properties in dependence of the granular diameter was determined. However, they didn’t study the variation of solar granulation over an activity cycle.

Finally, a substantial and careful report on the behaviour of photospheric granulation in the 10-year period of 2006 - 2016 was published by (Muller et al. 2018) being based on the morphometric analysis of high-resolution filtergrams obtained by the Hinode solar optical telescope (SOT) in the blue continuum channel. Again, there were no decisive conclusions made on the variability of the granulation scale and contrast with respect to the solar activity. Instead, various instrumental effects on the long-term quality and homogeneity of high-resolution Hinode image time series were noted including orbital, thermal, mechanical and electronic impacts. It was mentioned that these exclusive, uniquely detailed and seeing-free image time series obtained by the Hinode space-borne telescope suffer from image blurring and uncontrolled changes in intensity. The authors have concluded that the variation of photospheric granulation related to 11-year solar cycle remains an open issue (Muller et al. 2018).

Quite recently a comprehensive review of the Hinode performance in the first eleven years was issued by the Hinode Review Team including 35 authors. Among other things, they pointed to an unexpected change in the best focus position (~7 steps) according to the change in pointing on the solar disk. The cause of this focus change is not well understood and one should account for the short-term defocussing due to change in pointing. Besides, it was reported that during the eclipse season from early May to early August, a large focus drift (~12

steps) occurs approx. 30 minutes from the dawn in each orbit. This behaviour was explained by thermal deformation of the heat-dump-mirror cylinder and its supporting spider which can displace the secondary mirror during the day-night cycle and it was stated that “the eclipse season is certainly a degraded performance period for SOT” (Al-Janabi et al. 2019).

All in all, the variation of the photospheric granulation related to the solar activity cycle remains an open issue which deserves to be investigated further with very homogeneous sets of images (Muller et al. 2018). The sheer curiosity and natural desire to test own abilities and skills in processing big data were the main motive for the further search for a solution to this open and complex problem in the frameworks of the present thesis.

Chapter 2. Hinode Surveys of Solar Granulation

2.1 Hinode sensor complement

The launch of an optical 50-cm solar telescope on board the Japanese Hinode spacecraft[16] on September 22, 2006 gave new impetus to systematic and detailed observations of photospheric granulation. The Hinode solar observatory satellite was built in international cooperation between Japan, the USA and Great Britain[17]. It carries three telescopes on board, namely

- a Solar Optical Telescope (SOT) for the continuous high-resolution photospheric and chromospheric imaging and spectropolarimetry in narrow bands of the spectral range between 380 and 670 nm with a consistent spatial resolution of 0.2",
- an X-ray telescope (XRT) for complete imaging of the upper corona with an improved angular resolution of 2" at plasma temperatures between 1 and 30 million °K,
- an EUV Imaging Spectrometer (EIS) for observing the dynamics of the magnetic reconnection, for imaging and determining the speed field in the lower corona and transition area with an accuracy of 1 km / s.

A synergetic combination of the data obtained from these three sensors on a systematic level should finally solve the longstanding controversies about coronary heating and solar dynamics. Regrettably, SOT observations were terminated in February 2016 due to the short circuit in the CCD camera electronics. Two other telescopes continue to work. The complement of Hinode sensors is illustrated in Figure 5.

Figure 5. Hinode sensor complement and coordinate system (© eoPortal 2019)

The size of the spacecraft bus is 3.8 x 2.0 x 1.6 m³ and the dry mass is 0.7 tons. 175 kg of thrust gas to maintain orbit increase the initial mass. Two solar panels (SAP) with a total length

[16] Hinode ("日の出") means sunrise in Japanese - a symbolic name for the "land of the rising sun".

[17] ESA and the Norwegian Space Centre have contributed to the operation of data receiving station in Svalbard.

of 10 meters provide the electrical power of 1 kW. An on-board solid state recorder has a capacity of 8 Gbit.

2.2 Optical system of solar telescope

SOT is an aplanatic Gregorian telescope with unprecedentedly high diffraction-limited angular resolution of 0.19'' or approximately 140 km on the solar surface. The effective focal length of SOT is 4.52 m and the relative aperture is f / 9. The diffraction-limited field of view is given as 361" x 197" (Berger & Slater 2009). From the beginning of observations in November 2006 to the end of the lifespan due to the sensor crash in February 2016, the Hinode Solar Optical Telescope (SOT) remained the largest solar telescope in space. Sequences of high-resolution multispectral images obtained in the spectral range of 380–670 nanometres during 10 years of continuous operation of the telescope are the best and longest time series of solar granulation images ever seen ☺.

Figure 6 shows a schematic view of SOT components and diffraction limited angular resolution of SOT (in blue) in comparison with that of Hubble ST (in red). The Gregorian design of SOT ensures the direct access to the primary focus which allows for a heat dump mirror (HDM) and a field stop to be placed there in order to reject the excess heat and reduce the amount of scattered light in SOT interiors. The secondary mirror is 17 cm large and the primary-secondary mirror length is 1.5 m. The light obscuration by the secondary mirror makes up only 12%.

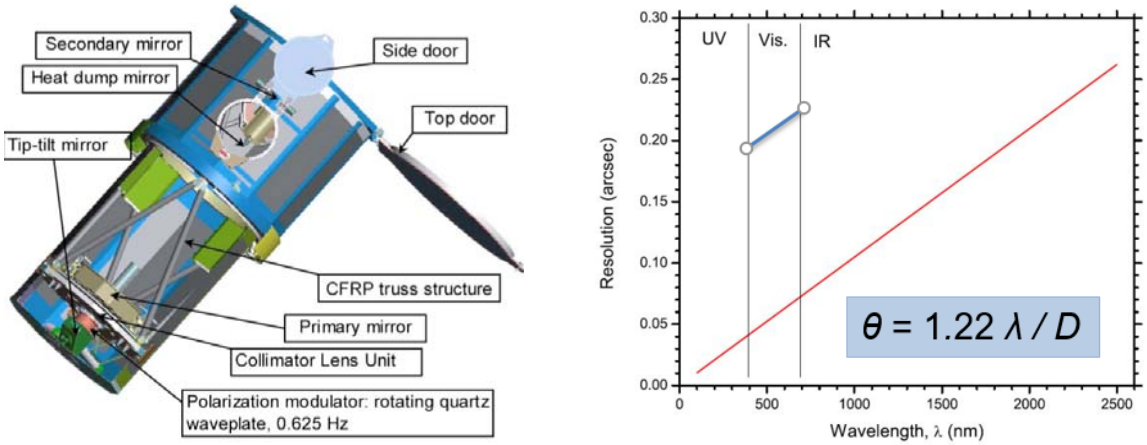

Figure 6. Overall view of SOT (left) and diffraction limited angular resolution: SOT vs HST (ri)

The SOT aplanatic optical system shown in Figures 7 and 8 is corrected for the spherical aberration and coma. In addition, an astigmatism correction lens (ACL) is built into the system to correct for the astigmatism of catoptric elements. The field curvature is not corrected. Due to the relay lens error the Broadband Filter Imager (BFI) has a chromatic aberration which was unexpectedly recognized after the Hinode launch. The impact of chromatic aberration on the image quality is relatively small (4 steps or 21 nm rms, with focus adjustment), but not negligible (Ichimoto et al. 2008). Most optical elements of SOT are made rotationally symmetric to minimize instrumental polarisation. Both, primary and secondary mirrors of SOT are made of lightweight ultra-low expansion glass, which exhibits no dimensional changes under extreme temperature fluctuations (eoPortal 2019).

SOT consists of two optically separable parts (Tsuneta et al. 2008):

1) Optical Telescope Assembly (OTA) including primary and secondary mirrors with HDM and a collimating lens unit (CLU), a polarisation modulation unit (PMU) and an active tip-tilt mirror (CTM-TM).
2) Focal Plane Package (FPP) housing a narrow-band (NFI) and a broad-band (BFI) filtergraphic imagers, a spectral polarimeter (SP) working at a pair of photospheric magnetically sensitive lines of FeI at 630.15 and 630.25 nm, and a correlation tracker channel (CT) which minimizes jitter and stabilizes solar granulation images on the focal plane CCDs by steering the tip-tilt mirror (Shimizu 2008).

The reimaging (relay) lens unit in the upper-left corner of Fig. 7 serves as an optical interface between the OTA and FPP parts and compensates for the shift in the focal plane, thereby improving the SOT focusing performance. SOT is a joint development in collaboration between JAXA and NASA, in which Japan supplied the OTA optics and the USA manufactured the FPP.

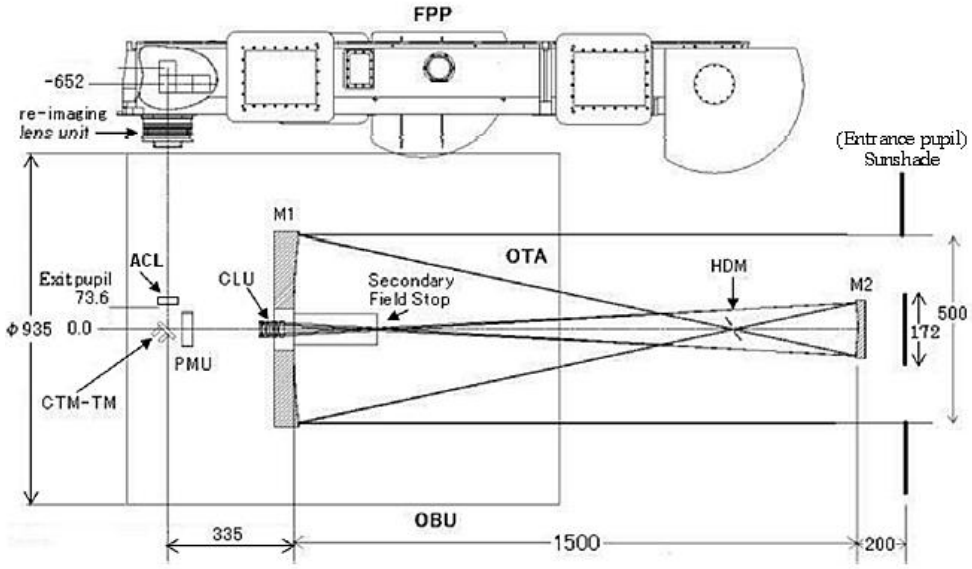

Figure 7. SOT optical configuration (OTA-OBU Part, © JAXA)

SOT consists of two optically separable parts (Tsuneta et al. 2008):

3) Optical Telescope Assembly (OTA) including primary and secondary mirrors with HDM and a collimating lens unit (CLU), a polarisation modulation unit (PMU) and an active tip-tilt mirror (CTM-TM).
4) Focal Plane Package (FPP) housing a narrow-band (NFI) and a broad-band (BFI) filtergraphic imagers, a spectral polarimeter (SP) working at a pair of photospheric magnetically sensitive lines of FeI at 630.15 and 630.25 nm, and a correlation tracker channel (CT) which minimizes jitter and stabilizes solar granulation images on the focal plane CCDs by steering the tip-tilt mirror (Shimizu 2008).

The reimaging (relay) lens unit in the upper-left corner of Fig. 7 serves as an optical interface between the OTA and FPP parts and compensates for the shift in the focal plane, thereby improving the SOT focusing performance. SOT is a joint development in collaboration between JAXA and NASA, in which Japan supplied the OTA optics and the USA manufactured the FPP.

The entire optical scheme of SOT is pretty complex (Figure 8). It includes catoptric (mirrors), dioptric (lenses, prisms, plane-parallel plates like filters), dispersive (gratings, prisms), polarizing (modulators, beam splitters), mechanical (shutters, slits, field stoppers) and optoelectronic (CCD arrays) elements. It has been a challenge to design, align, and tune all elements of the optical system, and it is challenging to keep them adjusted during the long-term operation of the system in the extremely variable environment. Only the OTA-BFI and CT channels marked in red-yellow-green in Fig. 8 are of practical interest for the present study.

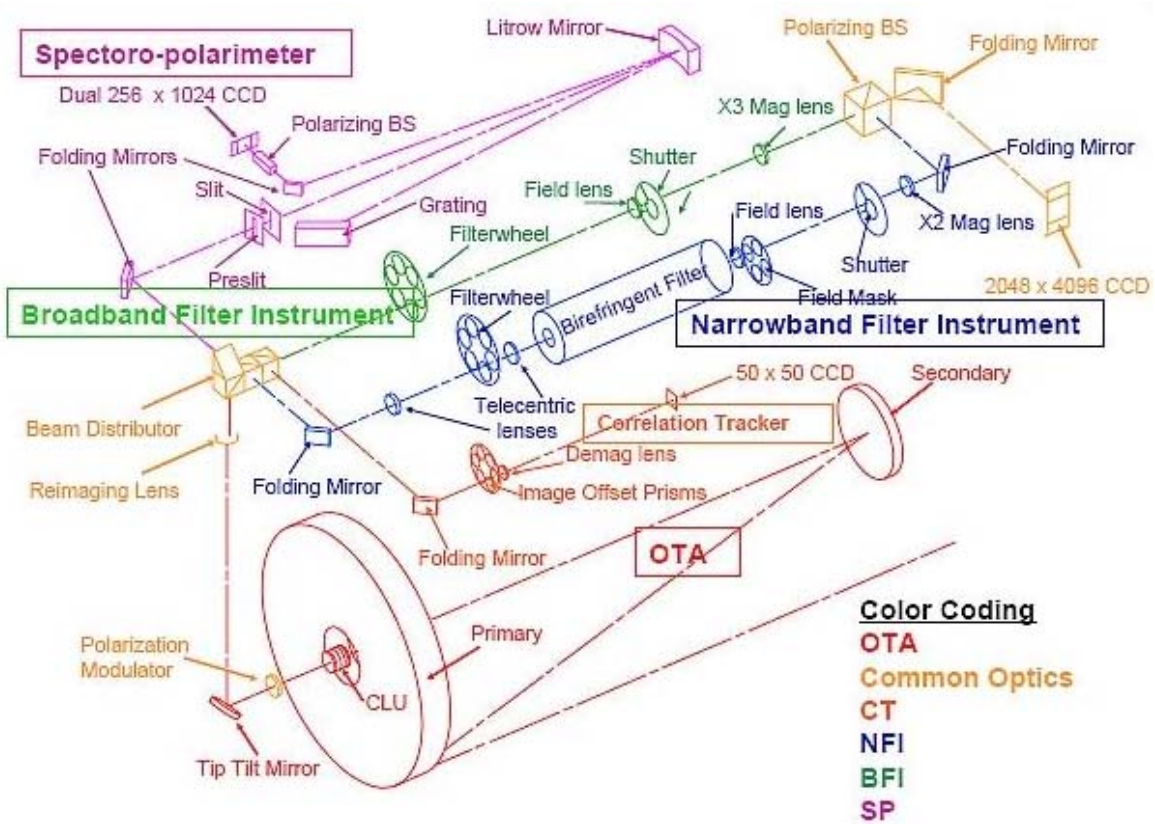

Figure 8. Entire optical scheme of SOT (© NAOJ 2011)

The broadband filter imager (BFI) includes a user-steered wheel with six interferential filters and delivers photometric, almost monochromatic images of the solar surface with the highest spatial and temporal resolution in 6 different spectral bands including CN I, Ca II H and CH I bands and three continuum windows at 450.45 nm (blue), 555.05 nm (green) and 668.40 nm (red). The continuum channels with the band width of 0.4 nm are suited to the measurement of the plasma movement and temperature in the photosphere. Measurements in the short-wavelength “line” bands permit identification of sites with strong magnetic field. Filtergrams (FG)[18] are recorded with the dedicated 4k x 2k frame transfer CCD camera, which is located in the focal plane of the BFI channel.

This is a dual large-format camera that consists of two adjacent CCD arrays, each with 2048 x 2048 pixels. The full-well capacity of both sub-arrays is 130.000 e-, which ensures a

[18] Filtergram is a BFI image that was recorded in one of six narrow spectral bands.

significant dynamic range and a linear response to the light signal.[19] The BFI CCD camera is characterized by low dark current (< 1 nA), high exposure efficiency and correctness. Exposure times are typically 0.03 - 0.8 sec, and the cadence between image takes can be as short as 5 to 10 seconds. The CT channel has its own CCD detector with 50 x 50 pixels, 0.22 arcsec/pixel and an error signal accuracy of 0.01 arcsec within the displacement range of ± 5 pixels.

The Hinode-SOT operates close to the diffraction limit and has a small albeit anisotropic contribution of stray light (Wedemeyer-Böhm 2008). Its point spread function (PSF) is very stable and only 1% wider than that of an ideal optical system described by the Airy function.[20] The PSF is a function with which the sharpness characteristics of the optical telescope and the individual elements of its optical system are assessed. Optical aberrations and contamination of optical elements as well as jitter, tracking and pointing errors, and scattered light expand the PSF, which leads to a reduction in image resolution, sharpness and contrast toward the edge of the field of view. A complete description of the complex optical system, such as SOT including multiple components, requires a range of PSFs. For SOT, the dominant terms in the PSF were derived from the Fourier spectrum of the physical aperture and empirically determined during partial solar eclipses and the Mercury transit in November 2006.

2.3 SOT orbit, coordinate system and stabilization

The Hinode satellite is placed in the sun-synchronous circular dawn-dusk orbit with the altitude of 680 km, inclination of 98.1°, revolution period of 98 minutes and the local time of descending node at around 6:00 p.m. The orbit is synchronised in relation to the Earth's revolution around the Sun, so that the spacecraft is exposed to the continuous sunlight for at least 9 months a year during the planned three-year mission[21]. A solar eclipse season lasts from the beginning of May to the beginning of August, in which a night period with the longest duration of 20 minutes takes place in each orbit period. Significant fluctuations in the surface temperature of the spacecraft during day-night cycling lead to periodic thermal deformations and a large focus drift (~ 12 steps) occurs in each orbit approx. 30 minutes from the dawn. Such behaviour has been predicted. Nevertheless, the eclipse season was referred to as “certainly a degraded performance period for SOT” (Al-Janabi et al. 2019).

Figure 9 shows the Hinode orbit and illustrates the change in the line of sight (LOS) to the sun disk centre with the movement of the spacecraft along the orbit. The diameter of the Hinode orbit ($2a$) is 14.100 km. In the SOT solar images obtained from the opposite points of the satellite orbit, the lines of sight differ by 20 arc seconds. This is important with regard to the short-term focus changes with change in pointing.

The relationship between the heliocentric coordinate system and the Hinode BFI-CCD image coordinate system is described in (Shimojo 2006) and shown in Fig. 9 (right), in which the elements of the heliocentric system are shown in black and those of the BFI image coordinate

[19] The dynamic range of a CCD is defined as the full-well capacity divided by the camera noise and relates to the ability of a camera to record simultaneously very low and bright light signals.

[20] Airy disk in the image plane.

[21] The planned duration of 3 years was extended to 13 years. It is expected that the sun-synchronous condition will be maintained until at least 2020 without any orbital manoeuvres.

system - in blue. X and Y denote coordinates of an image pixel in the heliocentric coordinate system, while CCD image coordinates of the same pixel are specified as nxCCD and nyCCD. Θ is the offset angle of the Y axis of the heliocentric coordinate system and the Y axis of the CCD. XoffAT and YoffAT are the offset values between the SOT FOV center and the CCD center in the heliocentric coordinate system. Heliocentric coordinates of the centre of the CCD FOV (image) are specified in arc seconds in the header of each BFI image as Xcen, Ycen.

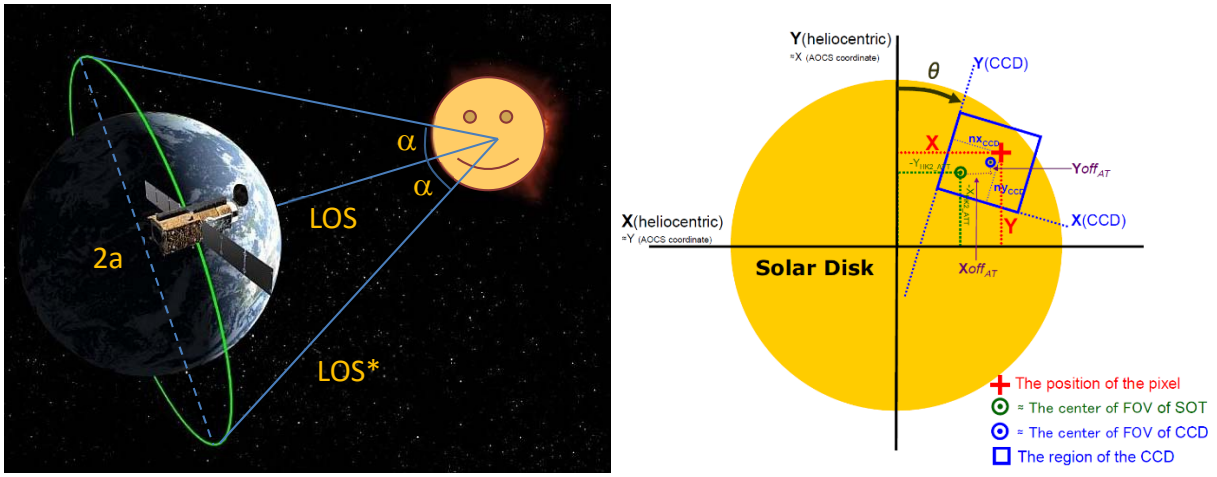

Figure 9. Hinode orbit and lines of sight (left), and Hinode image coordinate system (right)

The Hinode BFI images are taken under relatively stable pointing conditions. The Hinode SOT stabilization is achieved by a combination of the satellite attitude control system, structural design and active image stabilization. The Hinode spacecraft is stabilized in three axes with the aid of attitude and orbit control system (AOCS). Its Z-axis points to the Sun (Fig. 5) and is aligned with the SOT FOV centre. The AOCS uses four momentum wheels as the actuators, two ultra-fine sun sensors for determining the solar direction with sub-arcsec accuracy, an inertial reference unit of four gyros for detecting temporal changes of attitude, and a star tracker for determining the roll of the spacecraft (eoPortal 2019). In the AOCS coordinate system, the X and Y axes point in the solar east-west and north-south directions, respectively. The Sun pointing stability with AOCS is given as 0.1 arcsec.

Even with AOCS stabilization, BFI image sequences of solar granulation suffer from the jitter of the spacecraft, which was measured as 0.1-0.2" (σ in 10 s) and 0.3" (σ in 60 s), i.e. too much for SOT observations. A further image stabilization of 0.02 arcsec is achieved for SOT using its own correlation tracker and a piezo-driven tip-tilt mirror system. The TTM system operates in a closed-loop servo using the displacement error that is estimated from the correlation tracking of the solar granulation. In (Al-Janabi et al. 2019) the SOT image stability when the CT is switched on is characterized with 0.01 arcsec rms in both X and Y directions.

No jitter from moving mechanical parts of the BFI, such as filter wheel and shutter, or from continuously rotating wave plate of the PMU was recorded. However, the visible-light shutter of XRT produces a jitter of SOT images with the magnitude of 0.4'' rms during its operation. However, the visible light shutter in XRT produces a jitter of SOT BFI images with a magnitude of 0.4'' rms during its operation. The influence of XRT-induced jitter on long-term SOT observations is believed to be small due to the short-term (~ 0.5 s) and sporadic nature of its use. Besides, it was found that the spin speed of the impulse wheels, normally 1800 rpm, shows a gradual drift and the high frequency micro-vibration excited by the wheels can lead to

a rather large jitter of SOT images on the order of 0.3" (3σ) when the speed reaches 2200 rpm. To avoid such a deterioration in performance, the speed of the momentum wheels was reset every 3 to 4 years.

Another technical problem concerns the irregular heating, weathering and aging of Hinode structural elements, which distorts the optical system and affects the focusing performance of the SOT. In ten years of SOT operation, the focus position has gradually drifted from its original position. It is believed that such gradual drift is mainly caused by dehydration shrinkage in the space of the carbon fibre reinforced plastic truss tubes that connect the primary to the secondary mirror of the telescope. The focus's gradual drift almost ended after 2011, when dehydration of the truss slowed down and the temperature of the OTA became stable through heating control (Muller et al. 2018, Al-Janabi et al. 2019). The focus correction was certainly required and carried out during the SOT operation from 2006 to 2010.

Long-term changes in the best focus position are compensated for by stepwise moving the reimaging lens[22] in the FPP, which can only be managed by the ground control. The entire range of motion of the reimaging lens is given as 25 mm or 150 steps (0.17 mm step^{-1}). The largest drift in focus of 12 steps was caused by day-night heating effects. The short-term changes in the focus position due to changes in the pointing or / and cyclical warming of the spacecraft in the eclipse season must be corrected by image processing. In (Muller et al. 2018) no focus correction was performed for the Hinode image data taken after January 2012.

The annual change in the distance between the Sun and the Earth influences the pixel scale in BFI digital images and must be taken into account for precise granulometric analyses. An approximate expression for the temporal variation of the Sun-Earth distance *r* can be derived from Kepler's laws of orbital motion as

$$r \cong a \cdot (1 - e^2)/(1 + e \cdot cos(\nu)) \,, \tag{15}$$

where *a* = 1 AU is the semi-major axis and *e* = 0.0167 is the eccentricity of the earth's orbit around the Sun.

Then the Sun-Earth distance in astronomic units can be written as

$$r \cong 0.99721/(1 + 0.0167 \cdot cos(\nu)), \ [AU]. \tag{16}$$

In equations (15) and (16) ν is the true anomaly given as a function of time in the form

$$\nu \cong dt \ \cdot 360° \ / \ 365.25 \ = \ 0.9856 \cdot dt \,. \tag{17}$$

Here, *dt* is time in days since perihelion.

For practical calculations of the pixel scale in Hinode image time series, the closest perihelion time must be known as an epoch. In our case, this was on January 4, 2006 at 3:30 p.m. UCT. Note that all equations from (15) through (17) are approximate expressions since they don't account for the gravitational perturbation of the Earth orbit[23] and the increased velocity of the orbital motion around the perihelion. Nevertheless, they can safely be used in the present study

[22] The reimaging lens in FPP is often referred to as a focussing lens.

[23] By the Moon and other planets.

since the total variation of the Sun-Earth distance does not exceed 1.5% and the direct influence of orbital perturbations on the Hinode BFI pixel scale is negligibly small. [24]

Solar heating of SOT is also a problem for long-term observations of the solar surface because it affects the stability of the optical system and the image quality. In order to protect the optical telescope from overheating and overcooling and to stabilize the OTA temperature, an efficient system for thermal control was developed (Fig. 10). This includes sub-systems for passive control using multi-layer insulation (MLI), heat dump mirror, coatings, sunshades, radiators, shutters, thermal and X-ray filters, low-expansion materials, etc. and active control using cooling plates, louvers and operational heaters.

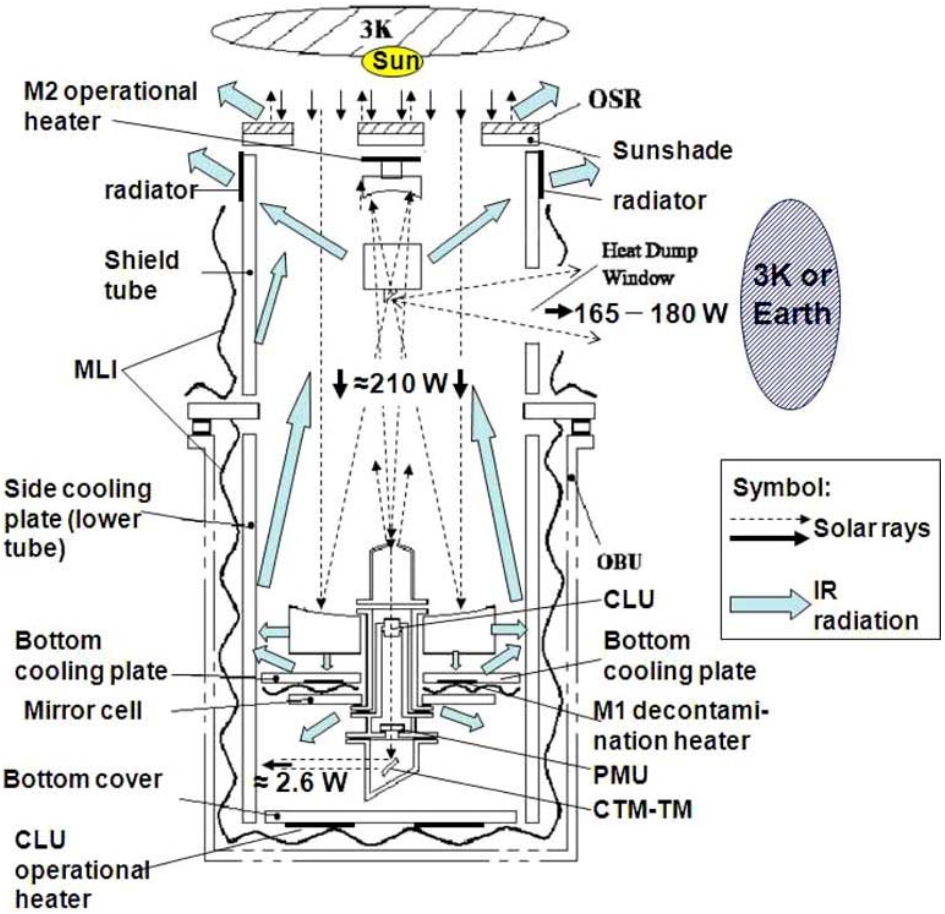

Figure 10. SOT thermal control system (© NAOJ / JAXA)

Not all SOT elements can be made from ultralow-expansion materials. Uncompensated heating therefore leads to a thermal deformation of SOT constructions, which affects the image quality on the focal plane CCD. Alternating processes of heating and cooling during the eclipse season bring about essential difficulties, especially when the thermal deformation of the heat dump mirror cylinder and its supporting spider leads to a displacement of the secondary mirror (M2). About 1% of the incident solar energy (~ 2.6 W) spreads into the FPP block. In addition, there are internal heat sources in the FPP, such as CCD cameras that use high voltage and generate heat. For this reason, each CCD camera is supplied with its own radiator. However,

[24] Hypothetically, gravitational perturbations due to the variable constellation of solar planets can influence the sun activity cycle.

micro-deformations that lead to unevenness in the CCD surface cannot be excluded. Irregularities on the sensor surface and shear of the sensor matrix can in turn lead to local image distortions and blurring.

Also contamination of open optical surfaces with interstellar matter and operational residues affects SOT performance and deteriorates CCD sensitivity. It was reported that, at the beginning of 2011, the light throughput in the blue continuum channel became about 77% of the initial value; accordingly, the signal-to-noise ratio has gone down to 80%. The baking of the FG CCD did not help in recovering the throughput (Hinode review team 2019).

It should be noted, however, that all these effects are sporadic rather than general in nature. They can deteriorate the quality of individual images, but they cannot degrade the value of long-term image time series. For this reason, the Hinode BFI image series collected in various international archives are still of constant interest to scientists and are warmly mentioned by numerous users. Today they are simply the best.

2.4 Characteristics of Hinode blue continuum images

Three Hinode BFI continuum channels, including

- the blue continuum channel (B) centred at 450.45 nm,
- the green continuum channel (G) centred at 555.05 nm and
- the red continuum channel (R) centred at 668.40 nm,

all have the same spectral width of 0.4 nm and can be used in combination or separately for imaging the photosphere and for measuring the photospheric temperature. Three other “line” channels are used to map magnetic network and to study chromospheric heating.

The blue continuum radiation of the Sun originates from the deepest layers of the solar atmosphere / photosphere, which are the closest to the uppermost part of convection zone. Naturally, the appearance of solar granulation in the blue continuum window is somewhat different from that in the green continuum because we are looking at a different height (Zirin 1988). The image resolution and the granulation contrast are at the highest level in blue continuum scenes. However, observations at 450.45 nm clearly represent the magnetic network elements that can deteriorate the results of the automatic morphometric analysis.

In Section 2.1 it was pointed out that the influence of the chromatic aberration in the BFI channel with a magnitude of 21 nm rms (4 steps of the reimaging lens motion) cannot be neglected. Indeed, chromatic aberration cannot directly affect the sharpness of blue continuum images obtained in a very narrow spectral window with $\Delta\lambda$ = 0.4 nm. However, the position of the BFI focal plane is controlled in the G-band (Muller et al. 2018), and in the blue continuum channel this position can be different just due to the influence of the chromatic aberration. This can result in defocusing and blurry images.

The pixel scale of original BFI grayscale images is given as 0.054 arcsec while the diffraction-limited resolution in continuum channels is approx. 0.2 arcsec. The full field of view (FOV) is 220’’ x 110’’. The pixel depth was given as 16 bits which is important for high-precision photometric measurements of the granulation contrast. Due to the limited bandwidth of the

downlink in the S-band (262 kbps)[25], however, the image data must be compressed on board in the pixel depth, e.g. from 16 to 12 bits (16- to 12-bit compression). The compression ratio is strongly dependent on the image nature. For example, SOT filtergram data is typically compressed to 8 bits per pixel by the JPEG discrete cosine transform, which is not a lossless compression (Al-Janabi 2019). 24-bit RGB images can be obtained by combining 8-bit data from three continuum channels.

Tight telecommunication constraints forced a further reduction in the number and volume of image scenes transmitted to the Earth. Accordingly, BFI images were binned[26] by a factor of two so that the new size of filtergrams taken after February 19, 2008 was reduced from 4096 x 2048 pixels to 2048 x 1024 pixels. Hence, the actual angular resolution of the images taken after February 2008 was lower by a factor of 2 and the pixel scale of the newly taken images was given as 0.108 ". Still, this size is twice smaller than the value of the diffraction limited resolution. All images obtained before the 29th January 2008 were larger in size and had a higher spatial resolution.

No FG scenes are available for the period from January 28, 2008 to February 20, 2008. BFI data are also not available between April 8 and June 1, 2008. For the whole year 2013 with high solar activity, only 30 FG scenes are available. With this one can state that the temporal coverage of the 10-year observation period with Hinode BFI data is characterized with essential gaps in years 2008 and 2013. Further information on the BFI image parameters can be found in the Hinode SOT Data Analysis Guide v. 3.3 (Berger & Slater 2009).

For the practical work in the frameworks of this thesis I got an access to the IGAM database containing long-term series of Hinode-SOT Level 1 image data obtained in the blue continuum channel centred at 450.45 nm. The database occupies 52.8 Gb on a hard disk and contains a total of 3.398 BFI FG full-size files that are saved in the *.fits format. Each * .fits file in the database contains the primary header with descriptive metadata and the data unit in which the image itself is stored in binary form. The file header describes the origin, size, format, coordinates, processing history, and other information about the image data. Also the position of the frame centre in the heliospheric coordinate system and the position of focussing lens in the FPP block can be found for each image in the associated header. All FITS keywords used in the Hinode FG header are explained in detail in (NAOJ 2008, version 20080122).

The first scene in the database is dated December 1, 2006 and the last one is of February 19, 2016. Most scenes originate from the Hinode synoptic observation program. During the synoptic Hinode program, BFI images of the solar disk centre were usually taken once or twice a day.

Hinode FG Level 1 data are fully calibrated data in *.fits format[27] that can be used directly for scientific analysis (Sakurai 2008). Therefore, I think that the Level 1 data set in the IGAM database is the automatically calibrated sequence of data, which contains all scenes that were

[25] The X-band downlink channel with the bandwidth of 4 Mbps has not been available for telecommunications since the beginning of 2008.

[26] Image binning is a form of image resampling (quantization) in which the original data values which fall into a given small interval, a bin, are replaced by a value representative of that interval, often the central value. This is a data pre-processing technique used to reduce the effects of minor observation errors.

[27] FITS (Flexible Image Transport System) is a standard format for astronomical data sets.

originally obtained from the SOT-BFI sensor. The same data set was initially available to the authors of (Muller et al. 2018).

From an observational point of view, this is the best available data set for the investigation of solar surface convection, measurement and statistical analysis of granulation parameters, since it represents the solar granulation with the highest contrast and the highest spatial resolution under seeing-free conditions over a period of 11 years, which corresponds to the duration of the solar cycle. Observations of solar granulation in the blue continuum channel are also valuable because the continuum radiation is formed closest to the surface convection layer and the images of solar granulation recorded in this channel are easy to interpret because the radiation physics is well understood there.

All images in the IGAM database were taken with the same instrument and have the same size and the same system of annotations in the file header. All images were subjected to the same calibration procedure. So they could be processed in an equal manner with the same processing tools. On the other hand, this was a “Big Data Set” and I had to go through everything carefully because it also contained blurry images. Figure 11 shows two consecutive Hinode blue continuum images from the IGAM data set including sharp FG20070710 and blurry FG20070711.

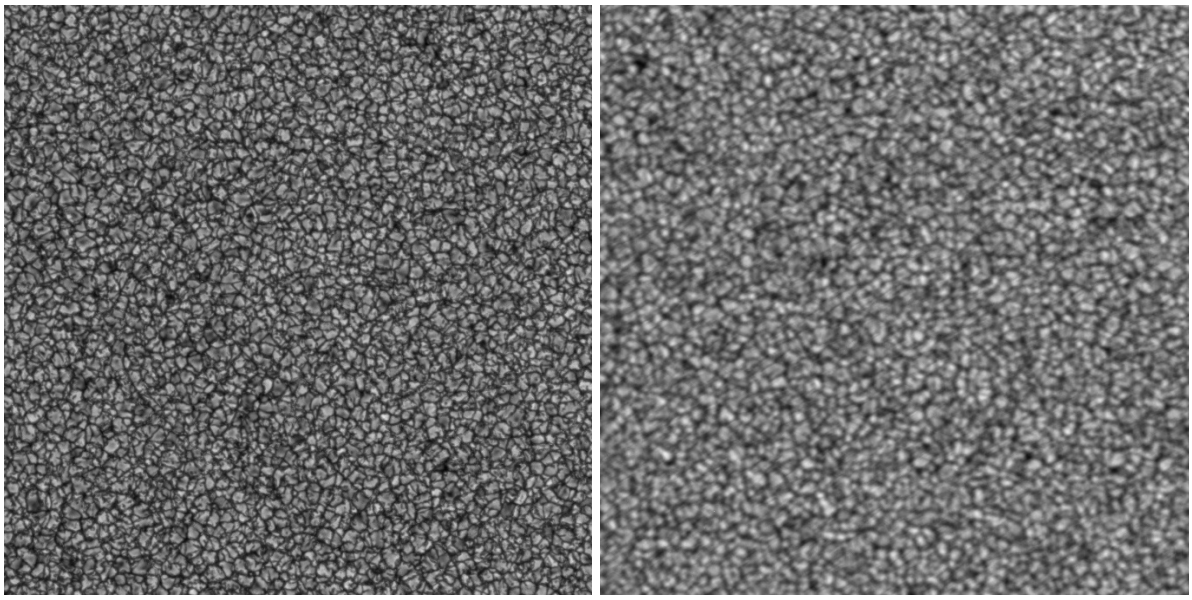

Figure 11. Two consecutive blue continuum images from the IGAM data set: sharp FG20070710 (left) and blurry FG20070711(right)

In the present study, only high-quality images recorded in the BFI blue continuum channel were used. The main focus was on the granulometric analysis of the BFI grayscale images, which were taken over the sun disk centre under non-magnetic conditions of the "quiet sun". All Hinode images with sun spots, pores, abnormal granulation28 and other magnetically active features had to be excluded from the analysis. In order to look through almost 3.400 scenes and check their quality, they had to be visualized.

[28] Abnormal granulation is a granulation area that appears smeared by the presence of many magnetic bright points in the intergranular lanes. The granulation contrast is reduced in such areas that also occur in quiet-sun regions (Muller et al. 2017).

2.5 Image visualisation and quality control

On September 3d, 2019 I have visualized the very first scene FG20061201_190556.7.fits[29] from the original data set with the MATLAB software package v.2017b[30]. MATLAB is my preferred tool because I learned and liked it during my master's degree at Graz University of Technology. The visualisation of this first Hinode FG scene took some time. Hence, before I started visualizing the entire set, I had a look through the annotations in the file headers[31] and red some publications about the peculiarities of Hinode image pre-processing (Hanslmeier et al. 2010, Yu et al. 2011).

So, I recognized that all images in the IGAM database were previously calibrated with the standard solar reduction procedure which is implemented in the SolarSoftWare (SSW) and distributed under SSWIDL. This calibration procedure (fg_prep) corrects for bad pixels, readout errors, dark current, flat fielding and stitching (Muller et al. 2018). The data list shows, however, that the original data set contains images of two different sizes, either 32.8 MB (1121 scenes, i.e. almost the first third of the images) or 8.2 MB (2277 scenes). This is due to the accident with the X-band datalink in January 2008 and the subsequent compression and reduction of images on board the Hinode (see Section 2.1). All images feature the pixel depth of 8 bits regardless of the image size.

No BFI scenes are available between January 28, 2008 and February 20, 2008. BFI filtergrams are also not available for the period from April 8 to June 1, 2008. For the whole year 2013 with high solar activity, only 30 FG scenes are available. There are also numerous short-term gaps lasting several days. With this it can be noted that the temporal coverage of the 10-year observation period with Hinode BFI data has significant gaps, especially in the years 2008 and 2013.

The next image for the visualization was selected from the second half of the original data set. Given the smaller size of the second image, rendering the second scene in the MATLAB environment took much less time. MATLAB is good for algorithmic design and statistical processing of long image series. However, displaying long image time series with the MATLAB is neither comfortable nor sensible. In this regard, it is inferior to any other image viewing software such as Adobe Image Viewer et al.

For this reason, I used the 64-bit IrfanView v. 4.54 software to look through all available Hinode BFI image data in detail. This freely available viewer only runs on 64-bit Windows but can read, display and convert FITS images to other image formats such as TIFF. It can load very large scenes and display long image sequences and enables detailed viewing (zoom) with direct addressing of the image to be displayed. And it is fast and efficient. An official IrfanView homepage can be accessed at https://www.irfanview.com/ .

With the IrfanView I created for the first time a slideshow of multitemporal BFI images with the automatic slide feed after 0.25 seconds. It was a pretty exciting, albeit somewhat tedious show, which lasted 15 minutes. Then I repeated the slideshow with a longer cadence between the

[29] The name means that the filtergram was taken on December 1st 2006 at 19:05:57 UCT.

[30] MATLAB (matrix laboratory) is a numerical computing environment and programming language developed by MathWorks. I used a student version of this software, License No. 61172.

[31] All file headers were read with the Microsoft WordPad in Windows 10.

slides. This time, the show showed that the entire image sequence contains images representing peripheral parts of the Sun including the solar limb, images with sunspots and separate pores, and faulty images, e.g. images with different brightness in the left and right sub-fields as shown in Figure 12. There were images with very low contrast, very dark images, images with stripes and many blurry images. Such scenes had to be rejected from the dataset. In (Muller at al. 2018) almost 25% of all Hinode images were removed because of defocussing problems.

The analysis of almost 800 file headers revealed that there are many scenes that are offset by tens of angular seconds from the disk centre in both the X and Y directions. If they are small, such displacements are not visually recognizable. However, they influence the average size of the solar granulation shown in these scenes. This effect is commonly referred to as foreshortening. To avoid geometric complications in data processing, all FG scenes shifted from the disk centre by more than 0.25” were excluded from further analysis.

The blurring of Hinode images is probably the most disturbing feature, as it occurs frequently and apparently randomly and is not easily detectable with the naked eye on the computer monitor. There are global blurs that affect the sharpness of the entire image, as well as local defocusing effects that are reflected in part of the image. On closer inspection using the IrfanView zoom option, I found that local defocus effects occur more frequently in the right subfield of the FG scenes than in the left subfield. In view of the sporadic occurrence of such effects, this indicates temporary instrumental shortcomings, e.g. those related to overheating of the focal plane CCD. This finding is consistent with other observations.

For example, the comparison of Hinode blue continuum images taken at the same distance from the disk centre showed that they are not always of the same sharpness (Muller et al. 2017). The same authors analysed the location of the CCD frame centre with respect to the limb position and found that the heliospheric Xcen and Y cen coordinates of the frame centre, as determined by the correlation tracker and specified in the file header, were often incorrect.

It can therefore be assumed that, apart from instrumental effects, an irregular or partial defocusing and tracking errors can also be caused by certain "seeing conditions" or transient features in the overlying layers of the solar atmosphere / chromosphere that perturb the propagation of the short-wave optical radiation and thereby influence focusing and tracking of Hinode images. One could call that solar atmospheric refraction. With this thought one approaches the hypothesis devised by Sir W. Hershel, who suspected the presence of clouds in the solar atmosphere, which partially obscure solar surface.

Another interesting observation made with IrfanView in Hinode BFI images is that of dark extended lineaments that cut apart individual granules as shown in Figure 13. These are chromospheric features that leave traces in photospheric blue-continuum images (Zaqarashvili, personal communication 2019). Consequently, the presence of atmospheric objects casting “shadows” on the solar surface is not an impossible invention. However, such objects are rather singular in quiet-sun regions and their influence on the total number of granules to be measured is negligible.

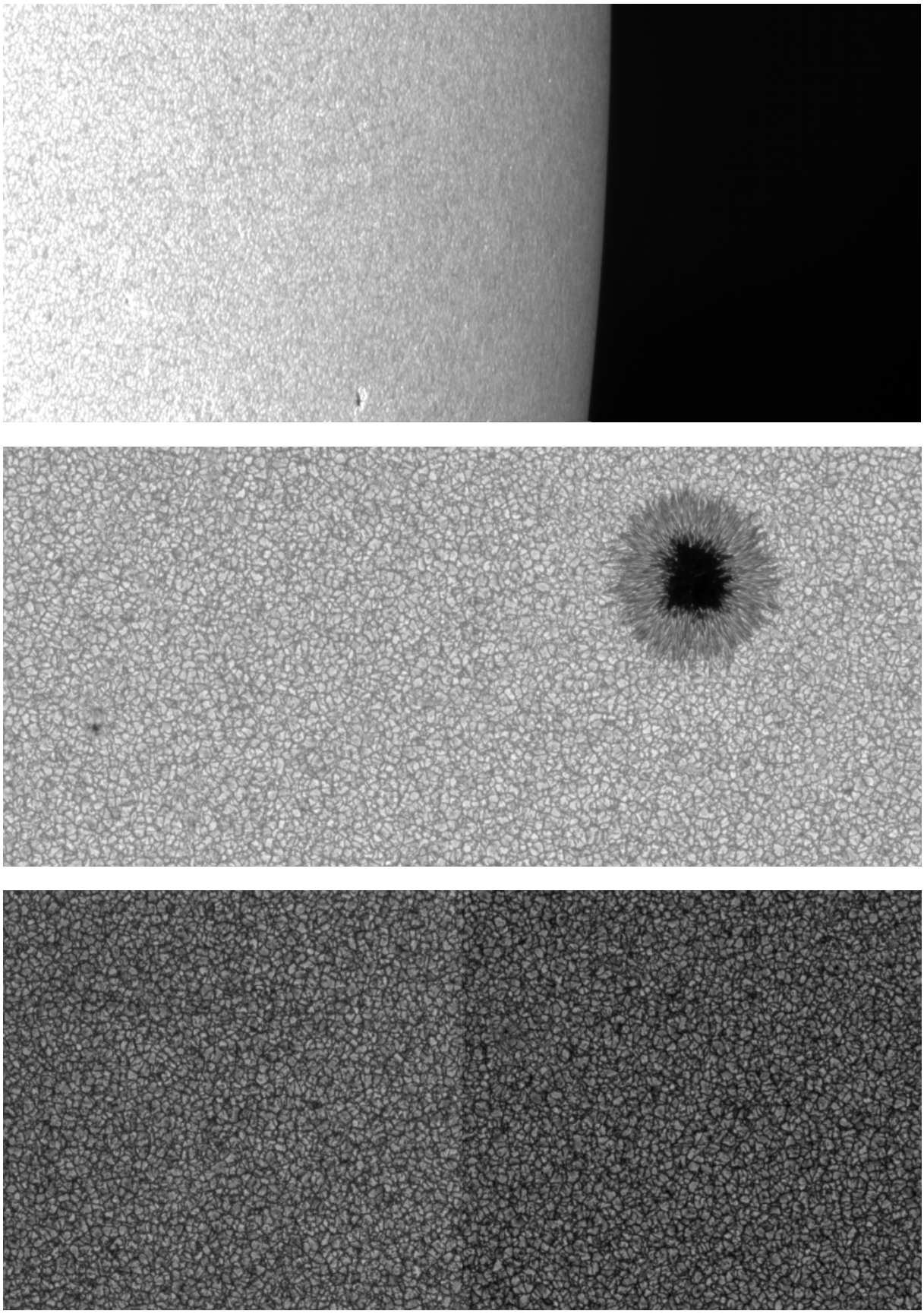

Figure 12. Solar granulation in the limb area (FG20141128, top), around sunspot (FG20070204, mid), in the area of image stitching defect (FG20070719, bottom)

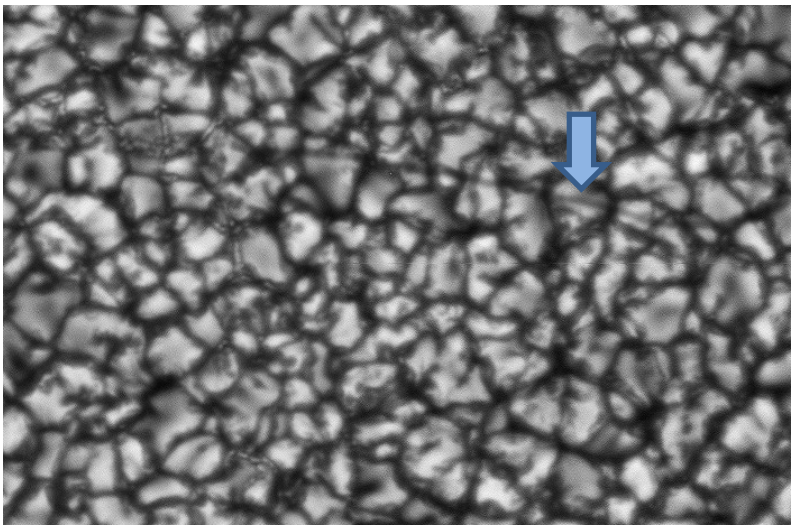

Figure 13. Dark extended lineament on FG20061227 (marked with an arrow)

In contrast to singular effects, it was assumed and later proved that the influence of blurred images on the results of the granulometric analysis is widespread and significant. Therefore, all images that were clearly out of focus, as well as those that contained sunspots, isolated pores, or abnormal granulation, were excluded from the analysis. As a result, a reduced data set was created with almost 2500 high-quality BFI images taken in the blue continuum channel at the quiet-sun disk centre between December 2006 and February 2016.

Also the reduced data set contains BFI images with different sizes of 4096 x 2048 pixels and 2048 x 1024 pixels. Most scenes in the reduced data set were taken either around 6:00 am or around 6:00 pm UCT. All scenes have 8-bit pixel depth.

2.6 Construction of image time series

Even after removing all flaw and improper scenes, the total number of Hinode BFI images suitable for the granulometric analysis is too large to be processed in a single study. On the advice of Prof. Hanslmeier, I concentrated on processing several representative sequences of Hinode high-quality images that cover different periods of time with different cadence. A total of seven Hinode image time series (HITS) with at least 90 images each were created and processed.

The list of HITS includes

- two *monthly time series* with a cadence of 30 days for the statistical analysis of granulation characteristics in comparison with the monthly mean number of sunspots,
- two *synodic time series* with a cadence of 27 days for the visual analysis of video sequences representing the dynamic behaviour of the granulation pattern and for the estimation of granulation parameters taken over the same area on the solar surface,
- three *daily time series* with cadence of 1 day for the statistical analysis of granulation characteristics in comparison with daily sunspot numbers.

Some statistical properties of the high-quality HITS can be derived from Table 1. Time series with low-quality images are not included. Monthly and synodic HITS were generated in pairs,

so that “basic” HITS were temporarily shifted with respect to the “other” time series by about 13 days, which corresponds approximately to half of the solar equatorial rotation period. The granulometric results obtained with “other” HITS were used to validate those obtained with “basic” time series.

Table 1. The list of HITS and their characteristics

HITS Name	Cadence, days	Start scene	No. of scenes	Processing date
HITS-30-basic	30	FG20061215	94	14.10.2019
HITS-30-other	30	FG20061202	94	17.10.2019
HITS-273-basic	27	FG20061215	104	05.11.2019
HITS-273-other	27	FG20061201	107	21.11.2019
HITS-2011-1234	1	FG20110101	118	03.12.2019
HITS-2012-1234	1	FG20120101	105	28.11.2019
HITS-2015-1234	1	FG20150101	88	04.12.2019

The total number of scenes in the monthly and synodic HITS is determined by the corresponding cadence and the number of available high-quality images in the reduced data set, and not by computational limits. The number of scenes in the daily HITS is determined both by the availability of high-quality images and by the computing time. In my case, the computational load limit set by the PC capabilities is approximately 120 full-frame scenes with 2048 x 1024 pixels.

All scenes with the size of 4096 x 2048 pixels that were included in HITS were resampled with the Lanczos filter to the smaller size of 2048 x 1024 pixels. The Lanczos filter available in IrfanView works slower than B-Spline filter, but offers better photometric quality, which is comparable to that of the JPEG DCT converter used on board the Hinode satellite (see Section 2.1). So all images in the resultant time series have the same size of 2048 x 1024 pixels. The HITS time series were then saved in TIFF format[32] without further compressions in order to enable Windows-based documentation and animation in the form of full-frame movies. The memory size of each TIFF image in the resultant time series is 2.049 KB.

The effective duration of the monthly and synodic time series is 9.25 years or 111 months, while the duration of the daily time series corresponds to the first 4 months or 120 days in the years 2011, 2012 and 2015. However, the actual number of scenes shown in Table 1 is less than the theoretical values of 111 for the monthly[33] and 120 for the daily series, indicating the existence of data gaps. This means that at least some sections of the time series have a variable sampling interval and the HITS are generally not regular but piecewise regular. In this concern, the daily time series are more regular than the monthly time series, the latter showing large time gaps of up to several months. Remember that there are only 30 FG scenes are

[32] A common Tag Image File Format (TIFF) enables lossless storage of 8- and 24-bit raster images (Veronig 2019).

[33] Regular synodic time series covering the observation period of 9.25 years should contain 125 scenes.

available for 2013. There are no scenes for December 2008 and June 2011, not even for the periods of April - May 2009 and September – December in 2012.

The daily HITS time series of 2011 and 2012 are fairly regular because they include the Hinode imagery taken during the seasons with moderate solar activity that had few days with sunspots and pores at the disk centre. In addition, the four-month periods from January to April are outside the Hinode eclipse season between May and August, ensuring that image data is less prone to artefacts and image defects such as blurring, defocusing, and interference disorder (see Section 2.2). The scale, resolution, and image contrast of the solar granulation are usually somewhat better in the BFI scenes that were taken from the position closest to the Sun, in January each year.

In the present study, daily and monthly mean time series of sunspot numbers for the period of Hinode operation in 1996 – 2019 were derived from the SILSO archive of the World Data Centre for SSN at the Royal Observatory of Belgium. The SSN data description can be found at http://www.sidc.be/silso/datafiles . In contrast to the HITS time series, the original SSN time series are regular because they have no gaps.

Both types of time series must be made comparable however. Therefore, the data gaps available in HITS were artificially inserted into the SSN time series. For example, daily SSN values were sampled with a 27-day interval for comparison with synodic HITS. The resultant SSN time series thus reflect all the time gaps available in HITS. In this context, it is unnecessary to present statistical parameters of the SSN time series in a separate table. The number of elements and cadence (typical sampling interval) in the resultant SSN time series are the same as in the HITS time series. Obviously, both types of time series represent stochastic processes with trends. In the case of HITS data series, it is not yet clear whether these trends are of natural or instrumental origin. Accordingly, the nature of the underlying processes is not entirely clear.

Besides, there is one more limitation to the use of SSN time series that was already mentioned in Section 1.1 and is related to the sections of SSN time series that were recorded during long periods of minimal activity in the solar cycle when the SSN index reached zero values. Such periods are not included in our daily HITS and SSN series. The daily series from 2011 and 2015 cover both the ascending and descending branches of the 24th cycle, while the 2012 series represents the season of the local maximum of solar activity in the current cycle. In this context, I would like to say that our daily HITS are seem to be the best choice from available data for comparative analysis with corresponding SSN series. Surprisingly, the selected seasons were examined to a lesser extent in granulometric studies than the period 2006-2010, which is characterized by minimal solar activity.

The overall quality of the HITS time series was again checked visually using slide shows with a scene advance of 0.25 seconds. All seven time-lapse video sequences were displayed under IrfanView v.4.54. Still images could be examined in detail under breaks using the zoom option.

The analysis of the video sequences showed no significant heterogeneity in the overall photometric quality of the HITS time series. No essential jitter was observed in the video sequences. An insignificant video flicker occurs due to the slightly different brightness of individual slides. An observer several meters away from the monitor can see dark spots with an irregular shape and the size of dozens of granules that resemble dark clouds moving across the field of view over the lighter surface. These “clouds” could be interpreted as the

manifestation of randomly superposed p-mode acoustic oscillations (McClure et al. 2018). I refrain from further comments due to the lack of expertise.

Under closer look at the animated synodic time series with a 27-day cadence, one can even see "downward" vortex movements and "upward" eruptive movements or granular fountains that look like daisy flowers, fireworks or molehills. The position of such features on the sun disk remains more or less constant. Their interpretation as an optical illusion is not improbable however. The line charts that graphically represent HITS time series are shown in later sections of this work. The animated HITS are available as supplementary material and can be provided on request.

Chapter 3. Algorithmic Design for Granulometric Segmentation

3.1 Image segmentation methods

The visual inspection of time-lapse video sequences is not appropriate for the precise quantitative granulation analysis of Hinode image time series. Hence an efficient algorithm and methodology, new or adopted, for the overall automatic segmentation[34], identification, accurate measurement and statistical parameterization of morphological properties of the solar granulation[35] in Hinode blue continuum images had to be developed, tested and implemented in the frameworks of this thesis.

There are four groups of methods known to the author that can be applied to the automatic segmentation and parameterisation of solar granulation in optical image time series:

- spatial- or image-domain methods of photogrammetric analysis,
- time-domain methods including time-slice and cross-correlation analysis,
- spatial-frequency-domain methods including spectral and wavelet analysis,
- combined methods.

Application of one or another method to processing long image time series depends on the statistical character of the process being investigated. Is it deterministic, stochastic, stationary or ergodic? Ergodicity of granulation continuum data was tested in (Hanslmeier et al. 2009) and it was deduced that the granulation is an (almost) ergodic phenomenon. This means that the morphological properties of solar granulation can be represented statistically with the same appropriateness either with ensemble averages or with time averages. In other words, spatial averages of the ergodic phenomenon can be substituted with time averages and vice versa.

Photogrammetric image analysis is based on methods of geometric and photometric processing of optical images and is the most traditional and established method of image processing that enables morphometric analysis of each and every granule represented in the examined image. It can be used directly for granulometric analysis of HITS time series in image-by-image mode. Another advantage of methods that operate in the image domain is the direct access to and the reliable quality control of the results.

Time-domain processing methods involve cross-correlation of subsequent images, analysis of time-slice diagrams and tracking procedures (Title et al. 1986). They are often combined with space-domain methods and are used for studying granular evolution, feature tracking and measuring horizontal velocities of convective flows (Müller at al. 2001). Granular and supergranular evolution was investigated by (Pötzi et al. 2000, Roudier et al. 2018) with so-called space-time slices, which are two-dimensional XT time series or composite images, with each image line (scan) X being recorded at successive, equally spaced points in time T. Time-related methods can also be used for cross-correlation analysis of the SSN time series and

[34] The concept of (granulation) segmentation means a process of separating objects (granules) from the background (intergranular regions) and from each other.

[35] All together, these procedures constitute the subject of solar granulometry. For basic principles of granulometry see (Sonka et al. 1999).

the time series of granulation parameters derived from image time series, which is important for the present study.

Spectral methods of image processing deal with the measurement, analysis and interpretation of the Fourier spectrum, which is obtained from an individual image or image series using the Fourier transformation and, in modern digital image processing, the Fast Fourier Transformation (FFT). In astronomic imaging, classical spectral methods involve power spectrum analysis of intensity variations, (auto)correlation function analysis, image filtering, apodization and reconstruction. The Fourier filtering method developed in (Roudier & Muller 1986) was used extensively for granular image segmentation up to the 2000s (Pötzi et al. 2000, Hirzberger 2002). The power spectrum analysis was applied to the overall estimate of the granulation scale, the contrast and the granule-size distribution in (Muller et al. 2007). The frequent need to perform both direct and inverse Fourier transformations makes this group of methods computationally intensive and prone to noise.

Although historically important for image processing, the spectral approach is no longer as popular. There is currently a tendency to reduce the need for work in the spatial-frequency domain. Conventional image domain processing methods are preferred in many cases over spectral processing methods due to the high computing efficiency and the affordability of the technical implementation of the former. The list of image processing tools that are applicable to granulation segmentation in grayscale BFI images is extensive and includes several groups of algorithms that work in the spatial domain, namely thresholding, edge-based segmentation, area-based segmentation, segmentation by matching, morphological segmentation, graph-based segmentation and combined or advanced algorithms (Schrijver et al. 1997, Sonka et al. 1999).

3.2 Edge detection operators

Most of the known image segmentation algorithms working in the space domain involve edge detection operators, which are also referred to as filters. Virtually all edge detectors are differential operators that use gradient magnitude images as input or generate them themselves. The gradient image is then used to estimate the position and orientation of object edges, to select characteristic edge points (markers) and to trace / delineate object boundaries.

In this context an edge is defined as a location in an image where the image intensity function varies rapidly or abruptly. Edges are described mathematically in the form of an image gradient vector which indicates the strength of the image function variation and points in the direction perpendicular to the local edge. Several differential operators, including local gradient (∇), Laplacian (∇^2), Laplacian of Gaussian (LoG), and others, for converting input images to gradient magnitude images are described as follows.

The magnitude of the intensity gradient at any point in a grayscale image is defined as

$$\nabla[f(x,y)] = \sqrt{\left(\frac{\partial f}{\partial x}\right)^2 + \left(\frac{\partial f}{\partial y}\right)^2} = \sqrt{\nabla_x^2 + \nabla_y^2} \cong |\nabla_x| + |\nabla_y|, \quad (18)$$

where *f(x,y)* is a two-dimensional image function; *x* and *y* denote image coordinates. The replacement of the square root in the gradient operator with the sum of the absolute values of the x and y components of the intensity gradient improves computational efficiency of the

procedure. The gradient magnitude determined by Eq. (18) is often used as a segmentation function. In granulometry, the gradient values are typically high at the object edges and low within the objects.

The partial derivatives of the image function in x and in y direction are well approximated by finite differences, and the magnitude of the intensity gradient is given in the form of central difference as (Sharov 2002)

$$\nabla[f(x,y)] \cong \left(f_{x+1,y} + f_{x,y+1}\right) - 2f_{x,y} \,. \tag{19}$$

In practice, the image derivatives are estimated by subtracting an original image from a translated version of the same image. The values of image translation in both x and y-directions are equal 1 pixel usually, but, in general, can be manipulated separately within the interval from 0 to several pixels. Larger shift values assist in neglecting unimportant changes in the image function. Further increase in the shift value coarsens the spatial resolution of the resultant gradient image (Sharov & Gutjahr 2002).

The direction of the gradient β is given by the relation

$$\beta(x,y) = tan^{-1}\left[\left(\frac{\partial f}{\partial x}\right)/\left(\frac{\partial f}{\partial y}\right)\right] = tan^{-1}\left(\nabla_x/\nabla_y\right), \partial f/\partial y \neq 0 \,, \tag{20}$$

where the angle β is measured with respect to the x axis (Gonzales & Woods 1993).

The non-directional second-order derivative of a two-dimensional image function *f(x,y)*,

$$\nabla^2 f(x,y) = \left(\frac{\partial^2 f}{\partial x^2}\right) + \left(\frac{\partial^2 f}{\partial y^2}\right), \tag{21}$$

is known as the Laplace operator. The average value of the Laplacian is 0 at the transition of the object edge[36]. In contrast to the gradient operator described with Eqs. (19, 20), the Laplace operator only determines the gradient magnitude.

The discrete approximation of the Laplacian operator is specified as

$$\nabla^2 f(x,y) \cong \left(f_{x+1,y} + f_{x-1,y}\right) + \left(f_{x,y+1} + f_{x,y-1}\right) - 4f_{x,y} \,. \tag{22}$$

Technical realization of Eq. (19) is fulfilled by copying the input image, shifting the copy by 1 pixel in x or y-direction and summing or subtracting the shifted version of the copy with/from the original image. Image differentiation accentuates high frequencies and amplifies noise. It is therefore advisable to smooth the original image with a low-pass filter prior to computing the gradient (Szelisky 2011). The Gaussian filter is often used to supress high-frequency noise and smooth input images before applying gradient operators.

The combination of the Laplacian operator with the Gaussian filter in the form

$$\nabla^2 G(x,y) = \left(\frac{x^2+y^2}{\sigma^4} - \frac{2}{\sigma^2}\right) \cdot G(x,y), \tag{23}$$

[36] This effect is referred to as zero-crossing.

where $$G(x,y) = \frac{1}{2\pi\sigma^2} e^{-\frac{x^2+y^2}{2\sigma^2}} \quad (24)$$

is the Gaussian smoothing filter, *(x, y)* are the image coordinates and *σ* is a standard deviation of the associated probability distribution, is called Laplacian of Gaussian operator (LoG), which is often used for edge detection in grayscale images. The standard deviation of image intensity *σ* is the only parameter of the LoG filter. The LoG operator is noise-resistant and creates thinner contours than the gradient operator.

Nevertheless, the implementation of LoG involving the second-order calculus is computationally intensive (Lemmerer 2010). Besides, the LoG filter is rotationally invariant, i.e. insensitive to edge directions, and marks the boundaries of sharp corners typical for the form of solar granules rather imprecisely. Particularly poor performance is shown at trihedral and greater vertices, where LoG creates curious loops instead of singular lines (Forsyth & Ponce 2003). This effect can be mitigated with the contour marking process that was realized in the marker-controlled watershed algorithm for grayscale image segmentation.

3.3 Watershed algorithm

Among others, the watershed algorithm devised in (Meyer & Beucher 1990) is one of the most efficient and accurate procedures for the automatic segmentation of long-term image time series of solar granulation. This advanced algorithm combines the principles of thresholding, gradient-based edge detection, active contouring, region splitting and growing, and morphological segmentation. The original watershed algorithm is based on the fast watershed transform (FWT) introduced by (Meyer 1994). The Meyer's watershed algorithm has been continuously improved over the past two decades and the FWT has been replaced with the oriented watershed transform in (Arbeláez et al. 2010). The oriented watershed transform or, simply, watershed transform (WT) is implemented in the Matlab Image Processing Toolbox.

The watershed transform finds "valleys" and "ridges" in a grayscale image by treating it as a topographic surface where light pixels represent high elevations and dark pixels represent low elevations. This corresponds to the appearance of solar granules and intergranular lanes in the BFI blue continuum images. Hence, it is easy to grasp the operation principle of WT and to interpret the results of its application. The watershed algorithm operates with gradient images that are derived from original grayscale scenes using the Sobel operator.

The Sobel operator is a simple approximation to a directional or oriented gradient filter, which is defined as (see Hanslmeier et al. 2008)

$$G_{x,y} = |G_x| + |G_y|, \quad (25)$$

where the components G_x and G_y are given by

$$G_x = \left(f_{x+1,y+1} + 2f_{x+1,y} + f_{x+1,y-1}\right) - \left(f_{x-1,y+1} + 2f_{x-1,y} + f_{x-1,y-1}\right), \quad (26)$$

$$G_y = \left(f_{x-1,y-1} + 2f_{x,y-1} + f_{x+1,y-1}\right) - \left(f_{x-1,y+1} + 2f_{x,y+1} + f_{x+1,y+1}\right). \quad (27)$$

In contrast to the Laplacian of Gaussian edge detector, which marks the boundaries of angular granules very inexactly, all the contours derived with the Sobel operator from the blue continuum images of solar granulation are consistent in their orientation. An important

advantage of the Sobel operator is that it produces strong edges in grayscale images of angular granules in a short amount of time (Fig. 14). It does not require the selection of a spatial scale parameter σ and does not need a priori knowledge about the image intensity distribution function. The Sobel operator is not tuneable, however[37].

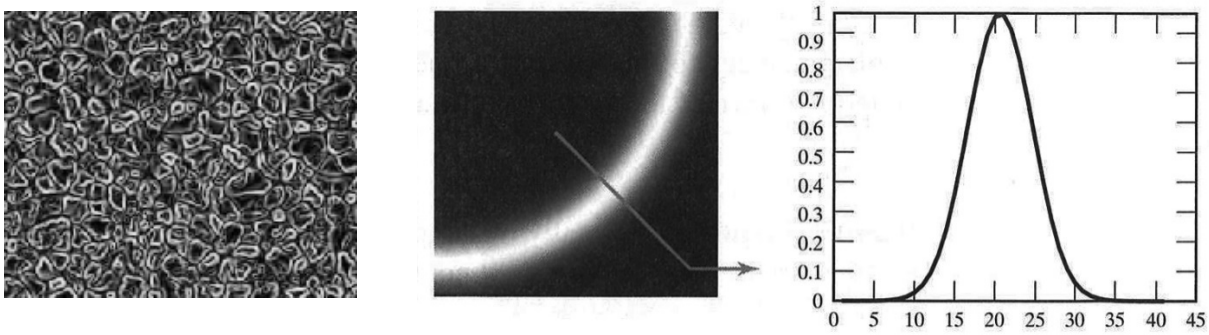

Figure 14. Gradient magnitude image derived from FG20100802 with Sobel filter (left); trail of large gradient magnitude and appropriate cutting direction (centre); peak gradient magnitude (right, adopted from Forsyth & Ponce 2003).

For the gradient-based edge detection one have to identify image points where the value of the gradient magnitude is maximal in the direction perpendicular to the edge and also large; these points are edge points (Fig. 14).[38] The direction perpendicular to the edge is estimated using the gradient direction β given in Eq. (20).

Usually, the watershed transformation is carried out on a smoothed version of the gradient magnitude image in order to reduce the local influence of noise and avoid over-segmentation. In contrast to other segmentation algorithms, however, the smoothing procedure is applied to the gradient size image and not to the original image. Instead of Gaussian filter, an improved version of the watershed segmentation uses a combination of local morphological operations (dilation, erosion, opening, closing[39]) to smooth gradient images and to optimize the boundaries separating the regions (Szeliski 2011).

The resultant gradient image is called the morphological gradient *MG(x,y)*, which is defined as the algebraic difference between the elementary dilation and erosion of the input image *I(x,y)* (Sonka et al. 1999) and is given by

$$MG(x,y) = I(x,y) \oplus SE(x,y;r,n) - I(x,y) \ominus SE(x,y;r,n), \qquad (28)$$

where *I(x,y)* is the input image function and *SE(x,y; r,n)* is the morphological structuring element, while symbols $\oplus$ and $\ominus$ denote the morphological operations of dilation and erosion respectively. The Eq. (28) means practically that the morphological gradient *MG(x,y)* is

[37] The size of the filter mask (kernel) can be selected between 3x3, 5x5 and 7x7 pixels.

[38] The middle and the right part of Figure 11 are taken from (Forsyth & Ponce 2003).

[39] Dilation and erosion are morphological, non-invertible operations; their combination constitutes operations of opening and closing (Sonka et al. 1999).

computed as the difference between the maximum and the minimum grey levels inside the structuring element of finite size placed subsequently at each point of the input image.

In practice, according to Eq. (28), the morphological gradient is calculated as the difference between the maximum and minimum grayscale values within the structuring element of finite size, which is sequentially centred at every point of the input image. The non-negative parameters *r* and *n* of the morphological structuring element denote respectively the radius and the number of line structuring elements that are used to approximate the shape of each object in the input image. The shape of SE can be specified as a cross, square, diamond, disc, octagon etc. The minimum size of the morphological structuring element is 2 x 2 pixels.

The parameters *r* and *n* are tuned to adjust the structural properties of the smoothed gradient image. Usually the number *n* is fixed to 0, 4 or 8 directions. In the case of *n* = 6, the image structure is approximated with a hexagonal pattern, which is practical for the granulometric analysis. The morphological smoothing acts as a low-pass filter and in order to be able to segment the smallest granules it is prudent to keep the *r* - value small. This should be taken into account, since the relation between structuring parameters is given as

$$n < r \, . \tag{29}$$

The total number of granules segmented in the standard BFI image decreases with increasing r. By using an isotropic SE, the dependence on the direction of the edge is eliminated.

The photometric homogeneity of separate regions and the character of object boundaries in the smoothed gradient image depend on the type and sequence of the morphological operations applied to smoothing. In the watershed segmentation, an opening operation, i.e. erosion followed by dilation, is usually followed by closing operation, i.e. dilation followed by erosion. Notice that basic morphological procedures of erosion and dilation are not mutually invertible operations and the results of image smoothing can be varied by changing an arrangement of these operations. In special cases of granulometric analysis, the morphological procedure of opening-closing by reconstruction can be applied to smooth granules and remove dark spots therein without affecting the overall shape of the granules. The quality of the smoothed gradient image is decisive for the automatic segmentation, identification and delineation of granules and determines the results of the analysis.

When the smoothed gradient image is created properly, the watershed segmentation can be started. In the present work, the granulometric analysis of BFI grayscale images is performed using an improved version of the oriented watershed algorithm, which is called marker-controlled watershed (MCW) segmentation. This type of segmentation is done in four steps. In the first two steps, a series of markers for each object (granule) and the background (lanes) are automatically recognized in the smoothed gradient image. In the next two steps, the gradient image is modified and the watershed network is constructed using the watershed transformation of the modified image. In (Beucher 2000) the algorithm for the marker-controlled watershed segmentation is described as follows.

1. Compute foreground markers, that is, determine the position and the pixel value of the brightest pixels or regional flat maxima[40] within each object in the smoothed gradient image. The number of foreground markers is equal to the number of objects in question.

[40] Connected set of the brightest pixels inside the object (granule). These are also called object markers.

2. Compute background markers, i.e. identify pixels, where the value of the gradient magnitude is minimal or zero, that are not part of any object.[41]
3. Modify the smoothed gradient image so that only the most significant contours between the foreground and background markers are retained.
4. Compute the watershed transform of the modified gradient image and define the position of the watershed points and configuration of the ridge separating basins in question.

Depending on the application, the identification of markers and modification of the morphological gradient image can include distance transform[42], geodesic skeleton and dilation, and image inversion operations. The diagram that shows the data and workflow of the MCW algorithm used in this work is shown in Fig. 15, left. Flowchart elements that indicate image-based products (input, intermediate and output) are shaded in cyan. A simplified explanation of the functional principle of the MCW algorithm based on the immersion analogy can be seen in Fig. 15 on the right (Arganda-Carreras 2019) wherein blue vertical lines indicate watersheds.

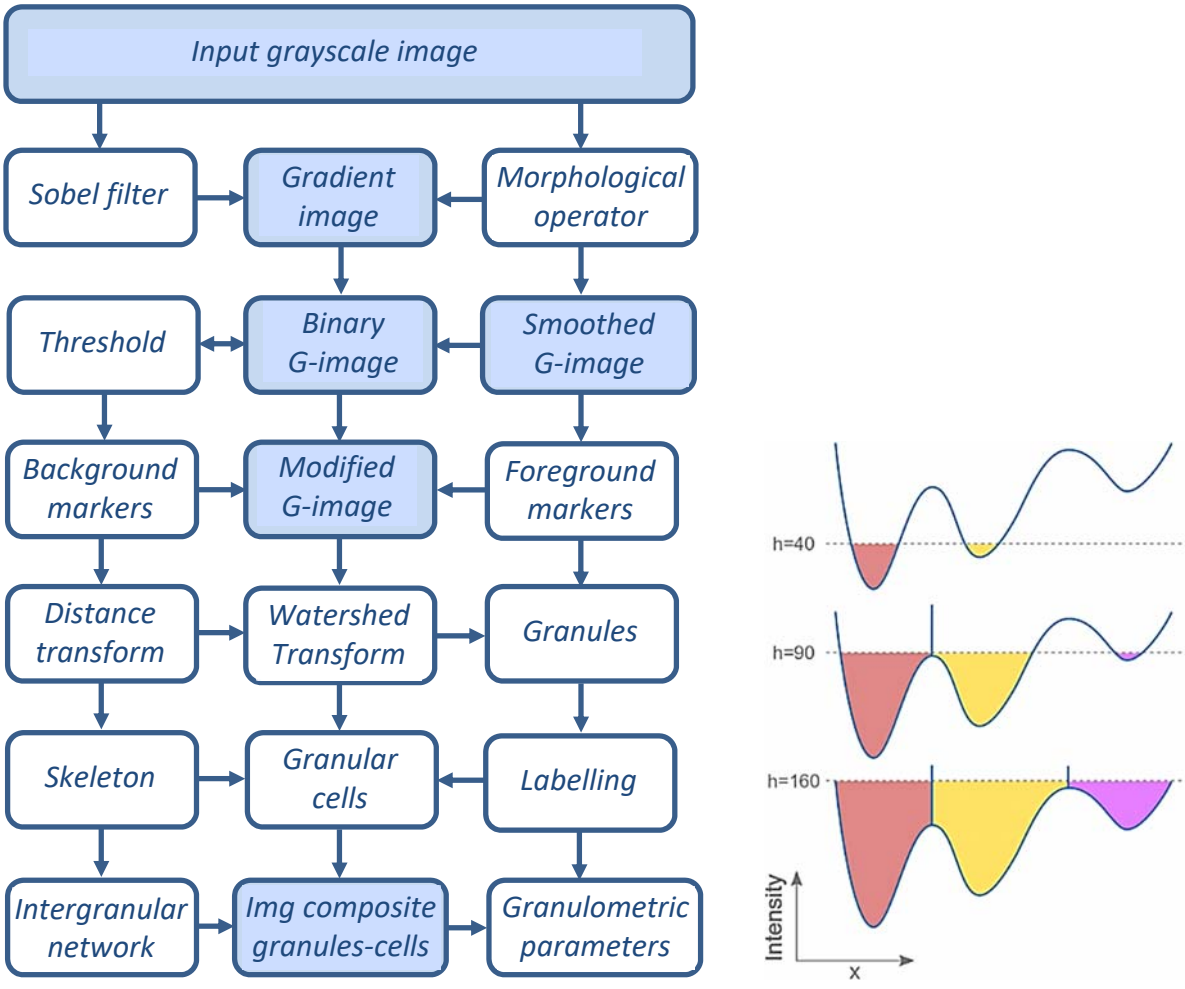

Figure 15. Flowchart (left) and operation principle (right, © ImageJ) of the marker-controlled watershed algorithm

[41] These are placed in intergranular lanes between the granules.

[42] The distance transform labels each pixel of the image with the distance to the nearest boundary pixel.

The main criterion of the watershed segmentation is the homogeneity of the grey values of the objects present on the image. Morphological operations of opening and closing create flat extremes of the gradient image in each object that can be used as foreground markers. In the MCW algorithm, both foreground and background markers are set automatically to the local minima of the image gradient, yet without outlining the object boundaries. The objects are delineated in a separate operation using the heuristic threshold and the segmentation function converted into a binary image (Fig. 16)[43]. Object markers are not necessarily placed in the central part of the object.

After the objects have been marked, they can be grown from the markers, provided that the parts of the objects are not connected when they come close to each other. In the area where the growing objects meet each other, the watershed is built in the form of a dam that separates catchment areas, each of which contains only one minimum (Fig. 15, right). The final contour search is performed on the modified gradient image using the morphology-based watershed transformation, which includes the distance transform and geodesic skeleton operations. Both, the distance transform and the skeleton operation are applied to the binary image.

In the distance transform of the modified gradient image, the value of each pixel is replaced by its distance to the nearest background pixel. The morphological operation of skeleton represents watersheds in the form of a thin line that runs along the medial axis of the original shape. The minimum width of the watershed lines (intergranular lanes) that separate neighbouring granular cells is made equal to 1 pixel. Each segmented object gets certain individual label, e.g. certain number or/and colour.

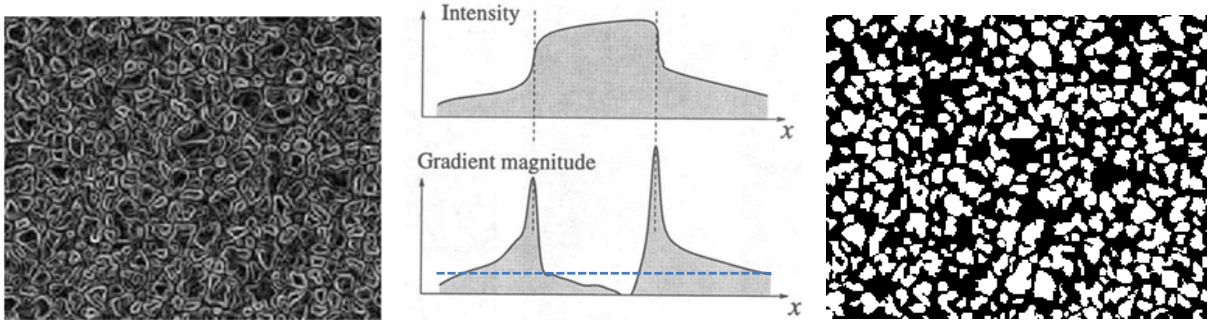

Figure 16. Gradient magnitude image (left), threshold, and object mask of FG20061224 (right)

The MCV algorithm supports region-based rather than boundary-based segmentation and looks for similarities between pixels and regions (Beucher 2000). As a result, the morphology-based watershed transform finds smooth regions called basins that are separated by higher gradient boundaries called watersheds or “ridges”. The output product is presented in the form of an image composite that contains the watershed lines and / or object edges that are superimposed on the original grayscale image for visual control. No supervision and no a priori knowledge on the original image quality are needed to perform the WT. In contrast to other dedicated algorithms for image segmentation, e.g. the multiple-level tracking (MLT) algorithm, the watershed algorithm is not recursive.

[43] In Figure 13, the right and left images are fragments of FG20100802; the middle graph is adopted from (Sonka 1999). The binary image of segmented objects is often referred to as mask.

The MCW algorithm is independent of object shape and size and works well also in the case of uneven spatial distribution of the image brightness. It is efficient and accurate, and it produces continuously closed contours. In the resulted image composite all intergranular minima are interconnected as well. To better account for small objects and partially filled pixels it would be expedient to use the watersheds represented in a vector form. However, vector graphics involve considerable computational effort, and the raster-based version of the MCW algorithm is used for this work.

3.4 MCW algorithm implementation

The MCW algorithm is potentially well-suited for identifying, delineating and labelling both granules and granular cells in grayscale BFI images. It ensures certain technical advantages in terms of accuracy and computational efficiency compared to other segmentation algorithms. It is therefore worth using this algorithm for the automatic segmentation of solar granulation in the long Hinode BFI image sequences recorded in the blue continuum window. The technical implementation of the MCW algorithm must be adapted to the accuracy and efficiency requirements of the granulometric analysis and be suitable for the ubiquitous measurement of granular size and contrast.

In the present work, the MCW algorithm was adapted for the automatic segmentation and morphometric measurements of solar granulation in 8-bit Hinode BFI images and programmatically implemented using the student version of the MATLAB software package v.2017b. The main reason for using this software is that I am sufficiently familiar with the MATLAB computer environment and have acquired good programming skills in MATLAB during my studies at Graz University of Technology. Seven days a week I had constant access to a student computer with MATLAB installed. An important factor when choosing this software package for programming the MCW algorithm is that the oriented watershed transform (WT) is already implemented in the Matlab Image Processing Toolbox. There are also a number of working MCW implementations written in MATLAB that are aimed at solving “terrestrial” tasks.

These implementations are well documented, which helped me to write, test and edit my own MATLAB program for the solar granulation image segmentation (SOGIS). In this section I’ll explain the main processing steps of the SOGIS program in detail, illustrate them with the image processing results and describe some tests that would validate the solution. The entire SOGIS code is given in the Annex A to this thesis (pages 93 through 100). The SOGIS software consists of six modules, including

- block for data preparation and input,
- block for image segmentation,
- block for morphometric measurements and granulometric analysis,
- block for correlation analysis and statistical processing of results,
- block for validation and correction procedures and
- block for graphic representation.

The SOGIS structure scheme is shown in Figure 17. In the following, the detailed description of each SOGIS block is given with the main emphasis on the redesigned parts of the software.

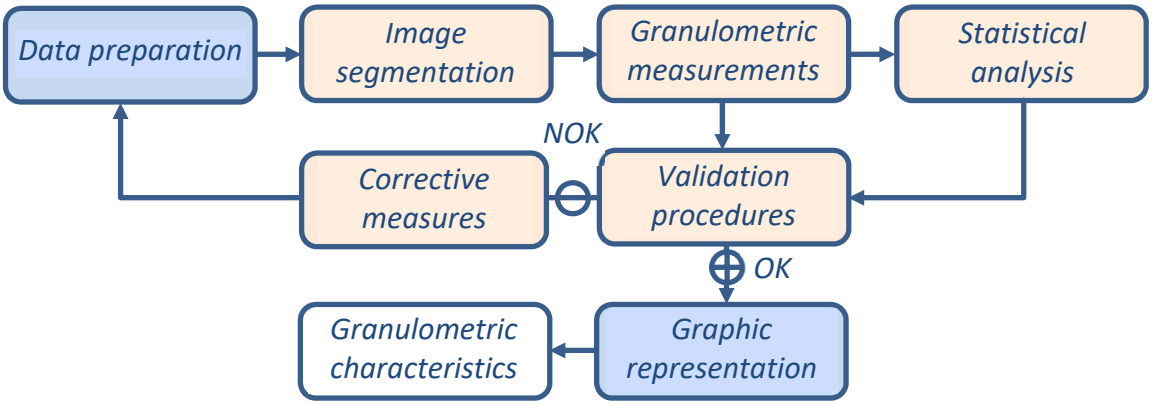

Figure 17. SOGIS software architecture

Data preparation

The SOGIS block for data preparation and input ensures processing of image stacks and includes procedures for

- reading Hinode image sequences given in FITS format and converting them into 8-bit grayscale images in TIFF format,
- storing and reading corrected image data,
- reading SSN *.txt data, both daily and monthly mean,
- modifying SSN data time series to match HITS time series, e.g. imitation of data gaps,
- reading ancillary data for validation procedures and corrective measures.

In addition, this block contains options for changing image frames / size, for creating image sub-sequences and for directly addressing individual pictures with the specified file name or sequence number.

Image segmentation

The module for image segmentation includes interconnected means for

- generation of gradient magnitude images *G(x,y)* from input grayscale images with adjustable Sobel operator,
- creation of morphological gradient images *MG(x,y)* using morphological operations of erosion-dilation, opening-closing and opening-closing by reconstruction with adjustable size and shape of structuring elements,
- detection of back- and foreground markers and removal of markers with less than 5 pixels,
- modification of gradient G-images involving smoothing, adaptive thresholding and de-spiking,
- converting grayscale G-images to binary images by replacing all pixels in the input image with magnitude greater than threshold with the value 1 and replacing all other pixels with the value 0,
- granule edge detection (optional) using Canny filter,
- removal of cut-by-frame granules,

- computation of the distance transform of the binary (mask) image,
- computing watershed transformation of the distance transform; watershed lines are placed where the watershed transform of the distance transform becomes 0,
- photometric inversion of the binary watershed image,
- visualisation of the segmented image by superimposing the watershed image on top of the original intensity image,
- labelling segmented objects.

In practice, the kernel size of the Sobel and Canny filters was set to 5 x 5 pixels per default while other tuneable parameters such as the size r = 1 pixel and shape n = 0 of the morphological structuring element[44], the minimum marker size M_{min} = 5 pixels and the binarizing threshold value I/I_o = 0.97 were determined empirically.

The threshold of I/I_o = 0.97 was chosen as a trade-off between the desire to keep the mean size of the identified granules close to the generally accepted value of 1 Mm and the requirement to remove the smallest granules with Ag <9 pixels from the analysis as offered in (Hirzberger 2002). No additional operations were involved to improve the original image contrast or sharpness, such as image histogram equalisation, image intensity rescaling, apodization or unsharp masking (high-pass filtering).

The results of data processing using the SOGIS image segmentation engine are shown in Figure 18. This illustration represents the original Hinode BFI image fragment of 800 x 500 pixels with the size of 31.32 x 19.58 Mm or 43 x 27 arcsec in the upper left corner, intermediate results and the resulting segmentation of the original image in the lower right corner. In the resultant composite image, the identified granular cells are bordered with red lines. The linear bar in Fig. 18 indicates the image scale. Both products in the bottom raw of Fig. 18 are applicable to identifying and measuring properties of granular cells, while both panels in the third raw demonstrate segmentation products that can be used to measure the morphometric properties of granules and intergranular lanes.

Figure 18 clearly shows that the watershed segmentation with subsequent metric analysis is a unique process in which almost all image details are relevant for the analysis. The right panel in the second raw of Fig. 18 demonstrates, however, that some fairly dark (overlapped, occluded) granules are not labelled with foreground markers, which means that these objects are not segmented properly in the end result.

This effect results in the appearance of X-crossings in the watershed network, which correspond to the location of the darkest granules. Two such crossings are framed in Figure 19. As a result, the darkest elements of the granulation pattern are "crossed out" from the watershed network, resulting in a smaller number of identified granules. This error is called under-segmentation and remains the main limitation to the accuracy of the MCW algorithm. However, I estimate that the number of "lost" granules does not exceed 0.5-1.0% of the total. The manual setting of markers on dark granules is possible to mitigate under-segmentation, although this takes a lot of time.

[44] Shaping of structuring element does not make any sense if its area is smaller than 4 pixels (r = 1 pixel).

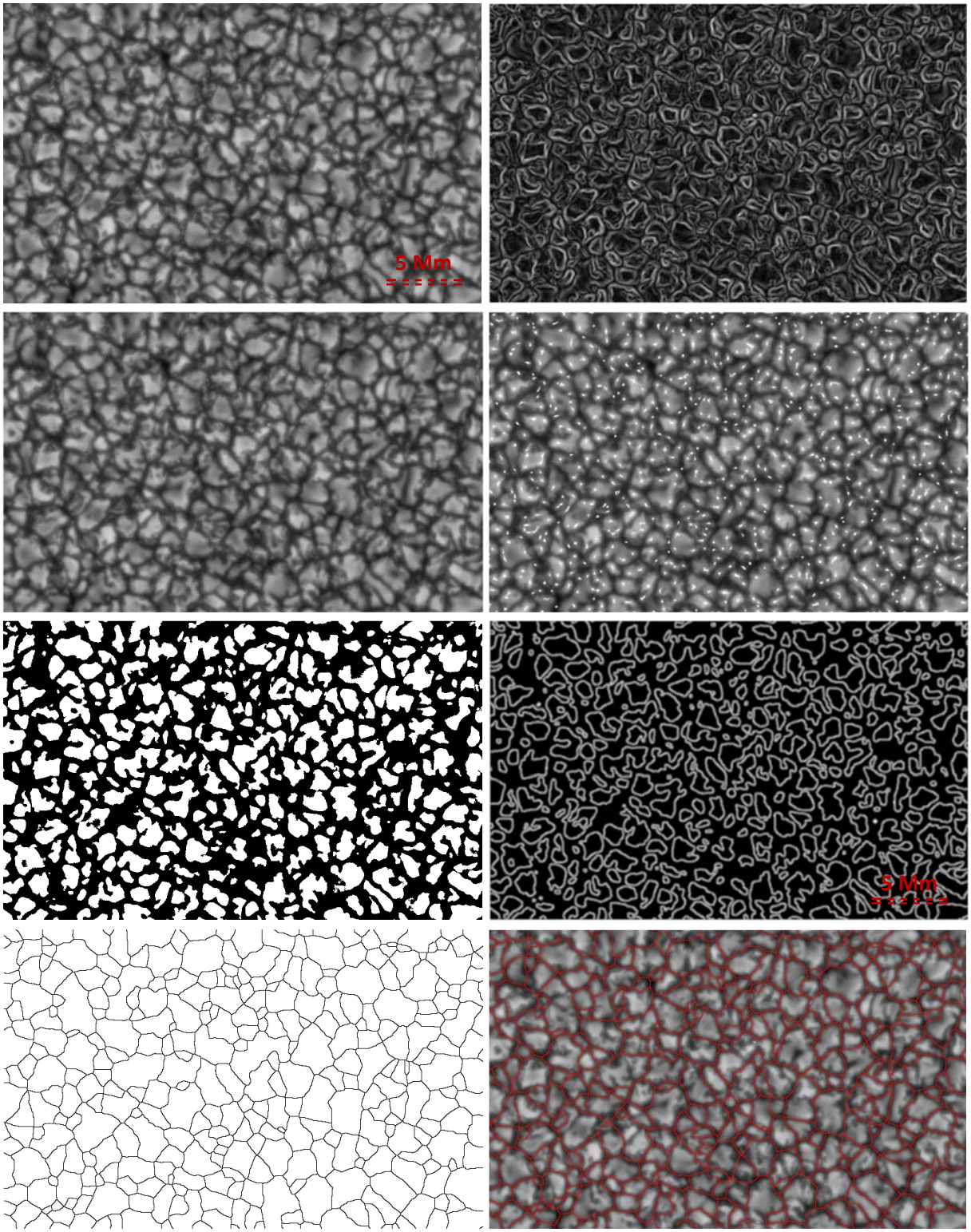

Figure 18. Segmentation of FG20070131_180358 image: Original image fragment of 800 x 500 pixels (top, left), gradient magnitude image (top, right), morphological gradient image after opening-closing by reconstruction, regional maxima overlaid on the original image, object binary mask, granule edge detection with Canny filter, inverted watershed image (bottom left), and the resultant segmentation (bottom right).

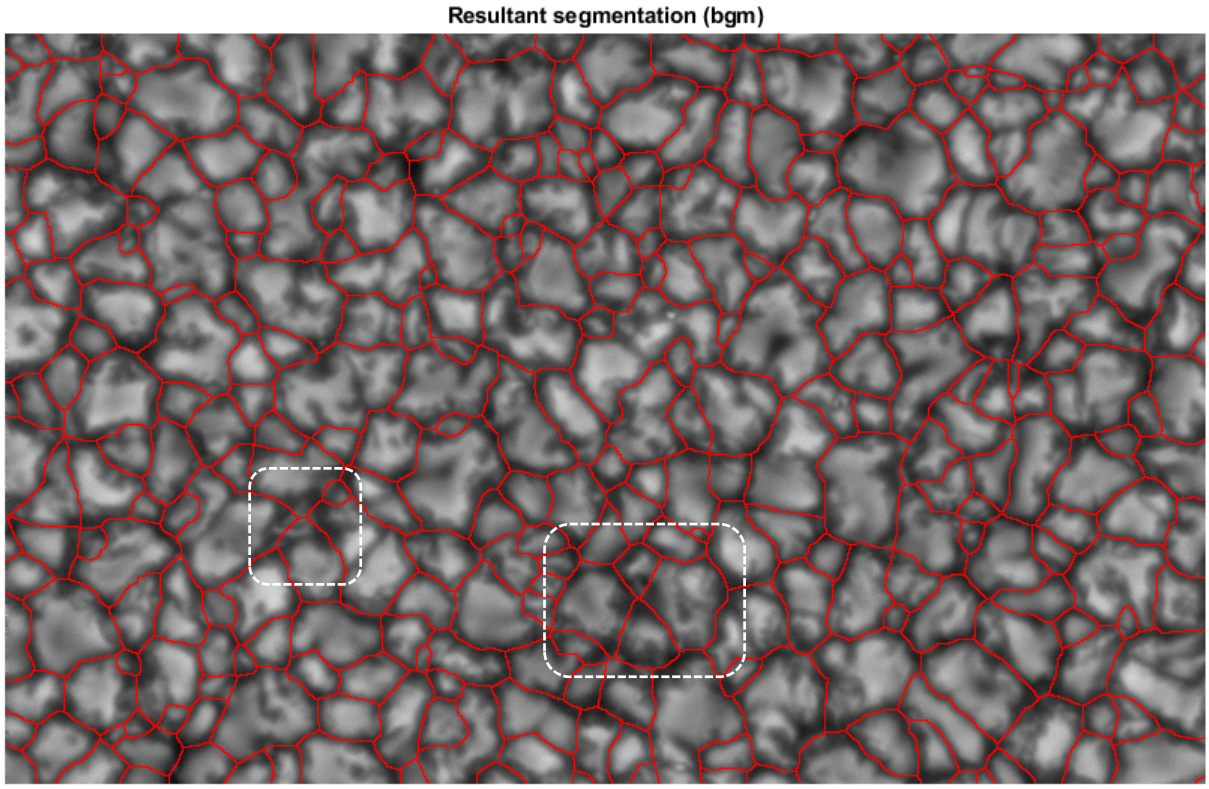

Figure 19. Close-up of the segmented FG20070131 image showing lost granules (framed)

Morphometric measurements

The granulometric module of the SOGIS software is based on the adaptation of the Image Region Analyser App and the 'regionprops' function implemented in the MATLAB software.[45] My module for morphometric measurements includes procedures

- to find, select, and label objects in binary images[46],
- to measure properties of image objects, such as area, perimeter, perimeter-to-area ratio, centre of mass, orientation, and bounding box,
- to remove small objects from binary image,
- to measure properties of grayscale image areas corresponding to identified objects, e.g. to create image histogram,
- to measure the properties of individual pixels and paths, e.g. to create contour plot of image data, to determine pixel value cross-sections along line segments (intensity profiles) and to measure distances between pixels / objects.

With this module I was able to efficiently measure the area, the perimeter, the ratio of perimeter to area (PAR), the equivalent diameter and the extent of each granule frame by frame. In this concern, the equivalent diameter D_e of the granules with an irregular shape was determined as the diameter of a circle with the same area as the granules in question (Muller & Roudier 1986), i.e.

[45] https://www.mathworks.com/help/images/pixel-values-and-image-statistics.html (accessed in 2019).

[46] An object (granule) in a binary image is a set of connected pixels with the same value.

$$D_e = \sqrt{4A_g/\pi}\,, \tag{30}$$

where A_g is the granular area.

The granular extent was defined as the ratio of the number of pixels in the granule to pixels in the total bounding box, returned as a scalar. It is computed as the granular area A_g divided by the area of the bounding box A_b[47], i.e.

$$E_g = A_g/A_b\,. \tag{31}$$

The area, the perimeter and the equivalent diameter were measured in pixels, with a pixel scale of 0.104 arcseconds or 75 km. In this case, the perimeter-to-area ratio and the granule extent are dimensionless characteristics. Both determine the complexity of the shape of the granules and can be considered invariant for image scaling effects. Under certain conditions, they are less scattered compared to the dimensional parameters such as granular area or circumference. PAR is closely related to the fractal dimension *D*, which is often used to describe the spatial structure of solar granulation (Hirzberger 2002).

In addition to morphometric measurements, I programmed the procedure to determine the granulation contrast as the standard deviation of the grayscale image intensity within the granule, i.e.

$$C_g = C_{std} = \sqrt{\sum_0^N (I_i - I_0)^2/N}\,, \tag{32}$$

where *N* is the number of pixels within a single granule, I_i is the continuum intensity of the current pixel and I_0 is the mean intensity. The same equation can be applied to the contrast estimation of the entire image. In the latter case, the total number of pixels is 2048 x 1024 = 2097152 pixels.

Most astrophysical publications use the root mean square contrast of the granulation images in the form (Abramenko et al. 2012)

$$C_{rms} = \sqrt{\sum_1^N (I_i - I_0)^2/\left(N \cdot {I_0}^2\right)} = \frac{1}{I_0} \cdot \sqrt{\sum_1^N (I_i - I_0)^2/N}\,. \tag{33}$$

To compare the results obtained in this study with those of other investigators, the granular standard contrast must be divided by the value of the average image intensity

$$C_{rms} = C_g/I_0\,. \tag{34}$$

In the case of normalized image,

$$I/I_0 \cong 1 \quad \text{and} \quad C_{rms} \cong C_{std}/I\,. \tag{35}$$

It should be noted that the granulation contrast values vary essentially from image to image depending on the scenery, focussing and the prevailing size of the granules to be identified and measured. Correspondingly, different empirical values of the normalized continuum intensity I/I_0 were reported for the boundary between granules and granular lanes. In

[47] A bounding box is the smallest rectangle that contains the object (granule).

(Abramenko et al. 2012) five different threshold values in the range from 1.03 to 0.97 were specified as applicable to detect granules.

According to the concept of frequency-contrast characteristic, the granular size and the contrast in the given image are inseparable, and the image contrast can only be improved at the expense of the image resolution. In other words, the granulation size and the contrast are closely and inversely related and are not independent. Therefore, the focus in this work was on the investigation of only one group of these parameters, namely the geometric parameters, and the focus was on the morphometric analysis not of granules but of granule cells. As it was mentioned in Chapter 1.3, the identification of a granular cell is more straightforward than that of a granule, especially in images with heterogeneous contrast.

The main output of the morphometric module is a tabular list in which the values of five morphometric parameters and the image contrast for each identified granule and granular cell are specified line by line, page by page. In the list, each identified granular cell is labelled with a unique number and / or colour. The average number of granules identified in a typical Hinode scene is approximately 6400, which determines the total number of 44,800 values[48] that must be defined and stored as a result of the granulometric analysis of a single image.

Given the total amount of Hinode images to be processed as 710 scenes grouped into 7 HITS, we can rate the expected total number of granules identified in all HITS at 4.5 million. Note that by using 24 bits to encode colour information 2^{24} = 16777216 different colours can be displayed. This is sufficient to provide each granule identified in all HITS image time series with a specific colour. Still, the total number of measured parameters exceeds 38 million, which is not very practical for documentation, manual analysis and graphic representation. These big numerical data were processed with the aid of the module for statistical analysis.

Statistical analysis

The module for statistical analysis was used to compute the standard statistics (mean, variance and correlation) of all granulation parameters derived from seven HITS. As a result, the averages for each of the seven parameters[49] were defined for each of the 710 Hinode images. This enabled further granulometric analysis and graphic display, since I only had to deal with 4970 mean values of the granulation parameters.

The statistical module was also used to calculate the cross-correlation between time series of granulation parameters and the SSN time series. Both, cross-correlation coefficients and two-dimensional temporal cross-correlation functions were computed. The latter were used to determine the time delay or lag between discrete-time processes of magnetic and convection activity and to investigate the nature of the causal relationship between these processes. The time delay τ between the pair of random processes $f(t_1)$ and $g(t_2)$ is determined by the argument of the maximum of the cross-correlation, as

$$\tau = argmax\big((f \star g)(t)\big), \tag{36}$$

[48] Including label, five structural parameters and image contrast.

[49] Total number, area, perimeter, PAR, equivalent diameter, extent and contrast of granules.

where symbol ★ denotes the operation of cross-correlation and integer t is an arbitrary point in time.

The delay value determined in this way indicates the point in time at which the granulometric and SSN time series are best aligned and their cross-correlation function reaches a maximum if the signals are positively correlated or a minimum if they are interrelated inversely. The sign of the lag between the time series denotes the leading process, which occurs earlier in time.

Moreover, the statistical module was used to estimate the execution time of my MATLAB code and to optimize the composition and sequence of operations for granulometric analysis. To estimate the execution time for smaller portions of the SOGIS code I used tic and toc markers. The MATLAB ® Profiler was adopted to estimate the performance of the entire SOGIS code and to find out bugs and the slowest operations.

As a result, the SOGIS code started to work and the overall performance of the computing blocks was significantly improved. Within three working months, the SOGIS execution time was reduced six times from 15 seconds to 2.5 seconds per image. Nevertheless, the correctness of the image segmentation and the granulation measurements had to be verified. This was performed using block for verification and correction procedures.

Validation and correction procedures

In the present work, I couldn't get an access to original high-resolution optical images of solar granulation obtained by ground-based telescopes. Therefore, the performance of the MCW algorithm was preliminarily checked using several test images that show apple piles (Fig. 20). Afterwards, quality control, verification and validation of image processing results were carried out regularly using various approaches, including

(1) comparison of the results of granulation measurements obtained from separate Hinode images of different format, size, season and quality (resolution, sharpness and contrast);
(2) comparison of the results of granulation measurements made with the same set of processing procedures, but from different image time series, e.g. HITS-basic and HITS-other;
(3) comparison of the results of granulation measurements obtained from the same data set, but with different processing tools, e.g. with different edge operators (Sobel or Canny), different versions of the processing software (light and full), etc.
(4) comparison of the results of granulation measurements obtained from original and made-up[50] images;
(5) comparison of the results of granulation measurements that were carried out before and after corrective measures with the relevant image data set;
(6) comparison of the results of granulation measurements obtained automatically with the results of manual measurements;
(7) comparison of the results of granulometric measurements obtained in this work with those obtained by other researchers;
(8) animation of the results to identify outliers.

[50] Artificially sharpened images with enhanced contrast.

The final reliability test of the MCW image segmentation method was carried out by thoroughly comparing the results of granulation measurements obtained from the HITS-2011, HITS-2012 and HITS-2015 daily time series.

Figure 20. First images for testing MCW segmentation algorithm

The consistency of composite images representing identified granules and granular cells was checked by differencing between these products and by checking the topological inclusion of each granule in the corresponding granular cell. The resultant product, which resembles Brabant laces and is referred to as inclusion map is shown in Fig. 21.

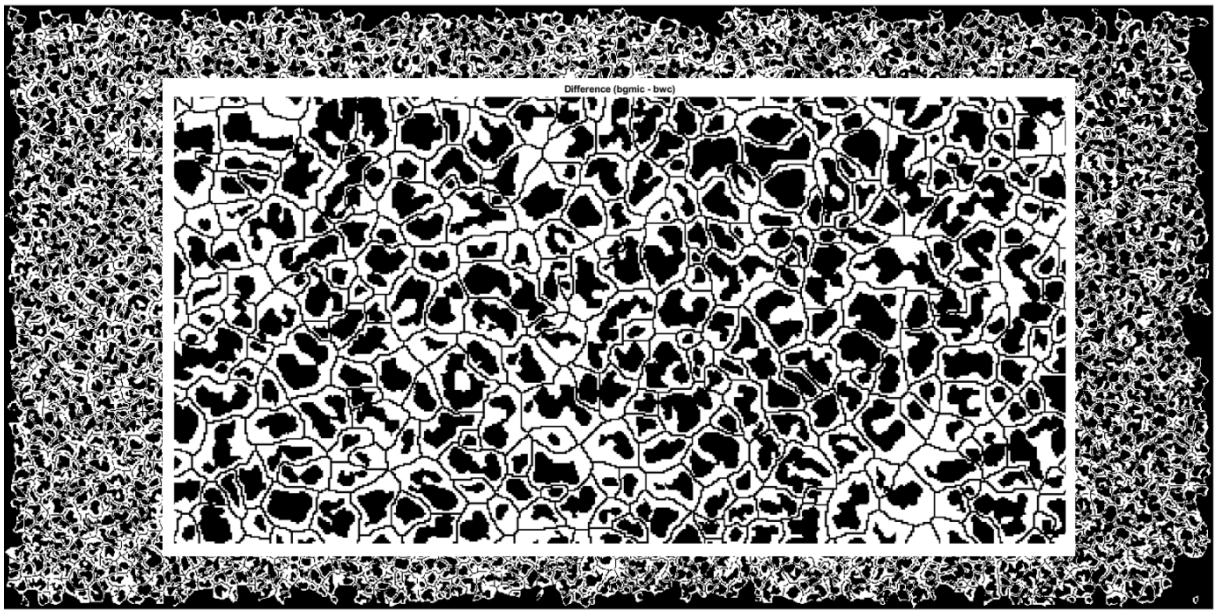

Figure 21. Inclusion map and its close-up as a result of topological control

Almost the same validation procedures as in (1-8), but to a lesser extent, were used to verify the processing of different types of SSN data, including daily, monthly averages, and 13-month smoothed monthly SSN time series. The most important inferences from the correlation analysis of the variability of solar granulation and sunspot activity were validated by comparing

with the results of other investigators and verified in several discussions with experts using visual control and logical methods of physical reasoning.

In the event that the processing results were incorrect (not OK as specified in Fig. 17) or did not meet my expectations, the corrective measures started. Some of corrective measures including

- removal of the image with out-of-control granulation properties and replacement with the closest image in the time series,
- change of the entire HITS,
- software optimisation and finding bugs

were performed manually.

Other routine corrections including

- resampling all Hinode images obtained in the period of 01.12.2006 - 28.01.2008 to the pixel scale of 0.104” with the Lanczos filter (geometric homogenisation),
- correction of granulometric results for the temporal variation of the Sun-Earth distance,
- removal of granules truncated with the image frames (optional),
- removal of granules with A_g < 5 pixels (optional),
- saving results in generally acceptable graphic formats (TIFF for images, PNG for graphs)

were carried out automatically.

Remember that all Hinode images available for this study were previously calibrated with the standard reduction procedure implemented in SolarSoftWare (SSW). This calibration procedure corrects images for bad pixels, readout errors, dark current, flat fielding and stitching (Section 3.1). In order to exclude the influence of cut-by-frame granules on the results of morphometric analysis, in my software, all granules truncated with the image edges can be identified and removed automatically (Figure 22). Of course, this procedure reduces the total number of granules identified in a single Hinode scene and should (optionally) be used with caution.

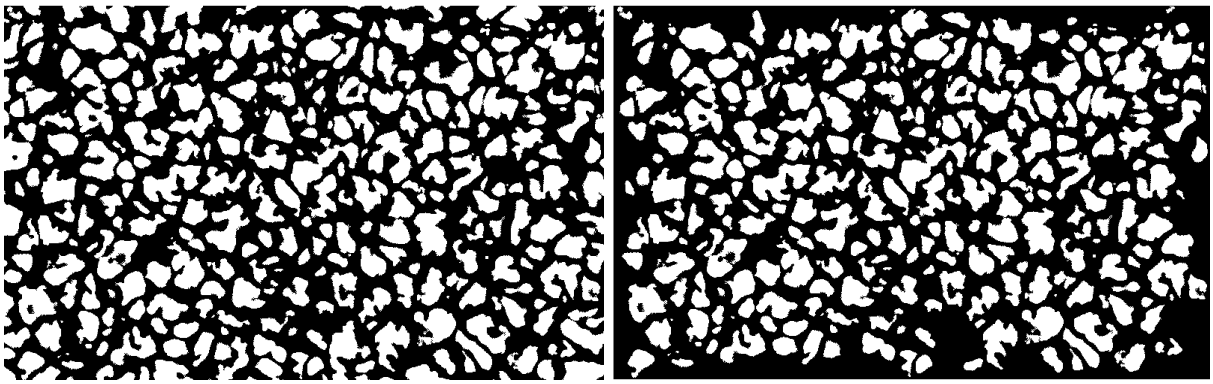

Figure 22. Removal of cut-by-frame granules (right) from the binary FG20070131 image (left)

After corrective measures were taken, the granulometric processing and correlation analysis of HITS and SSN time series were repeated from the beginning. The technical performance of the MCW segmentation method and granulometric processing implemented in the SOGIS software was compared using standard parameters of the workload and execution time with that of the MLT (Multiple Level Tracking) segmentation method described in (Bovelet & Wiehr 2001and implemented in IDL and C++ (Lemmerer 2010).

There are currently no other operational space-based solar telescopes that are comparable to Hinode in terms of image resolution, pointing accuracy and mission duration. The Atmospheric Imaging Assembly (AIA) aboard the Solar Dynamics Observatory launched by NASA in 2010 also takes images of the Sun at 450 nm (10. Channel). However, the AIA angular resolution in this channel is only 2.43 arcsec[51] and the pointing grid of 19.5 arcsec is quite coarse. AIA image data is therefore of little use for the validation of the granulometric results obtained with high-resolution Hinode images. Moreover, my cut-out requests for the AIA data received at the same time interval as the HITS time series were rejected due to the lack of data.

Graphic representation

In the case of positive validation (OK in Fig. 17), the results of the granulometric analysis are sorted and visualized

- in textual and tabular form,
- in the form of line and dot plots, graphs and histograms,
- in the form of image-based products, e.g. value-added image composites (Fig. 19),
- in the form of animations, movies, etc.

so that they are understandable for a wide range of researchers, including the author, and can be used for documentation and further presentation.

An example of the tabular representation of granulation measurements is shown in Figure 23. The graphic representation requires a lot of computing time. Therefore, most of the plotting options have been turned off in routine data processing. In the documentation phase, the results of the image segmentation were only plotted for several typical Hinode images.

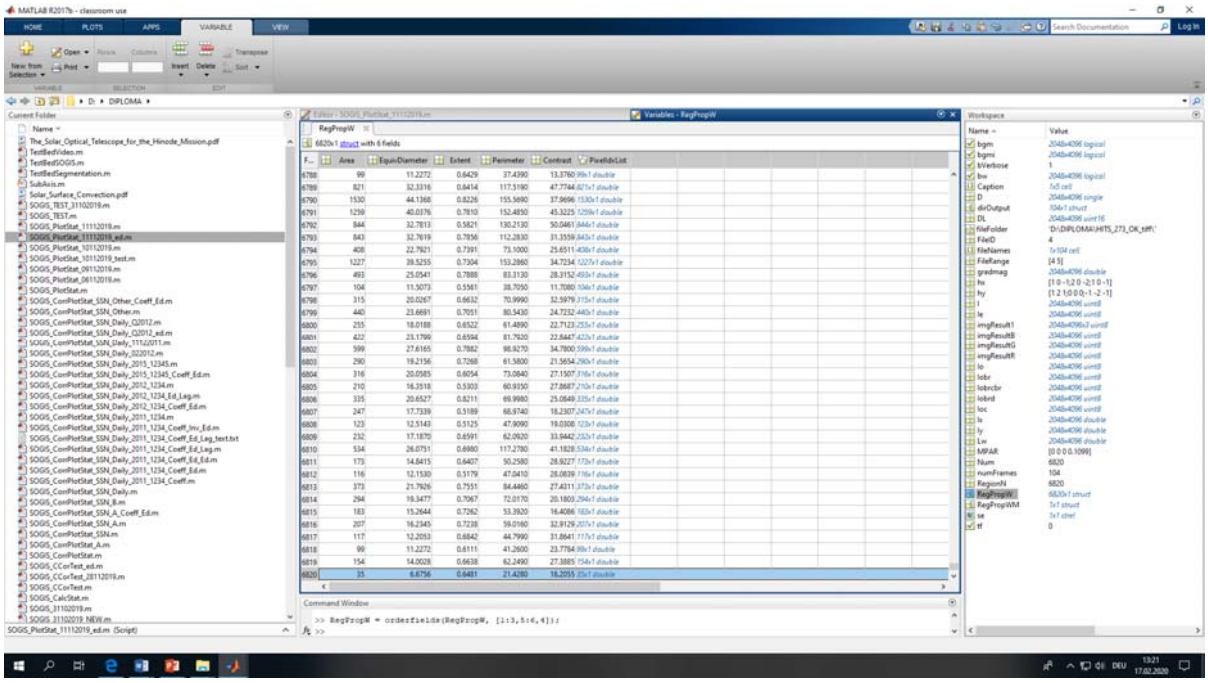

Figure 23. Tabular representation of granular measurements (HITS-273-other)

[51] Angular resolution of AIA images captured in other channels is 1.65 arcsec, which is at least 10 times lower than that of Hinode SOT BFI images.

Chapter 4. Data Processing

This chapter describes the most important procedures and results of data processing in chronological order, i.e. in the same order in which the data time series were processed in practice. The description of granulometric processing begins with the processing of short sequences of Hinode images, as this took less processing time and served a lot to select the relevant image data and optimize the processing chain. Unless otherwise stated, most of the results presented in this chapter refer to granular cells, not granules.

4.1 Processing short sequences of Hinode images

First, separate Hinode images with different sizes and pixel scales were processed in order to estimate the influence of these imaging properties on the results of the granulometric analysis. It has already been mentioned that the original Hinode data set contains images with two different sizes and pixel scales, either 4096 x 2048 pixels with a pixel scale of 0.054" (first 1121 scenes) or 2048 x 1024 pixels with a pixel scale of 0.108" (next 2277 scenes). I refer to these parts as subset A or subset B.

Expressed in pixels, the size of the granular cells measured in subset A and subset B is very different. However, the actual size of the granular cells in [Mm] or [km] must be similar regardless of the source image. The very first graphical representation of granulation measurements made in two Hinode images belonging to subset A (FG20080125) and subset B (FG20080221) is shown in Figure 24. Both images were taken under similar conditions of minimal solar activity (SSN_A = 0 and SSN_B = 11) from the optimal section of the Hinode orbit with a time interval of 27 days. Both are characterized by good sharpness and contrast. Note that these two Hinode images have not been corrected for the variable Sun-Earth distance and truncated granules.

Figure 24 represents the spatial variability of the equivalent diameter of granular cells identified in FG20080125 (top) and FG20080221 (mid and bottom). Both the line-wise (top and mid) and the point-wise (bottom) representation of the equivalent diameter values are displayed. Obviously the granular size in [pix] in picture A is almost twice that in picture B. The total number of cells for images A and B was given as 6433 and 5594, respectively. The average equivalent diameter of granular cells in the A scene with 0.054" angular resolution was estimated at 36 pixels = 1.96 arcsec or 1406 km, while it was measured as 19 pixels = 2.05 arcsec or 1486 km in the B scene with the pixel scale of 0.108".

The area and the equivalent diameter of the granular cell are related as given in Eq. (30). The mean area of granular cells in subset A is approximately four times the area in subset B. Then the fractional area of the granular cells in image A makes up 94% of the field of view (8388608 pixels) and that in image B makes up 88% of the 2097152 pixels. The total length of intergranular lanes with the width of 1 pixel varies between $2D_e$ and πD_e depending on the shape of granular cells. Accordingly, the total number of pixels filling granular lanes in the scene A is 2 x 36 x 6433 = 463176 or 6%, while that in the scene B is about 12%.

Some morphometric parameters of granular cells measured in these two Hinode scenes are specified in Table 2. From this it can be determined that the average scale of a granular cell in both, A and B scenes is 2 arcseconds.

Table 2. Morphometric parameters of granular cells in several Hinode scenes of different size

Subset	Scene size, pixels	Pixel scale, arcsec	Average area, pix	Average equivalent diameter, D_e	Number of cells
A	4096 x 2048	0.054	1222	36 pix = 1.94“ = 1406 km	6433
B	2048 x 1024	0.108	328	19 pix = 2.05“ = 1486 km	5594

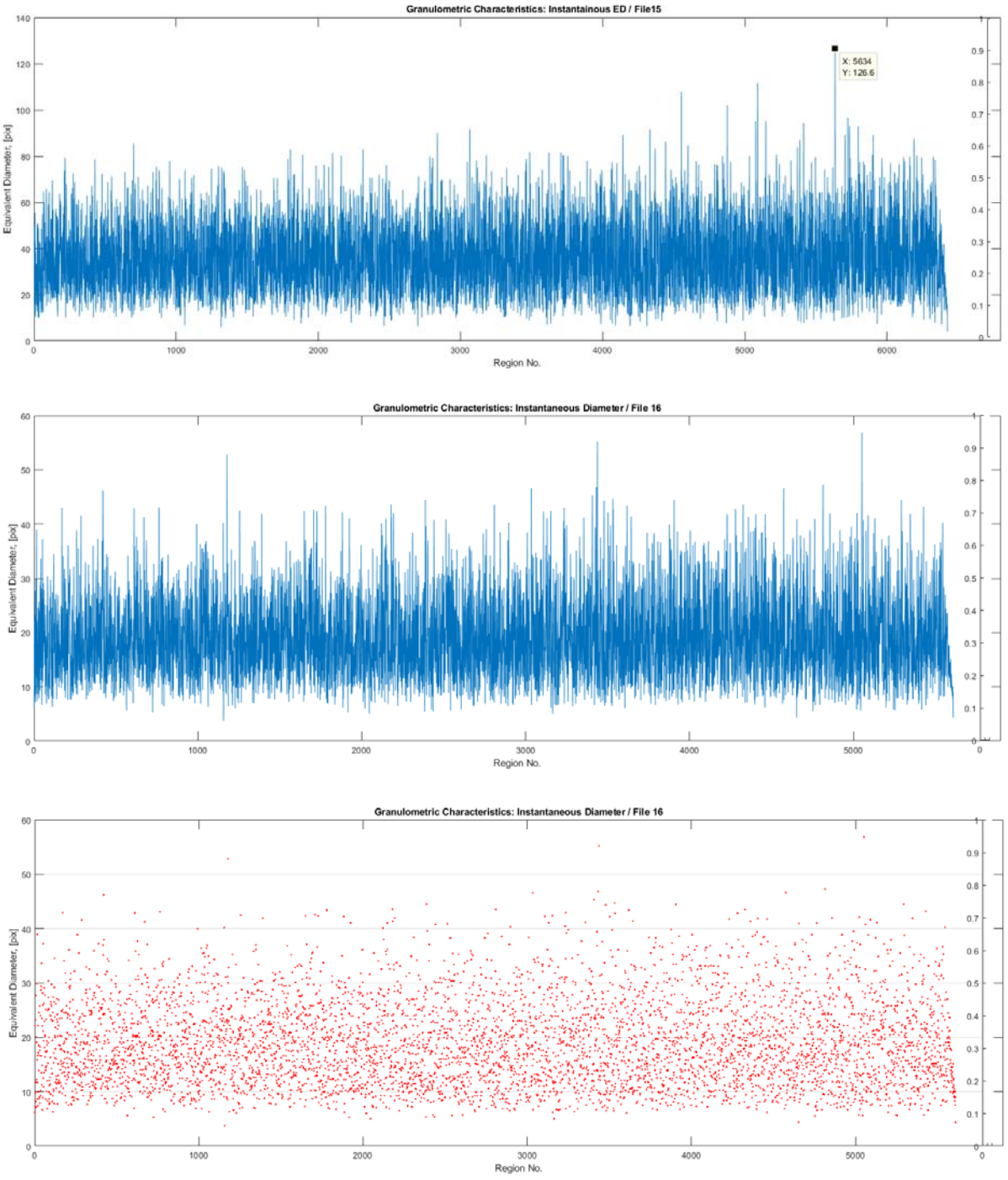

Figure 24. Instantaneous equivalent diameter of the granular cells in scene A: FG20080125 (top) and scene B: FG20080221 (mid and bottom)

The chain-like or cloud-like graphical representation of granulometric values, as shown in Figure 24, is bulky and not very practical for the visual interpretation because there are too many measurement points. In the following, mean values for each granulation parameter averaged over the entire image are calculated and displayed.

The values of mean area and mean equivalent diameter of granular cells derived from the original HITS-273* time series[52] including 15 A-scenes and 58 B-scenes are shown in Figure 25. The temporal behaviour of the mean area in Fig. 25, left is almost the same as that of the mean equivalent diameter (Fig. 25, right). This should be, since these parameters are directly related, as in Eq. (30).

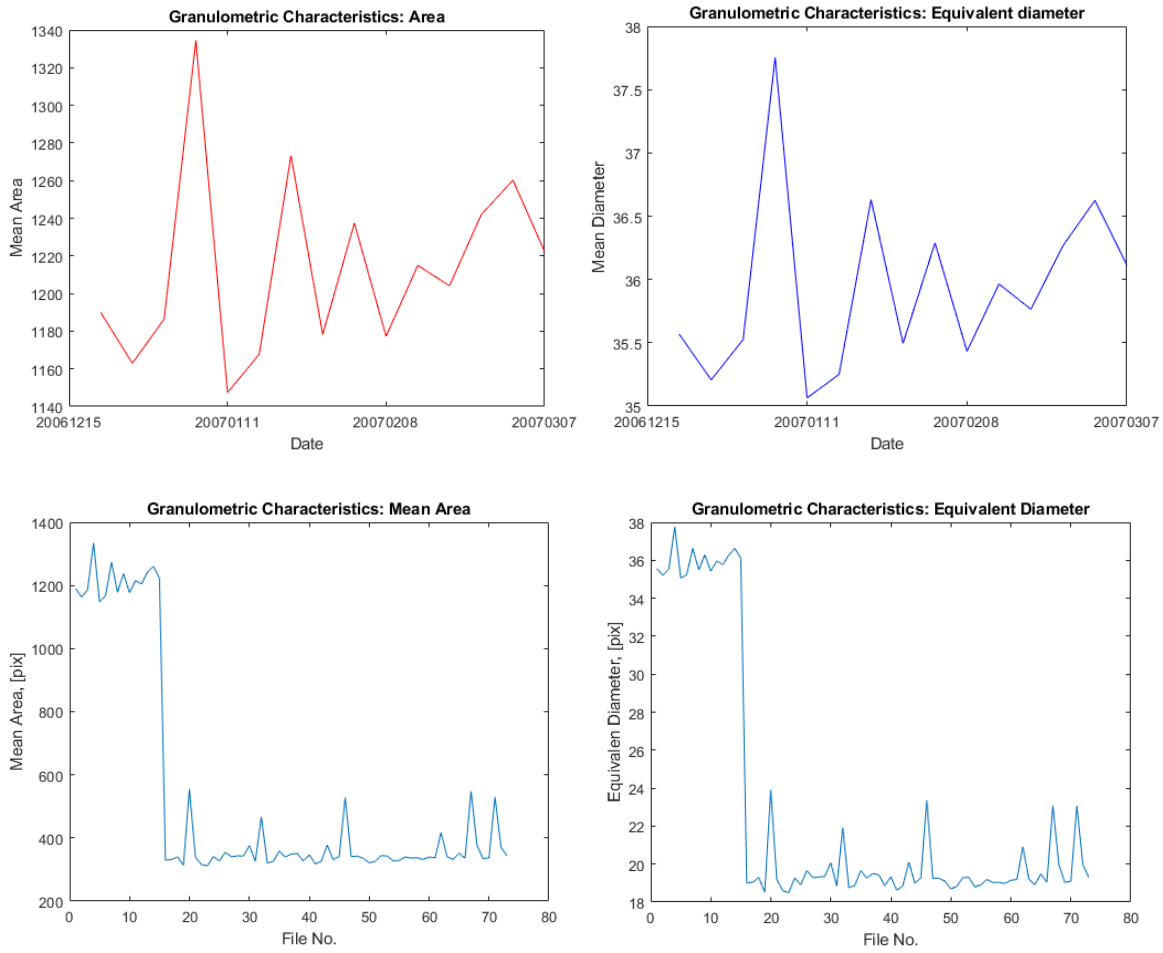

Figure 25. Average area (left) and equivalent diameter (right) measured in the first 73 scenes (lower raw) and the close-up for the first 15 scenes (upper raw) of the HITS-273* time series

A closer look at the graphs in Figure 25 shows a good match with the values given in Table 2. However, there are several artefacts seen in these graphs (Figure 25, lower raw), including 6 -7 spikes due to the presence of slightly blurred images and the steep descent in the graph amplitude between the last A scene and the first B scene, caused by a change in the image scale. This shows the need for a geometric equalisation of all images contained in time series.

[52] These image sequences were not corrected for the variable Sun-Earth distance and the different angular resolutions of the scenes they contain, and include blurry images.

The image scale difference between subset A and B can be taken into account by multiplying the morphometric parameters derived from A-scenes by the corresponding scaling factor. However, this is not very practical since the number of A-scenes contained in different time series varies randomly and it is difficult to determine the value of the scaling factor for the image contrast equalization. For this reason, the geometric equalisation was carried out by means of image resampling using the Lanczos filter, as described in Section 3.2. As a result, all A-scenes with the size of 4096 x 2048 pixels included in basic time series were resampled to the smaller size of 2048 x 1024 pixels. This reduced the execution time of the HITS processing.

In addition, the scale of all images contained in HITS was corrected for the variable distance between the Sun and Earth, as described in Section 2.3. In this case, the estimate of the Sun-Earth distance in astronomical units according to Eq. (16) was used as the scaling factor. Figure 26 represents the Sun-Earth distance correction procedure. The distance function shown in cyan is estimated for the discrete times that correspond to Hinode data takes. The lower panel in Fig. 26 shows two graphs of the mean area (MA) of granular cells which was measured in the HITS-273** time series before (red) and after (blue) correction. The magnitude difference between the corrected and non-corrected morphometric signals does not exceed 1.5 %.

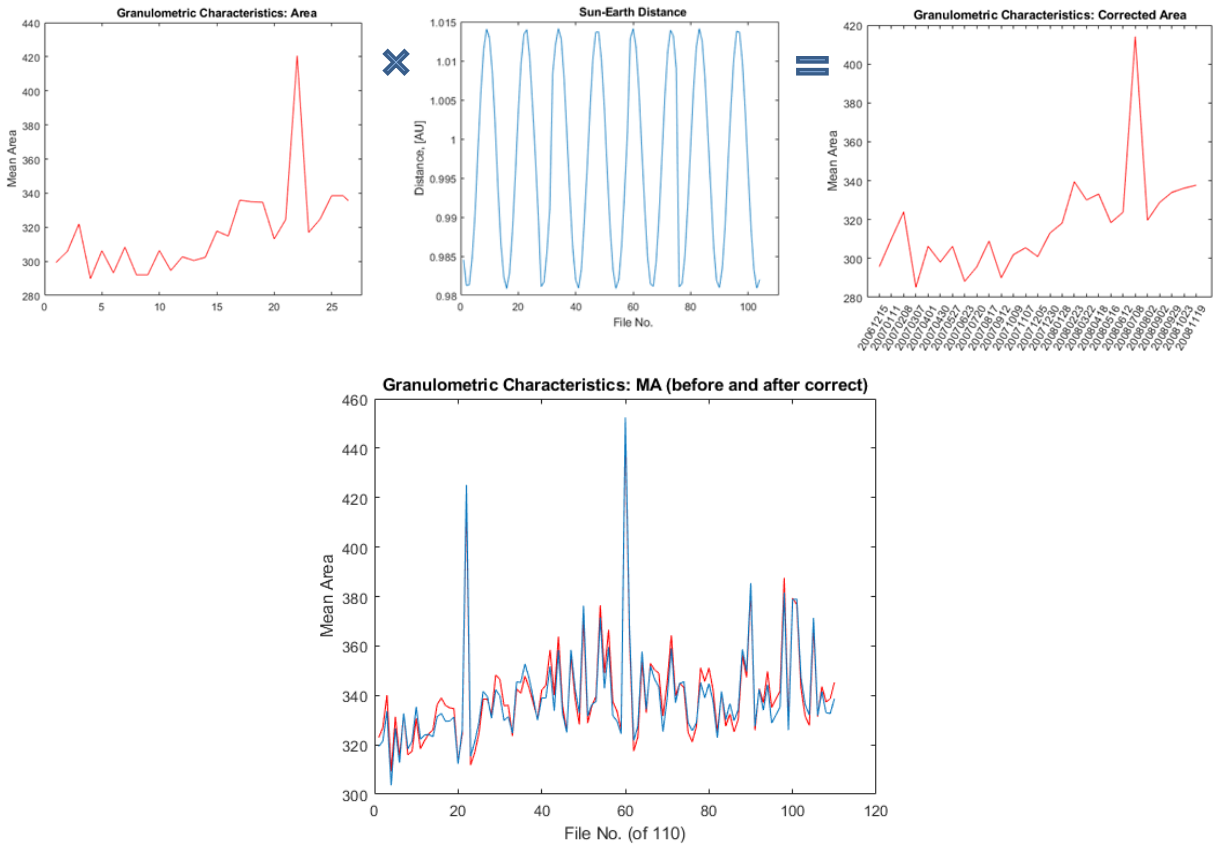

Figure 26. Correction of mean area measurements for the variable Sun-Earth distance

The correction procedure also includes an option to reformat timeline by converting the image sequence numbers to the Gregorian date or the number of days that have passed since the January 4, 2006, 03:30 p.m. UCT, the perihelium time closest to the first Hinode data take (See Section 2.3). The HITS-273** test time series still contains two blurry images that were

intentionally left to demonstrate the impact of image defocussing on the results of the granulometric analysis. Afterwards, all blurry images that caused outliers in morphometric measurements were removed from the analysis.

4.2 Processing 30- and 27-day time series

Two monthly and two synodic HITS time series with a cadence of 30 and 27 days respectively were processed to investigate the variability of solar granulation over the solar activity cycle. The 30-day interval between the data points in the monthly time series was considered useful for the statistical analysis of the granulation characteristics compared to the monthly average number of sunspots, while the cadence of 27 days in the synodic time series should be suitable for estimating granulation parameters measured in the same area around the solar disk centre. “Basic” HITS were temporarily shifted with respect to the “other” HITS by about 13 days, which corresponds approximately to half of the solar equatorial rotation period (see Section 3.2).

Initially, two HITS-30 monthly time series, each with 94 Hinode BFI images, were created from the IGAM archive data and processed using the MCW method described in the previous chapter. The processing resulted in few outliers due to several blurred images that were not previously recognized under visual control.[53] These scenes were rejected from further granulometric analysis. Therefore, the time series HITS-30-basic and -other are characterized by the lowest number of scenes, the longest cadence and the shortest execution time for their processing. The results of granulation measurements in the HITS-30-base time series are presented in the form of a timeline of the mean area, equivalent diameter, perimeter, extent, contrast and PAR of granular cells, as shown in Figure 27.

Then two synodic time series with 104 and 107 images were processed. The 10-year course of the mean granulation properties for surface convection cells, measured in the HITS-273-basic time series, is shown in Fig. 28. The corrected granulometric characteristics are shown in blue. The graphs are somewhat longer than those for the monthly HITS. The graph for the mean equivalent diameter is omitted because it is very similar to that of the mean area. Instead, a new graph is added to Figure 28, showing the ratio between the minimum and maximum values of the grayscale image intensities within the granular cell. This ratio characterizes the average image contrast of granular cells with the exception of the darkest parts of intergranular lanes.

At first glance it can be seen that even corrected values of all granulation properties are widely scattered. However, a closer look reveals the existence of some trends. The mean area, mean equivalent diameter and mean perimeter of the granular cells show similar behaviour with an increase of values in the first half of the graph and two maxima around scene No. 39 and 69 in HITS-30-basic or 49 and 92 in HITS-273-basic, while perimeter-to-area ratio varies in reversed way. The mean contrast values decrease steadily over time. The average extent[54] of granular cells and average min-to-max ratio show no trend.

---

[53] Images with the mean area of granular cells greater than 400 pixels or D_e > 23 pixels = 2.4” were treated as inappropriate.

[54] The cell extent is computed in accordance with Eq. (31) as the granular cell area divided by the area of bounding box.

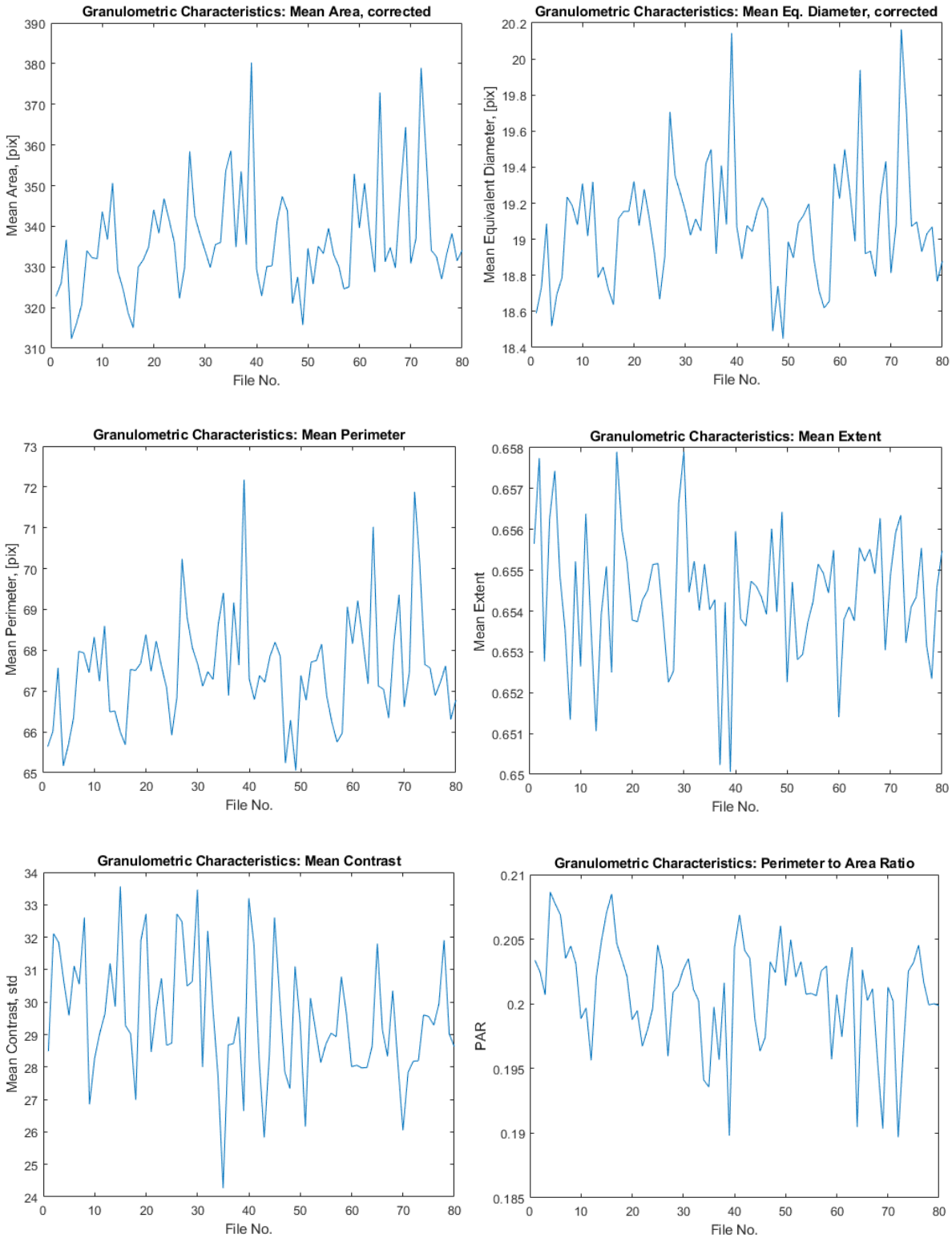

Figure 27. Corrected morphometric parameters of *granular cells* in HITS-30-basic time series including mean area, perimeter and contrast in the left column and mean equivalent diameter, extent and perimeter-to-area ratio in the right column

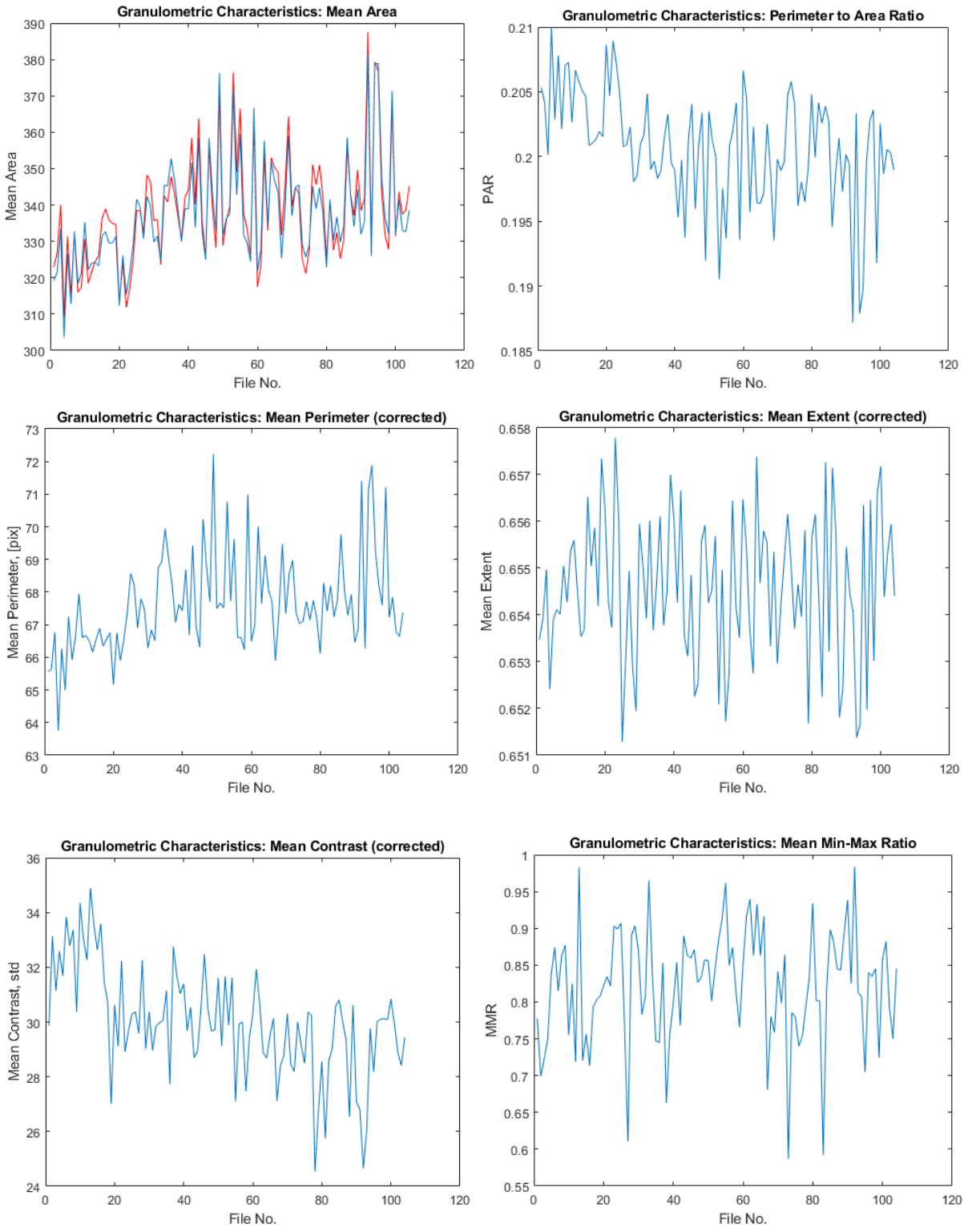

Figure 28. Corrected morphometric parameters of *granular cells* in HITS-273-basic time series including mean area (original in red and corrected in blue), perimeter and contrast in the left column, PAR, mean extent and min-max ratio in the right column

The granulometric results obtained with “other” HITS were very similar to those derived from “basic” time series. The relevant diagrams, which show the mean morphometric properties of the time series HITS-30-other and HITS-273-other and can be used to validate the results presented in this section, are listed in the appendix to this work. In addition, the average

morphometric parameters of granular cells measured in all corrected monthly and synodic HITS are summarized in Table 3 for the sake of comparison. The average values of the std-contrast are also given.

Table 3. Average morphometric parameters of *granules* and granular cells in HITS

HITS No.	Average area, pixel	Average perimeter, pixel	Average D_e, pixel	PAR	Average extent	Contrast, std(I)
30-basic	340	68.1	19.1	0.200	0.654	29.7
30-other	345	68	19.2	0.201	0.6545	30
273-other	339	67.8	19.1	0.200	0.6545	30.1
273-basic	338	67.7	19.2	0.200	0.655	30
273-basic	*162*	*53.75*	*12.66*	*0.332*	-	*15.5*

The values of the morphometric parameters given in Table 3 are very close to each other, which indicates the relative stability of the long-term solar granulation pattern and the constancy of the imaging characteristics of the Hinode optical telescope[55] as well as the stable performance of the MCW processing technique. This also points to the stationary character of the random process under investigation and shows the high demands on measurement accuracy and duration that are required to detect the trend signal.

In order to display the measurement results of the granulation scale concisely and to evaluate the precision of the granulometric processing, I have created several plots that show the mean area versus the mean perimeter of the granular cells in HITS-30 (top row) and HITS-273 (bottom row) time series. These plots are shown in Fig. 29.

In Figure 29, one asterisk denotes one image and the total number of asterisks in all four graphs is nearly 400. All graphics clearly show the linear relationship between the mean area and the mean perimeter. The deviation from the linear relationship is mainly due to the inappropriate quality of the individual images and the measurement error. The picture suggests that the most widely scattered set of granulation parameters is the one derived from the HITS-30-basic time series that was processed first (upper left graph in Fig. 29).

The area-perimeter relationship is also useful for estimating the size distribution of granular cells. The deviation from linearity in the upper right part of the graphs can also reflect the fact that larger granules have a more complex shape and a larger ratio of circumference to area.

Such plots show that the sharpening of images, e.g. after resampling, slightly influences the morphometric properties; it reduces the mean area of the identified granular cells by 6% and the mean perimeter by 3% (see Fig. 29, continued). This is shown for illustration purposes only. No sharpened images were used for the granulometric analysis.

The same processing was carried out to measure the morphometric properties of the granules identified in the HITS time series. The boundary of granules was determined at the $0.987 \cdot I_0$.

[55] Thanks to maintenance activities and corrective measures.

The results of morphometric measurements for granules are only shown for the longest HITS-273-basic time series in Figure 30.

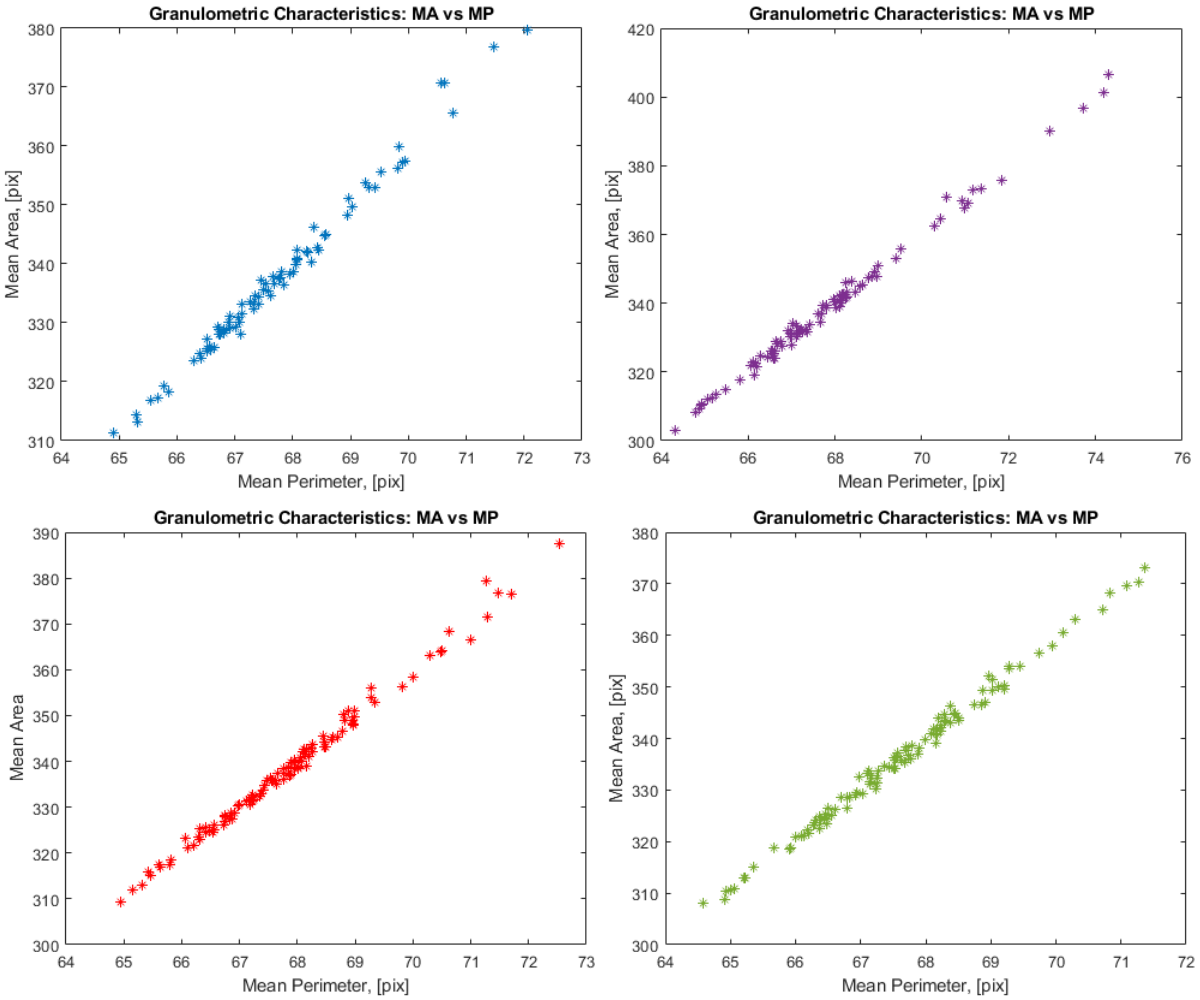

Figure 29. Area-perimeter relation of granular cells in HITS-30-basic (blue), HITS-30-other (lilac), HITS-273-basic (red) and HITS-273-other (green) time series

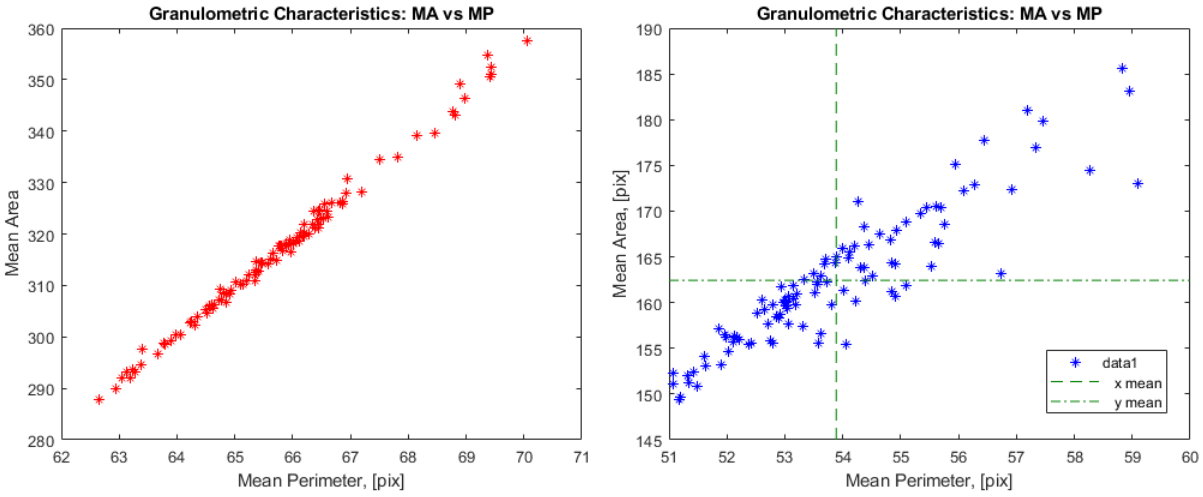

Figure 29 (continued). Area-perimeter relation of granular cells in the sharpened HITS-273-basic time series (left) and that of granules in the HITS-273-basic (right)

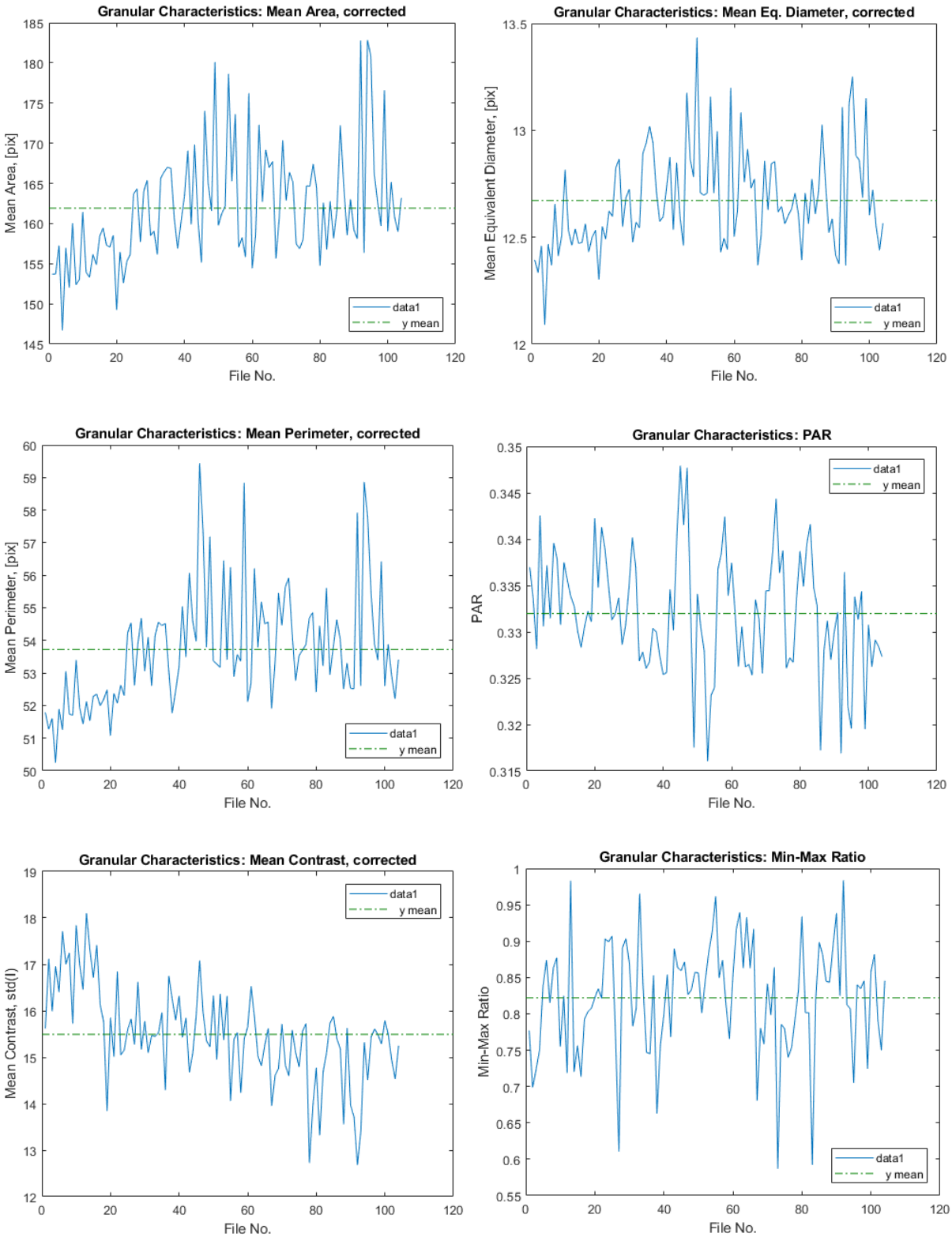

Figure 30. Corrected morphometric parameters of *granules* identified in HITS-273-basic time series: mean area, perimeter and contrast in the left column, mean equivalent diameter, PAR and min-max ratio in the right column

Graphs in Figure 30 also represent mean values of the granular parameters, which are summarized in the bottom raw of Table 3 (in italic) as averaged means. A comparison with Figure 28 shows that the temporal behaviour of the morphometric properties of granules is

very similar to that of granular cells, although the amplitudes and the variance of the parameters are very different.

The mean granular scale is measured at 12.66 pixels or 1.32 arcseconds, which corresponds to 958 km on the solar surface. The average granular area is almost half that for granular cells. The PAR value determined for granules is 1.5 times higher than that for granular cells, which indicates more complex outlines of granules. Accordingly, the morphometric parameters of granules are much more dispersed than those of granular cells. This is illustrated in the bottom right corner of Figure 29. In each Hinode scene, the number of granules is equal to the number of granular cells.

4.3 Processing daily time series

The very first comparison of the monthly and synodic HITS with the SSN time series was not very promising. For this reason, I decided to compare the granulation parameters derived from daily HITS with daily SSN data, which led to the creation and processing of three daily HITS, namely the time series HITS-2011-1234, HITS-2012-1234 and HITS-2015-1234.[56]

Therefore, the processing of daily time series included

- Processing of SSN time series,
- Processing of the HITS-2011-1234, HITS-2012-1234 and HITS-2015-1234 time series,
- Superposing and post-processing of daily SSN and granulometric time series (GTS).

Again, the main goal is to prepare Hinode and SSN data sets for quantitative joint analysis.

Processing daily SSN time series

SSN data series are regularly provided by the Sunspot Index and Long-term Solar Observations (SILSO), at the Royal Observatory of Belgium. [57] These SSN time series are regular in that, unlike HITS time series, they have no data gaps and their processing is straightforward. SILSO delivers sunspot data in the form of daily SSN, monthly mean SSN, 13-month smoothed monthly SSN and yearly mean SSN (http://www.sidc.be/silso/datafiles). No data point was considered incorrect in the SSN time series downloaded from the SILSO website.

The processing of SSN time series included their visualization, cutting out relevant fragments, modification, e.g. imitation of data gaps, temporal alignment and matching to granulometric time series. Figure 31 represents three typical (daily, monthly and monthly smoothed) and two pre-processed SSN data sets (monthly and daily), which were adopted for the joint analysis with HITS time series for the period 1996 - 2019. In the lower right corner, I added the timeline of granular area, which was derived from the HITS-273 basic time series, for comparison.

The fragments of the SSN time series shown in Fig. 31 were not matched with the HITS time series, i.e. they were not aligned precisely in time (X-axis). Nevertheless, a certain similarity

[56] These time series cover the first four months of a year with a cadence of one day.

[57] World Data Centre for the production, preservation and dissemination of the international sunspot number

can be seen in the temporal behaviour of the SSN fragment and the mean granular area, which are shown in two lower panels of the right column.

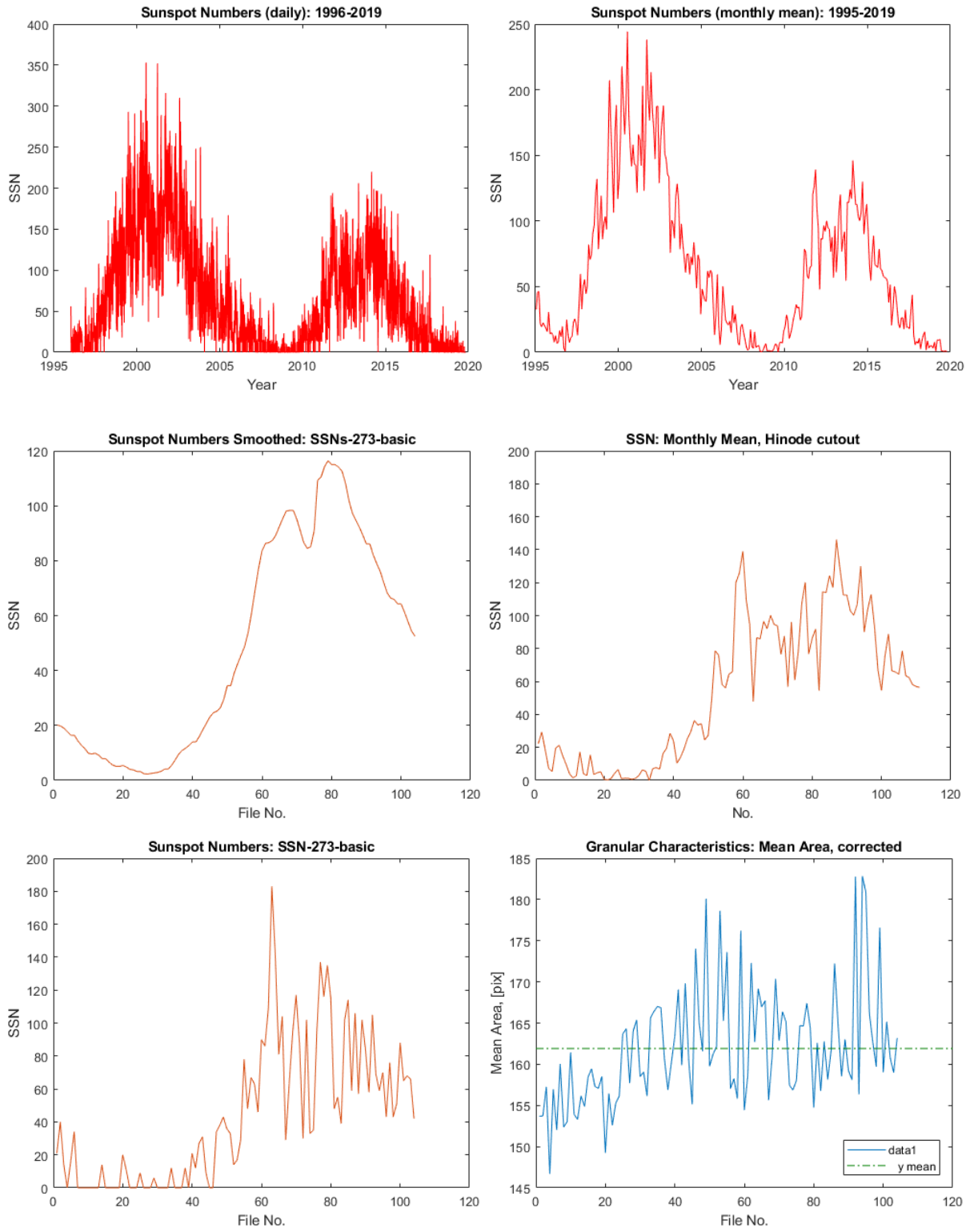

Figure 31. Visualisation of SSN time series: daily SSN, monthly mean SSN, 13-month smoothed monthly SSN, monthly mean SSN cut-out for the period of XII/2006 – II/2016 and daily SSN values sampled with 27-day time interval for the Hinode SOT operational period of 2006 – 2016. The timeline of granular area is added for comparison in the lower right corner.

Afterwards, the regular SSN time series were modified, aligned and overlaid with the piecewise regular HITS time series, as shown in Figure 32. The daily SSN data set shown in Fig. 32 (top left) represents all data gaps that exist in the HITS-273-basic time series, e.g. that in 2013. The approximate overlay in Figure 32 (top right) was used for the first (visual) qualitative comparison of the SSN and Hinode data sets.

It appears that the SSN graph in Fig. 32 (top right) is shifted forward in time compared to the mean area graph, as marked with an arrow. However, the shift value of 14 samples or 378 days (1 year and 13 days) is quite large. The exact alignment of the HITS and SSN time series with the tared time axis[58] in the lower row of Figure 32 shows even poorer match between the two data sets. Both, the blue and brown graphs in Figure 32 are very scattered. The extensive data gaps in the HITS time series and numerous zero values in the SSN time series bring about additional difficulties when comparing these data sets, which do not appear to be sufficiently representative for estimating the interrelation between data sets scattered in this way.

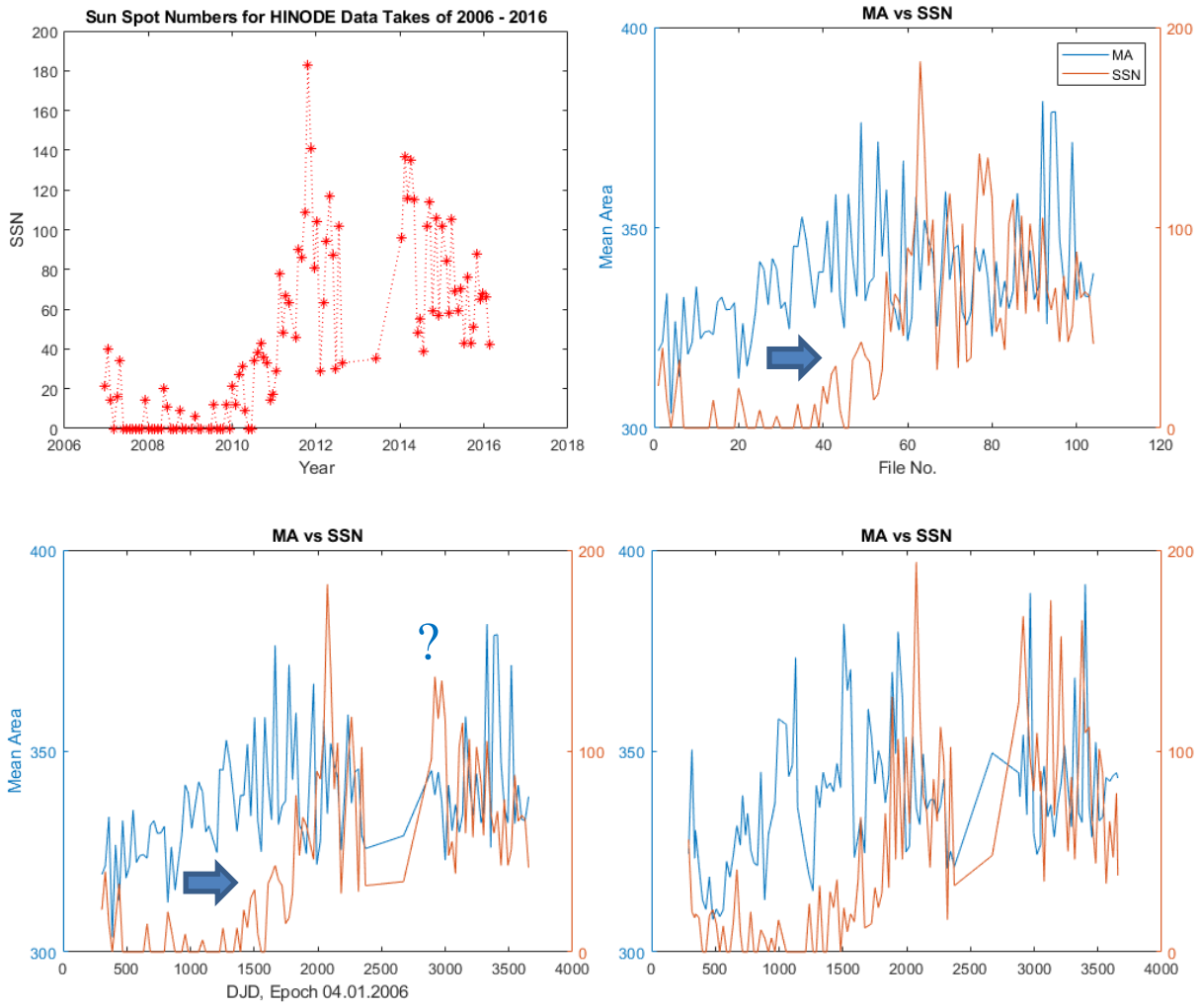

Figure 32. Daily SSN data set adopted to the HITS-273-basic time series (top left) and superposed with the mean area timeline of *granular cells* for HITS-273-basic (bottom left) and HITS-273-other (bottom right)

[58] In days passed since the epoch of January 4th, 1996, the first perihelion in the Hinode era.

The comparison with other time series such as HITS-30 and HITS-273-other did not bring any significant improvement because they have the same disadvantages as the HITS-273-basic (Fig. 32, bottom right). Also the graph of the mean granular area derived from the HITS-273-basic time series did not match the SSN data set well. The only consolation was the processing efficiency and reliability of the granulometric results obtained with different HITS time series.

Processing daily HITS

The comparison of the daily HITS with the daily SSN data was done in the hope of achieving less scattered results and a better match between these data sets. This was a kind of rescue mission. And it helped. Indeed, the granulometric processing results obtained with the HITS-2011-1234 and HITS-2012-1234 time series were less scattered than those obtained from the synodic and monthly time series. Figure 33 shows corrected morphometric parameters of granular cells for the first four months of 2011 (in the left column) and 2012 (in the right column). The granulometric graphs for the time series HITS-2015-1234 are included in the Annex B (Figure C). The average morphometric parameters of granular cells in three daily HITS are summarized in Table 4.

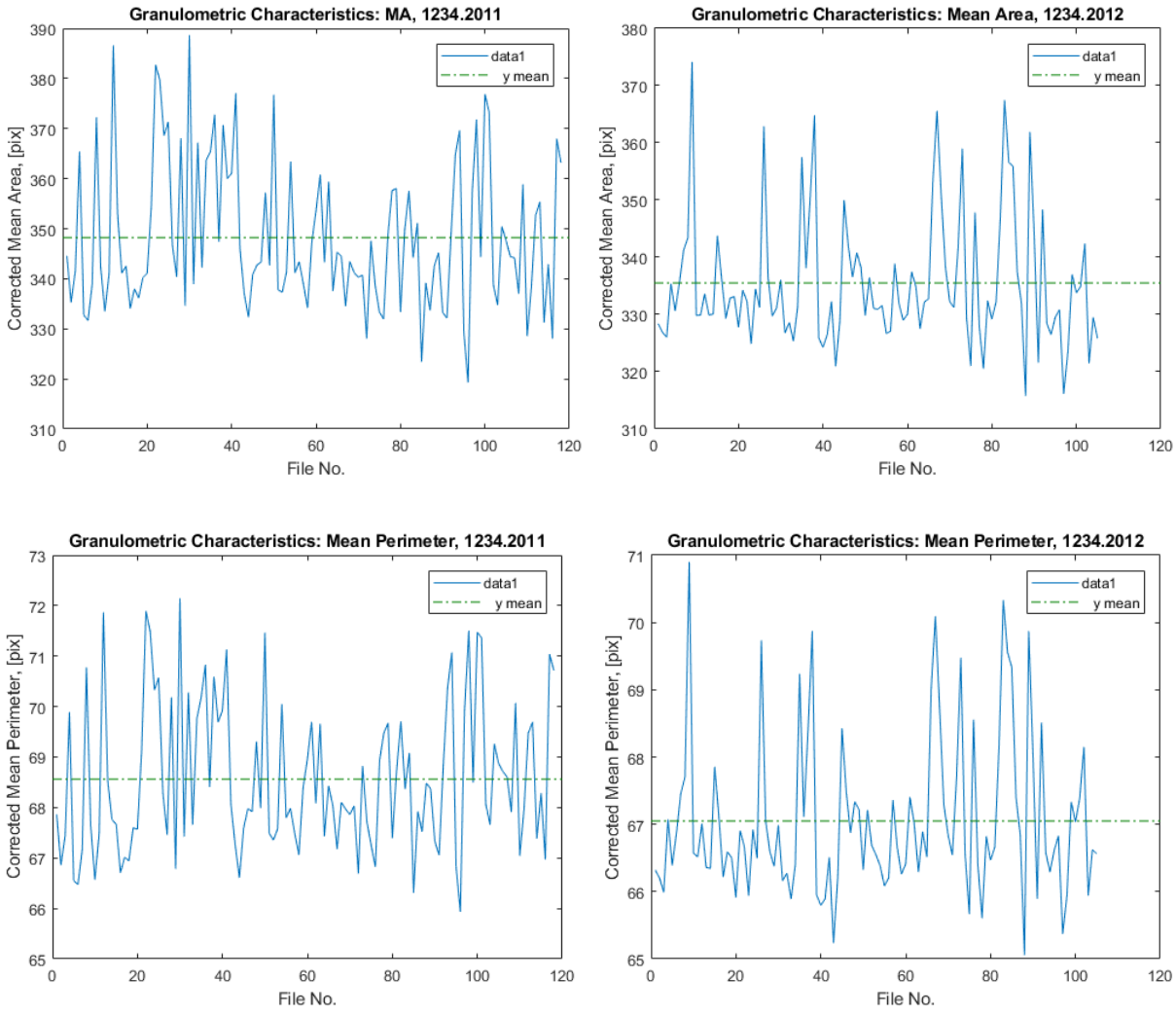

Figure 33. Corrected morphometric parameters of granular cells derived from the daily HITS-2011-1234 (left column) and HITS-2012-1234 (right column).

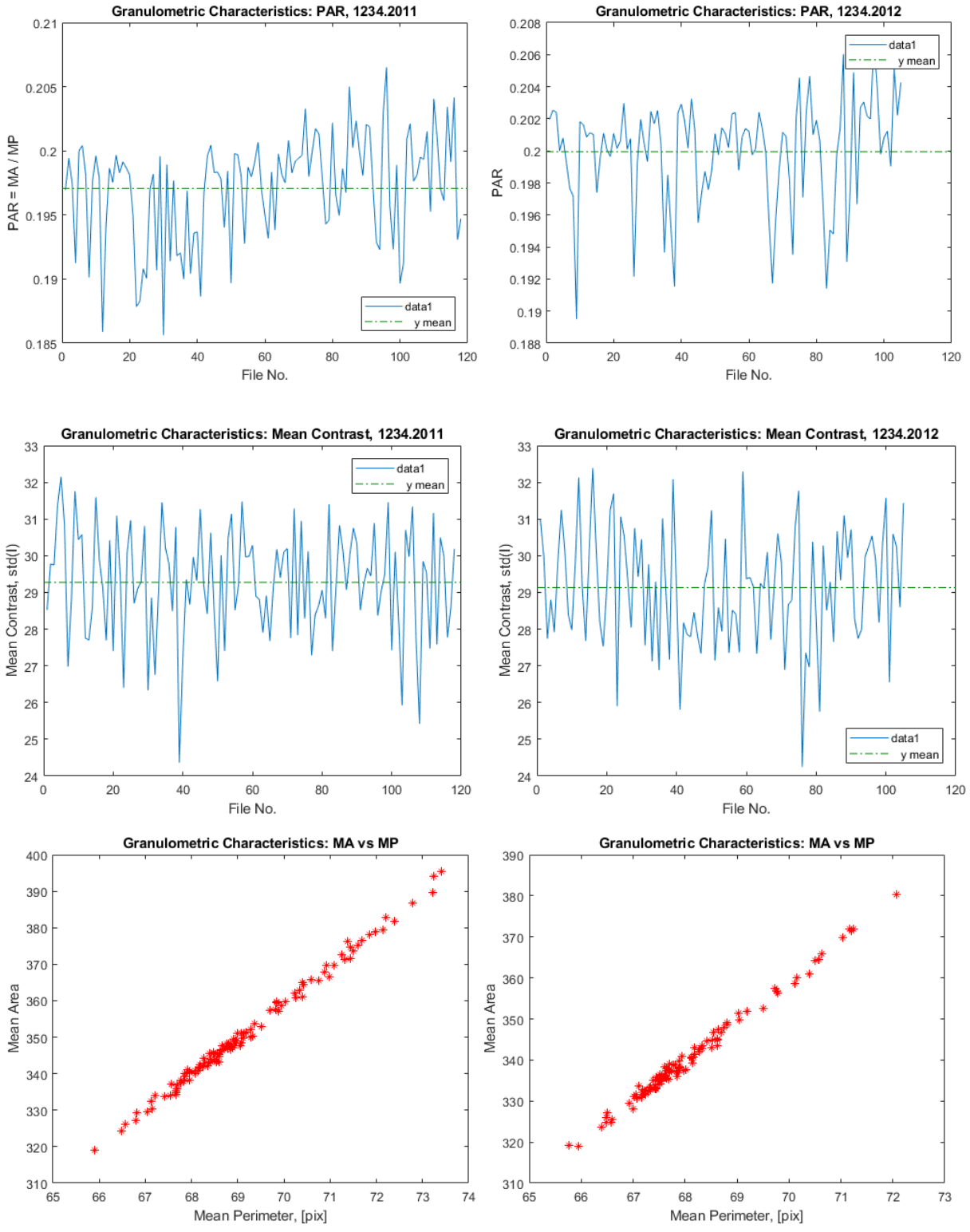

Figure 33 (continued). Corrected morphometric parameters of granular cells derived from the daily HITS-2011-1234 (left column) and HITS-2012-1234 (right column).

The comparison of Figs. 27 to 30 with 33 indicates that the results shown in the latter were less dispersed, although the average values of the granulation parameters were very similar to those given in Table 3. Keep in mind that the daily HITS include only the images that were taken under the best survey conditions during the seasons with moderate solar activity. The daily time series of 2011 and 2012 are long and fairly regular (see sections 2.3 and 3.2). The

short cadence of the daily HITS and the better agreement with continuous natural processes on the surface of the quiet sun also seem to be the reason for the homogenization of the granulation parameters.

Table 4. Average morphometric parameters of granular cells in daily HITS

HITS No.	Average area, pixel	Average perimeter, pixel	Average D_e, pixel	PAR	Average extent	Contrast, std(I)
2011-1234	348	68.6	19.3	0.197	0.648	29.3
2012-1234	336	67.1	19.0	0.200	0.644	29.1
2015-1234	342	67.7	19.1	0.198	0.647	28.4

All of the morphometric properties specified in Table 4 clearly show the decrease in the cellular scale with the increase in solar activity between winter 2011 (SSN_0 = 60.5) and winter 2012 (SSN_0 = 79.3), while the average contrast value characterizing the image quality remained almost equal. The similar image quality in the daily HITS of 2011 and 2012 is also identified with the scatterplots in Figure 33 (bottom row). There was also a slight increase in the scale of granular cells between 1234.2012 (SSN_0 = 79.3) and 1234.2015 (SSN_0 = 73.6). Figure 34 shows two daily SSN time series that correspond to data points in HITS-2012-1234 and HITS-2015-1234.

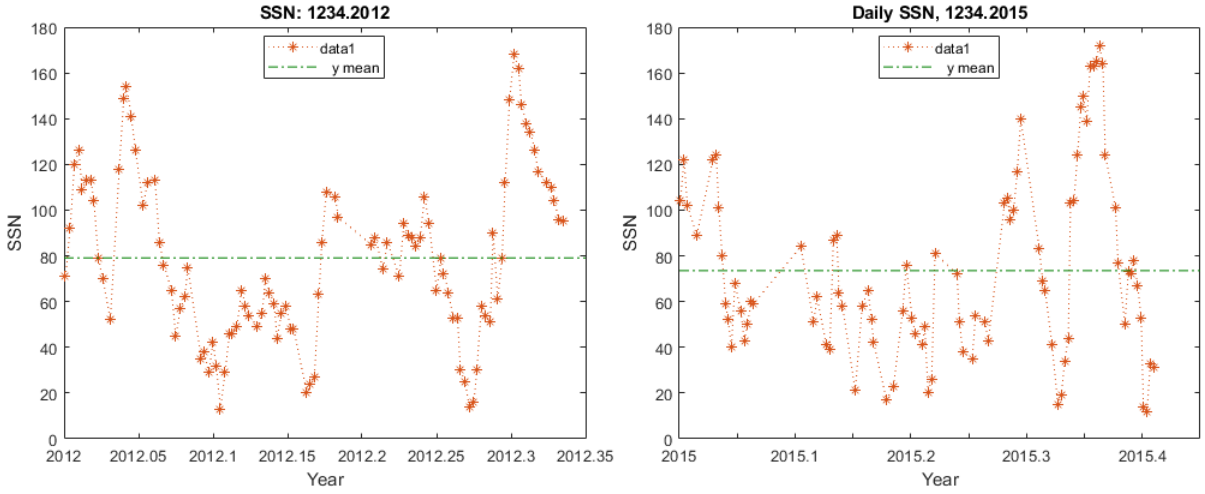

Figure 34. Daily SSN corresponding to data points in HITS-2012-1234 and HITS-2015-1234

Superposing and post-processing of daily granulometric and SSN time series

The time series of the granulation parameters, which resulted from the processing of the daily HITS, were overlaid with the corresponding SSN data for the common statistical processing and analysis. All time series were matched in pairs and aligned in time before their overlap. Figure 35 shows the superposition of the corrected time series of granulation parameters (in blue) with the daily SSN values (in brown, scaled on the right vertical axis).

The most prominent feature that can be clearly seen in all diagrams of Figure 35 is the inverse relationship between the course of the cellular scale and that of SSN. At best, this can be seen

on the right picture of the middle row, which is a kind of close-up of the left picture. Interestingly, the course of the mean extent of granular cells in all daily time series shows a good agreement with the general SSN trend, while it showed no trend in monthly and synodic time series. Conversely, corrected values of the mean contrast show no trend in the daily representations. In the Annex B, several additional superimposed diagrams are attached, which show the temporal behaviour of the mean contrast and the PAR ratio in relation to daily SSN.

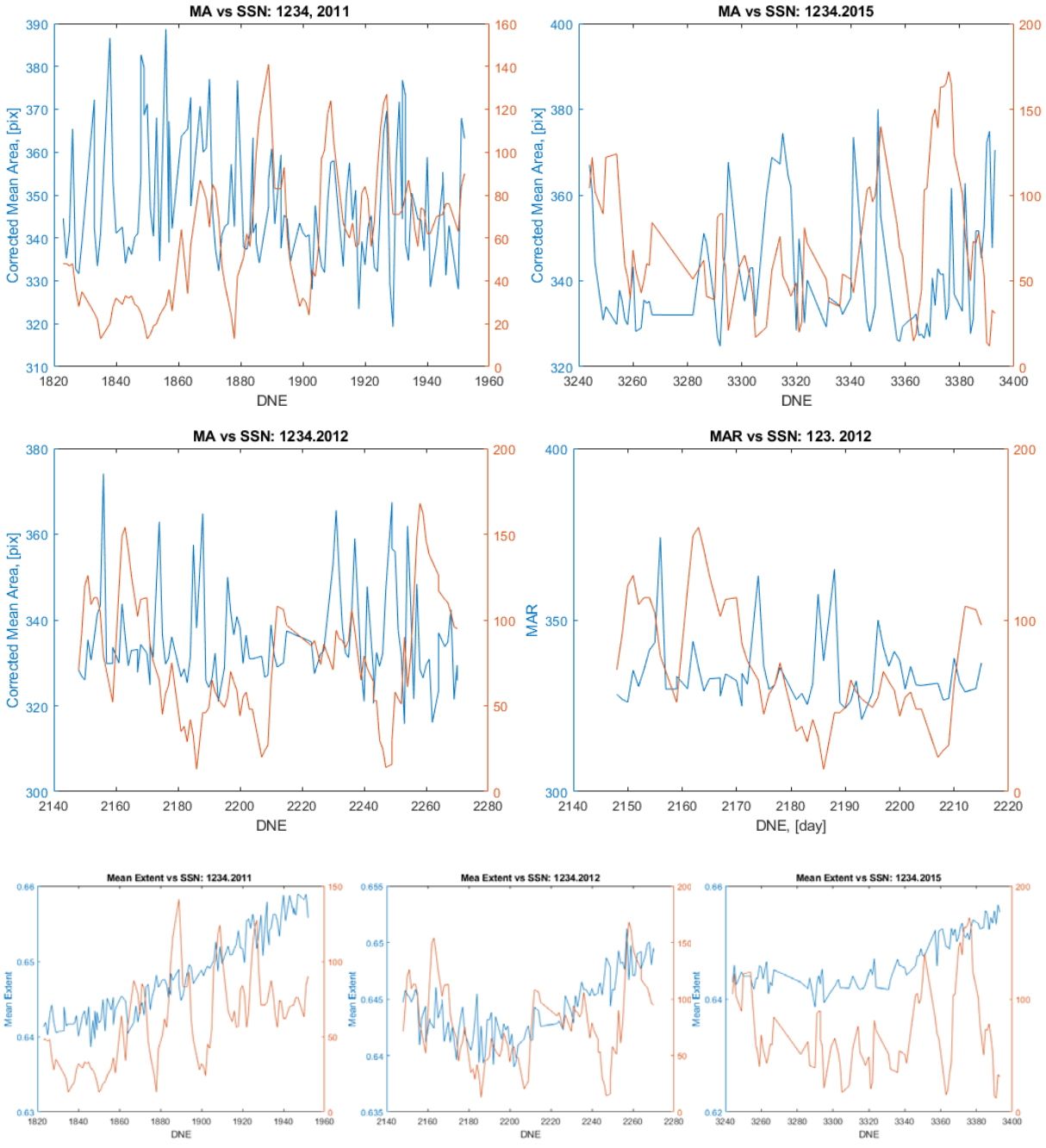

Figure 35. Superposition of SSN and GTS including mean area for the first four months of 2011 and 2015 (top row), mean area for the first four months and the first quarter of 2012 (middle row), mean extent values for the first four months of 2011, 2012 and 2015 (bottom row)

Both the SSN and granulometric time series (GTS) are very scattered and likely noisy. Therefore, it is difficult to manually estimate the relative intensity of statistical relationships between these data sets using graphs such as those shown in Figure 35. Fortunately,

polynomial trends in daily SSN and granulometric time series for the mean area of granular cells (GTS-A) also show an inverse relationship between these data sets. The polynomial trends in the SSN and GTS time series were determined using the MS Excel 2016 software.

An example of the inverse relationship between 4th order polynomial trends (in blue) in the SST (top) and GTS (bottom) data for the period of 1234.2011 is shown in Figure 36. The number of paired data points involved in the analysis is sufficiently large (118) and the determination of higher-order polynomials is justified. The comparison of the polynomial graphs in Figure 36 indicates the presence of an additional, probably linear trend that influences the SSN-GTS relationship.

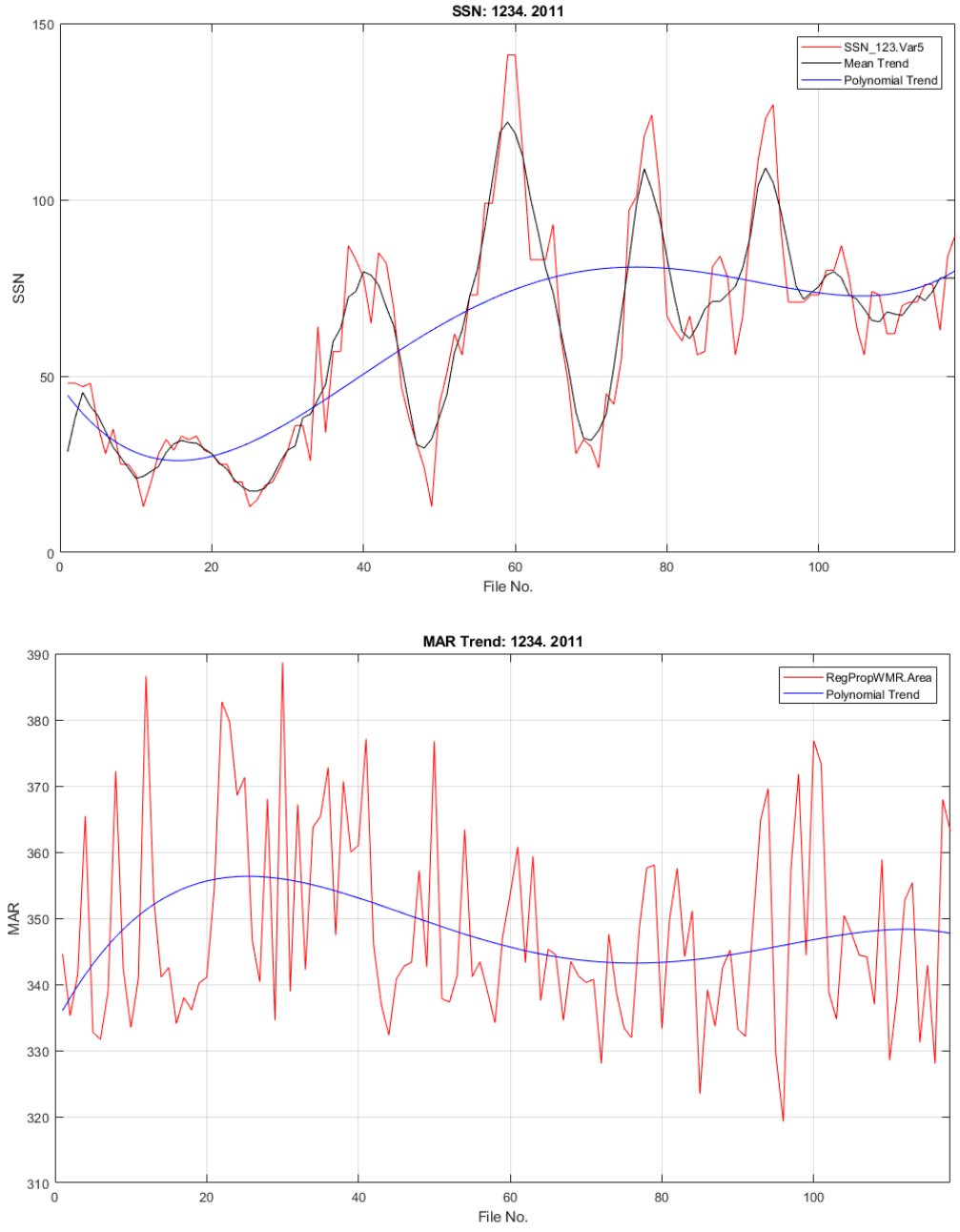

Figure 36. Inverse polynomial trends in daily SSN (top) and mean cellular area (MAR, bottom)

All of the graphics shown in Figures 35 and 36 met and even exceeded my expectations and were therefore subjected to detailed statistical verification, joint analysis and further validation.

Chapter 5. Analysis of results

The present chapter is devoted to the analysis of the results obtained in this work and describes

- cross-correlation analysis of granulation parameters and SSN,
- histogram analysis and summary of granulometric parameters,
- comparative review and validation of results,
- analysis of data processing efficiency,
- analysis of perspectives.

5.1 Cross-correlation analysis of granulation parameters and SSN

In previous sections, elements of the qualitative visual comparison between the granulometric and the SSN data set were briefly discussed. In this chapter, quantitative statistical relationships between granular, cellular, and SSN parameters are determined, displayed, and evaluated using conventional tools of cross-correlation analysis.

For two discrete-time sequences of real valued data *f[t]* and *g[t]*, the operation of cross-correlation $(f \star g)$ is defined as

$$(f \star g)[l] = \sum_{-\infty}^{+\infty} f[t] \cdot g[t+l] = \sum_{-\infty}^{+\infty} f[t-l] \cdot g[t] \,, \tag{37}$$

where τ denotes the displacement between two processes in time called lag and integer *t* is an arbitrary point in time (data point No). Cross-correlation is a measure of similarity between two random data series as a function of the lag (see also Eq. 36). A noticeable feature, e.g. local maximum in the function *f* at the instant *t* occurs in the function *g* at the time *t*+τ.

The simplest measure of the statistical relationship between two paired data sets *x[n]* and *y[n]* (variables) consisting of *n* pairs $\{(x_1, y_1), (x_2, y_2), \dots, (x_n, y_n)\}$ is the Pearson correlation coefficient, which is computed as (Veronig 2019)

$$r_{xy} = \sum_1^n (x_i - x_0) \cdot (y_i - y_0) / \left(\sqrt{\sum_1^n (x_i - x_0)^2} \cdot \sqrt{\sum_1^n (y_i - y_0)^2} \right), \tag{38}$$

where x_0 and y_0 denote the mean values of data sets. The correlation coefficient ranges from −1 (perfect linear anti-correlation) to 1 (perfect linear correlation). The implementation of these options in the statistical block of the SOGIS software is based on the MATLAB® xcorr and corrcoef functions using Eqs. (36 - 38).[59]

First I created scatterplots[60] and calculated correlation coefficients for three paired data sets including SSN and GTS-A for the first four months of 2011, 2012 and 2015. Correlation coefficients were given negative values in all three cases (Table 5). This confirmed the remark

[59] See Section 3.4.

[60] Scatterplot – scatter diagram wherein the independent variable is plotted along the horizontal axis, while the dependent variable is plotted along the vertical axis.

made in the previous section about the inverse relationship between the cellular scale and the SSN.

However, the absolute values of the correlation coefficient at zero delay were quite low, indicating a weak anti-correlation between the aligned SSN and GTS-A.[61] Scatterplots also indicate a statistically weak relationship between the SSN and GTS-A time series (Figure 37, left), although for smaller granular elements in the lower left corner of the scatter graph, a clearly negative correlation can be seen.

For some tasks in the further analysis, it is not the absolute values of the granulometric parameters that are actually interesting, but the deviations from the mean. So I added another version of the same scatterplot that shows deviations from the mean (Figure 37, right). In both of the scatterplots shown in Figure 37, the allegedly independent variable (SSN) is plotted along the vertical axis, while the dependent variable (GTS-A) is plotted along the horizontal axis. At the time of plotting, I didn't take care about the leading process because I didn't know it exactly.

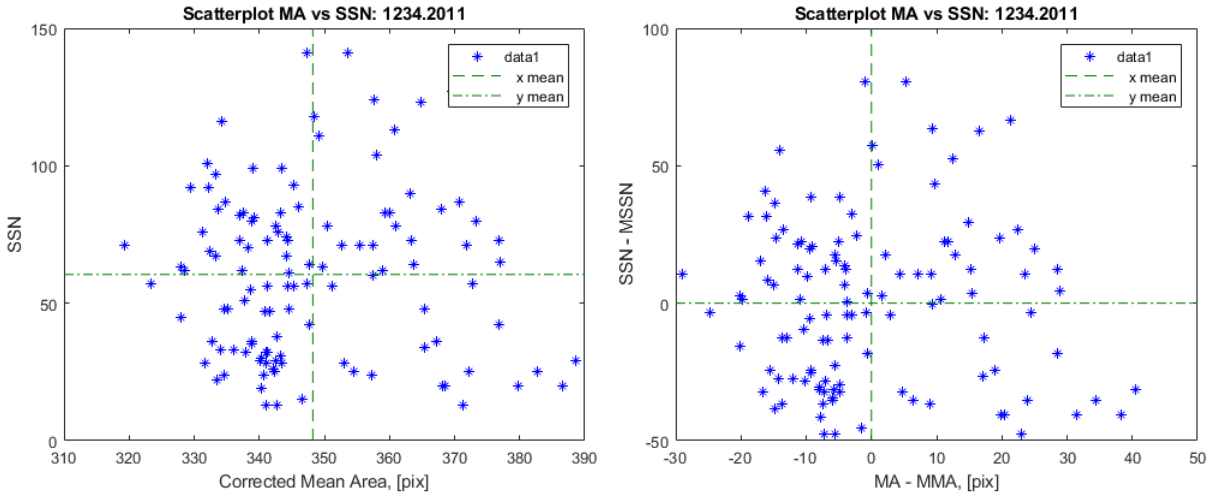

Figure 37. Two versions of scatterplots showing the absolute values (left) and deviations from the mean (right) of the SSN and GTS-A data records in the period 1234.2011

Table 5. Correlation coefficients of daily SSN and GTS-A time series

Time series No.	Correlation coefficient at zero lag	Correlation coefficient at the second extreme	Correlation coefficient at the third extreme
2011-1234	-0.04	-0.34	-0.24
2012-1234	-0.17	-0.45	-0.32
2015-1234	-0.17	-0.37	-0.14

To evaluate the cause-effect relationship between the SSN and GTS time series and to reveal the existence of a potential time shift between the causal process and the response to it, the cross-correlation function was calculated. In practice, I calculated the normalized cross-correlation that is common in time series analysis and got the Pearson correlation coefficient

[61] GTS-A - Granulometric time series for the corrected mean area of granular cells.

as a function of time, i.e. the lag. A diagram representing the unsigned function of normalized cross-correlation between the SSN and GTS-A time series is given in Figure 38 (left). The signed variant of cross-correlation (XCOR) for the period 1234.2011 is shown in Figure 38 (right). The first extreme of the XCOR function corresponds to the zero lag value.

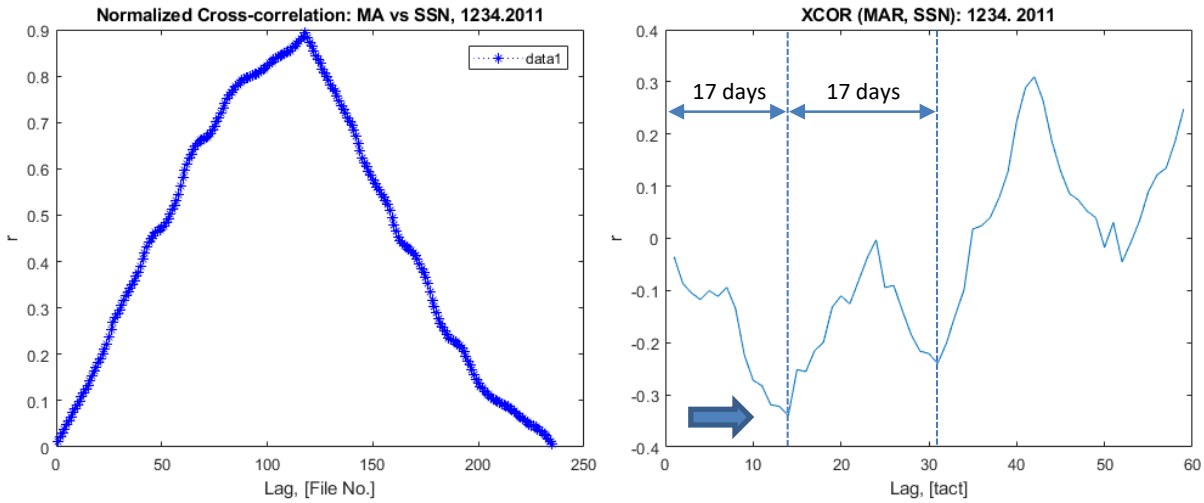

Figure 38. Cross-correlation between the aligned SSN and GTS-A time series: unsigned normalized (left) and signed normalized (right)

The XCOR function in Fig. 38 (right) shows a periodic behaviour in the form of a negative sine function depending on the delay value. The XCOR absolute value attains its maximum marked with an arrow at the lag value of 14 data points or 17 days.[62] The next (third) extreme of the cross-correlation function is reached at the delay value of 31 points or 34 days. A very similar course of the cross-correlation function was obtained for the SSN and GTS-A time series from 1234.2012 and 1234.2015. The values of correlation coefficients of daily SSN and GTS-A time series at the second and third extremes are also specified in Table 5. The minimum value of r_{xy} achieved for the 1234.2012 was -0.49 (see Figures D and E in the Annex B).

The absolute r_{xy} values are not very high, but I think they are fairly significant and representative given the scattered and likely noisy nature of the signals being compared. The results of the correlation analysis can be improved if, prior to the calculation of the correlations, the low-frequency components caused by the noise are removed from the measured signals by filtering. The normalization of the signals to be compared, e.g. by dividing to the maximum value, also increases the absolute value of r_{xy} (see Annex B).

For the period 1234.2012, the XCOR function reaches the second extreme with a delay of 14 days and the third at 28 days. The delay value of 14 days corresponds approximately to half of the solar equatorial (synodic) rotation period. The equidistant position of the first three extremes in the XCOR function was also found for the time series 1234.2015. Note that the delay value indicates the point in time at which the SSN and GTS-A time series are best matched and their XCOR function reaches a minimum if they are interrelated inversely. The positive sign of the delay between the SSN and GTS time series designates the former as the

[62] Due to the 3-day data gap in January 2011, the cadence of the time series does not correspond to one day.

leading process that occurs earlier. This observation confirms the statement made in section 4.3 about the SSN data set shifted forward in time compared to the granulometric data set. I think it makes sense to call sunspot activity a precursor process compared to solar granulation activity. Several additional graphs showing the course of the XCOR function are included in the Annex B.

Still, the different delay values obtained with different GTS time series are waiting for the plausible explanation. We believe that the variable latitudinal distribution of the sunspots on the solar surface could play an important role in this concern. A simple scheme for interpreting the delay between the SSN and GTS-A data is shown in Figure 39. Remember that only Hinode scenes without sunspots were selected for the granulometric analysis. In this context, the concept of persistently active solar longitudes developed in (Berdyugina & Usoskin 2004, Gyenge et al. 2012) appears interesting. The existence of an additional aperiodic trend, which could explain the skewed form of the negative sine function in Fig. 38, must also be proven both empirically and theoretically.

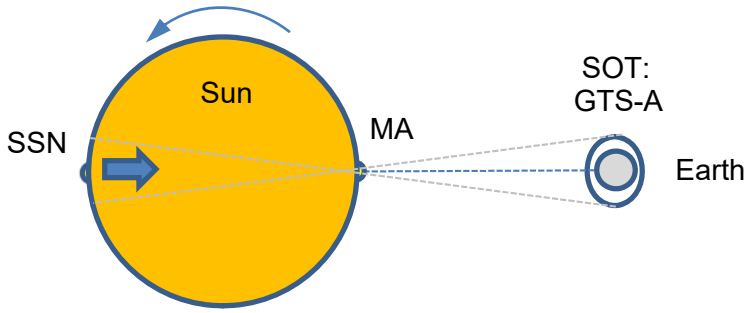

Figure 39. Simple scheme for the SSN - GTS-A delay interpretation (view from the North)

The importance of the correlation analysis described in this section is that it confirms the results obtained earlier and positively supports / verifies the working hypothesis about the dependence of the granulation parameters on the SSN and on the solar activity cycle. The anti-correlation and the time lag between the causal and effect processes determined in this section provide additional information for the interpretation and understanding of the dynamic behaviour of the solar surface convection.

5.2 Histogram analysis. Summary of granulation parameters

In order to identify possible effects of methodological restrictions and image processing imperfections on the granulometric results and to summarize the morphometric parameters of granules and granular cells, the histogram analysis was carried out using the statistical module of the SOGIS software. Typical histograms showing frequency distributions for the main morphometric parameters of granular cells in the HITS-273-other and HITS-2011.1234 time series are shown in Figure 40. Most histograms are skewed, i.e. they are asymmetrical and their distribution peak is off centre.

Depending on the direction of the tail, the mean area cell, the perimeter and the equivalent diameter show right-skewed distribution, with the number of small granular cells decreasing sharply. The natural limit that prevents the occurrence of smaller granular cells is image resolution. Conversely, the mean contrast of granular cells shows the left-skewed distribution with elements of the comb distribution; the latter is due to the limited number of grey levels in

8-bit image mode and rounded-off data, while the former is caused by the finite width of the contrast-frequency characteristic of Hinode images. Only the mean extent of granular cells[63] shows the normal distribution, with data points occurring on each side of the average with the same probability. In Figure 40, two last histograms in the lower row (middle and right) show the distribution of the extent values for the granular cells identified in the synodic HITS-273-basic and daily HITS-2011.1234, which in both cases are very close to the normal distribution[64]

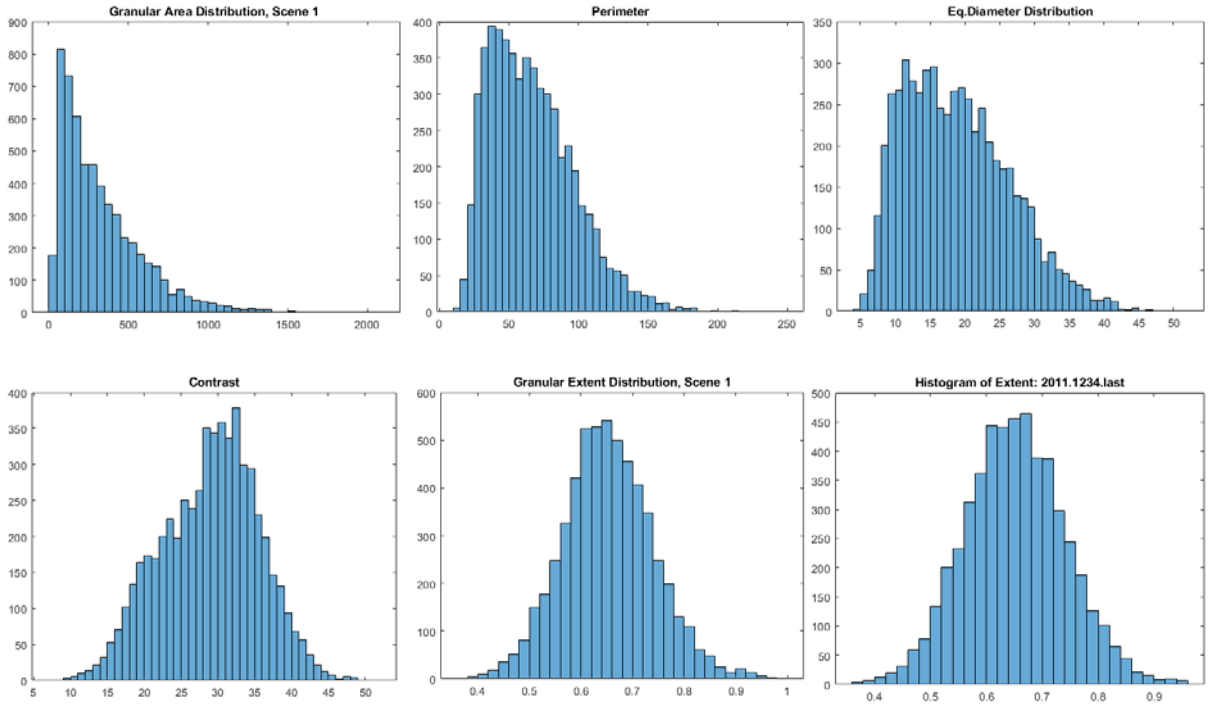

Figure 40. Typical histograms of granulation parameters: right-skewed distribution of the granular area, perimeter and equivalent diameter (top row), left-skewed distribution with elements of comb distribution for granular contrast and almost normal distribution of the granular extents (bottom row).

This observation indicates one of the shortcomings in the statistical analysis of the granulation properties: the mean value of the cellular scale does not correspond to the highest frequency of its occurrence. Accordingly, the total area of the granular cells identified within the image frame cannot be estimated by multiplying the mean cellular area by the total number of granular cells. This finding corresponds to the observations of other investigators. For example, in (Müller 1989) it was already mentioned that the number of granules rises sharply to the limit of the image resolution. The same apparently applies to the size of the granular cells.

Still it's surprising that the normally distributed mean extent of granular cells was seldom used for the characterization of the morphometric properties of solar granulation. Taking into account the similar courses of the mean cellular extent and polynomial trend in the daily SSN

[63] The cellular extent was computed as the cellular area A_{gc} divided by the area of the bounding box A_b, as given by Eq. (31).

[64] The comb distribution of the extent values for granules is also remarkable.

(see section 4.3), this morphometric parameter is very interesting for granulation studies. In contrast to the mean extent, the mean equivalent diameter was often used for describing the morphology of granules and supergranules (Roudier et al. 2018).

The histogram analysis allowed the typical, most frequently occurring values of granulation parameters called peak values or peak parameters to be measured precisely. I managed to put the mean and peak values of all granulation parameters in one Table 6. In Table 6, the peak morphometric parameters of granular cells were derived from the histograms in Figure 40, while the mean parameters of granular cells are averages of the corresponding values for four synodic and monthly time series and three daily time series, which were given in Tables 3 and 4. All parameters describing the granular scale are given in pixels. The pixel scale is 0.104" or 75 km on the solar surface. The pixel area is $75^2 = 5625$ km² (0.0117 arcsec²).

Table 6. Main morphometric parameters of solar granulation [1 pixel = 0.104"]

Mean area, pixel	Peak area, pixel	Mean D_e, pixel	Peak D_e, pixel	Mean perim. pixel	Peak perim. pixel	PAR	Mean extent	Peak extent	Mean contr.
Granular cells, synodic and monthly HITS									
340	100	19.2	12	67.9	40	0.200	0.6545	0.66	30.0
Granular cells, daily HITS									
342	100	19.1	12	67.8	50	0.198	0.646	0.68	28.9
Granules, synodic HITS									
162	30	12.7	5	53.8	20	0.332	-	0.60	15.5

Figure 41 shows two histograms of the contrast values for granule cells which were identified in the daily HITS-2011.1234 (left) and for granules which were identified in the synodic HITS-273-basic (middle). Compared to the left-skewed contrast distribution for granular cells, the contrast values for granules have a bimodal distribution that indicates the presence of two sub-processes with different distributions. Interestingly, the histogram of the maximum intensity values for granules in Figure 41 (right) also shows the bimodal distribution with a few number of very bright granules.

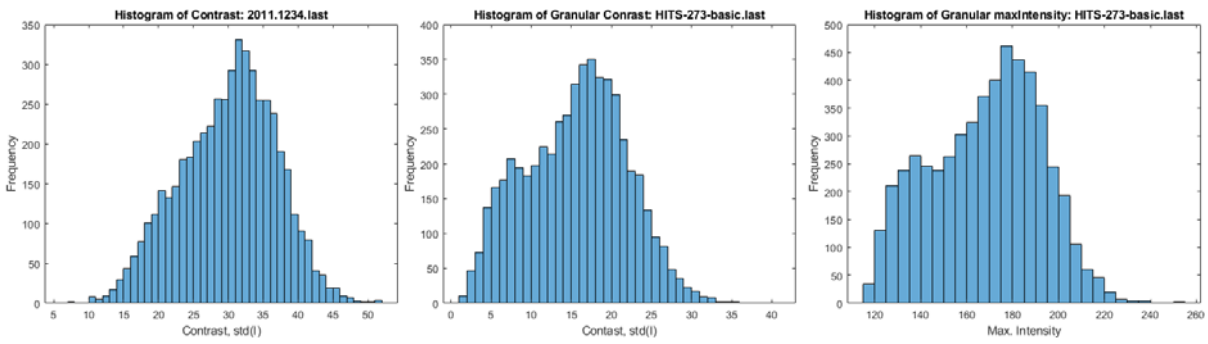

Figure 41. Histograms of contrast values for granular cells in daily HITS-2011.1234 (left) and granules in monthly HITS-273-basic (mid); histogram of maximum intensity for granules (right)

The data summarized in Table 6 clearly show that the peak values of the morphometric parameters for granular cells and granules are significantly lower than the mean values and only the value of peak extent is very close to the mean. The peak contrast values (not shown in Table 6) of 33, 32 and 18 for the first, second and third rows of Table 6, respectively, are higher than the mean. Such a summary of the granulation parameters is undoubtedly useful for the comparison with the results of other researchers and further studies of solar granulation based on new observation techniques and processing methods.

5.3 Comparative review and validation of results

The comparison of multitemporal histograms described in the previous section revealed no unusual events that could influence the granulation properties of the HITS time series. All granulometric characteristics show continuous distribution of values. However, the morphometric properties of granules and granular cells differ statistically and only those of granular cells can be described by Gaussian distribution. The mean and median morphometric properties of granules aren't equal. This should be taken into account when comparing the granulation properties measured with different techniques for granules and granular cells.

Nevertheless, the mean values of the morphometric parameters for granules and granular cells given in Table 6 can be compared directly with the granulometric results measured and modelled by other researchers. Unfortunately, there are only a few publications that report morphometric parameters of granular cells, and the inter-validation between the results obtained in this work and in other research must be based on the comparison of granular parameters.

The scale of granules measured in Hinode images by (Muller et al. 2018) and corrected for the annual variation of the Sun-Earth distance was reported to range between 1.52 and 1.58 arc seconds. Then, in terms of Hinode pixels, the mean granular scale varies between 14.1 and 15.2 pixels. This is slightly larger than the mean equivalent diameter of the granules, which was measured at 12.7 pixels in this work. In (Muller et al. 2018) the mean rms contrast of granules varied between 12.0 and 12.8. However, the value of corrected contrast was given as approximately 14.5, which is close to the value of std-contrast given in this work as 15.5.

In (Pötzi 2009), the mean perimeter of granules varies between 5 and 5,5 arc seconds or 46.3 and 51 pixels, which corresponds well to the mean value of 53.8 pixels given in Table 6. The mean granular distance of 1.4 – 1.6 arcsec or 13 – 14.8 pixels given in (Pötzi 2009) is also close to the mean equivalent diameter of the granules specified in Table 6. In (Pötzi 2009), however, the average area of granules is 1.1 arc seconds² or 104 pixels, which is considerably smaller than the value of 162 pixels determined in this work. The mean area of granular cells measured by W.Pötzi is 1.0 arc seconds² or 85.7 Hinode pixels and is smaller than that of granules, which does not correspond to the definition of a granular cell.

Most of the granules used to numerically model the granular properties in (Gadun et al. 2000, Lemmerer et al. 2019) are in the range of approximately 400 to 2500 km or 5.3 to 33 Hinode pixels. Both mean equivalent diameters given in Table 6 as 12.7 pixels for granules and 19.1 or 19.2 for granular cells fall within this interval. According to (Yu et al. 2011), the mean diameter of granules varies between 0.8 and 3 arc seconds or 7.4 and 27.8 Hinode pixels. Again, this includes well the mean value of the equivalent diameter given in Table 6.

Maximum intensities of granules were given as 1.2 – 1.6·I/I_0. This corresponds to the histogram values shown in Figure 41, right. According to the graphs shown in (Gadun et al. 2000), the mean min-max intensity ratio for granules is approximately 0.83, which is close to the average of 0.82 shown in the lower right graph of Figure 30 in this thesis.

The area-perimeter factor for granules f_{AP} introduced in (Hirzberger 2002) as

$$f_{AP} = 4\pi \cdot A_g / P_g \,, \tag{39}$$

where A_g and P_g denote the granular area and the perimeter,

can be rewritten as $$\sqrt{f_{AP}} = \pi \cdot D_e / P_g \tag{40}$$

or as $$0.3183 \cdot \sqrt{f_{AP}} = D_e / P_g \,, \tag{41}$$

where D_e is the mean equivalent diameter of the granules.

J.Hirzberger reported the peak values of f_{AP} as 0.16 and 0.58, which means that the ratio D_e/P_g varies between 0.127 and 0.242. In this work, the ratio D_e/P_g is equal 0.236 which is well within the specified interval.

A fairly universal parameter for comparing granulometric results is the total number of granules (or granular cells) identified in the full frame of the Hinode image. This value was published in (Hanslmeier et al. 2010) for the period of solar minimum in December 2006 – June 2009. They detected approximately 4000 granules in the half of the Hinode scene (1024 x 1024 pixels), while the mean granular area was measured at $6.3 \cdot 10^5$ km² or 112 Hinode pixels. The median value of granular segments was given as $3.7 \cdot 10^5$ km² or 65.8 pixels (Hanslmeier et al. 2010).

The mean granular area of 162 pixels given in Table 6 differs by 30% from the mean granular area given in (Hanslmeier et al. 2010). The average total number of granules and granular cells recognized in the full image of the Hinode image (2048 x 1024 pixels) in this work is 6400 or only 82% of the Hanslmeier value.

Now it is difficult to decide which measurement is more accurate, but I think that the problem of under-segmentation typical of the MCW segmentation algorithm mentioned in section 3.4 could play a crucial role in this matter. In addition, a substantial relative number of truncated granules, which increases with decreasing frame size, also affects the number of identified granules and the mean granular area. Finally, image filtering was not performed in this work, and the degraded quality of some slightly blurry images could lead to an increase in the size of the granular cells and a decrease in the total number of granules.

All in all, the average morphometric parameters of granules, which are given in this work and published by other researchers differ. The difference, however, is not drastic and cannot badly affect the achievement of the study goal, which only requires systematic measurements of numerous images of constant quality with uniform standard precision. I believe that this requirement has been met. Thanks to multiple tests and quality control measures for estimating the accuracy and checking the image processing performance, which are described in section 3.4, the validation of the main results achieved in this work was successfully completed.

5.4 Analysis of processing efficiency

The efficiency of data processing can be measured in terms of the time required for the end-to-end processing of a unit of input data. In this work a single full-frame grayscale Hinode BFI image with the size of 2048 x 1024 pixels and 8-bit pixel depth was considered as the unit of input. A total of 710 such Hinode BFI images were processed with the SOGIS software written by the author of this work. These Hinode images were saved in TIFF format and the storage size of each TIFF image was 2,049 KB.

To estimate the execution time for smaller parts of the SOGIS code, I used tic and toc markers. The MATLAB ® Profiler was used to assess the performance of the entire SOGIS code. The execution time for the pre-processing of 120 Hinode scenes with the size of 4096 x 2048 pixels, which were resampled to the smaller size of 2048 x 1024 pixels, was not recorded. Due to the gradual complication and continuous optimization of the SOGIS program, the processing time of an image changed constantly. Within three working months of the implementation phase, the SOGIS execution time was reduced six times from 15 seconds to 2.5 seconds per image.

The execution (lapse) time of 2.5 seconds includes the time for data preparation, granulometric segmentation, measurement of granulation parameters, joint analysis of granulometric and SSN data including computation of correlation functions, plotting several most necessary graphics and storing results. Plotting requires a lot of computing time. Therefore, most of the plotting options have been turned off in routine data processing.

In the end, I was satisfied with the software performance because processing of the entire image time series such as HITS-273-basic or HITS-2011.1234 did not take longer than 5 minutes. The entire data processing was carried out using a student PC No. 9 with 8-GB RAM and 3-GHz Intel processor in the TUG Computing Centre in Steyrergasse 30, 8010 Graz. The execution time of 2.5 seconds is a good indicator for such a machine.

The direct comparison of the processing efficiency became possible after I have read the publication by B. Lemmerer who adopted the Multiple-Level Tracking (MLT) algorithm devised in (Bovelet & Wiehr 2001) to the segmentation of Hinode images and implemented it in C++ programming language (Lemmerer 2010).

The direct comparison of processing efficiency became possible after reading the publication by B. Lemmerer, who adopted the Multiple-Level Tracking (MLT) algorithm developed in (Bovelet & Wiehr 2001) for the Hinode image segmentation and implemented it using C ++ language (Lemmerer 2010).[65] The main indicators for processing efficiency in this thesis and the work described in (Lemmerer 2010) are summarized in Table 7 for comparison.

Note that the processing “then and now” was carried out on personal computers made in different decades of the 21st century. The computing power of the Intel processor with 1.86 GHZ and 1.5 GB RAM was at least four times weaker than that of the PC used in this work. The Hinode image fragments used in (Lemmerer 2010) were 8 times smaller than the full-screen Hinode images that I processed. In both cases the execution times were fairly

[65] Earlier, T.Roudier implemented the same algorithm using IDL.

comparable, which suggests that the processing efficiency in the present work was higher and the speedup factor reached approximately 1.5 - 2.

Table 7. Indicators of processing efficiency

Parameter	Lemmerer, 2010	Sharov, 2020	Note
PC Processor, CPU	Intel, 1.86 GHz	Intel, 3 GHz	Laptop / Desktop
RAM	1.5 GB	8 GB	no parallel comp.
Programming language	C++	MATLAB	
Input image size, format	512 x 512, FITS	2048 x 1024, TIFF	8-bit pixel depth
Min. execution time, sec	1.77	1.75	one run
Opt. execution time, sec	2.13	2.5	including graphs
Processing date, year	2010	2019	

However, even the efficient processing of image data didn't allow me to process the entire data set, including almost 2500 high-quality Hinode BFI images. This is due to the lack of resources and the additional time for the preparation, graphic display, visual analysis and documentation of the results, which increases rapidly with the number of scenes. Nevertheless, I think that this was the first precedent in the history of Graz University of Technology, when more than eight hundred high-resolution Hinode images were processed by one person in the individual master's study.

5.5 Analysis of perspectives

There remain some ways to improve processing efficiency and optimize processing results. This could be achieved by restructuring the SOGIS software and implementing new options, e.g. for image normalization and lossless filtering.

Keeping in mind the results of cross-correlation analysis, which indicated the approximately 14-day delay in the cause-effect relationship between the SSN and granulometric parameters, it would be interesting to process Hinode image sequences with a cadence of 14 days. This means that the size of new HITS almost doubles compared to HITS-273-basic. The processing efficiency achieved in this work is already sufficient to successfully solve such a task. The next step could be to process the entire data set with almost 2500 high-quality Hinode BFI images. The granulation parameters derived from such a data set should be compared with the daily SSN. Then the cause-and-effect relationship between the SSN and the granulation parameters could be revealed over the entire cycle of sunspot activity.

The processing concept "no filtering and no retouched pictures" accepted in this work should be tolerated so that the filtering is applied to the granulometric results and not to the original images. Both the granulometric and SSN data set should be smoothed by filtering before the correlation analysis. This can weaken the influence of the saw-tooth variability of the signal amplitudes on the results of the correlation analysis.

An improved formulation of the relationship between the sunspot numbers and surface convection activity would be a very welcome result. Further in-depth studies can be performed to determine the influence of Hinode orbital peculiarities on SOT performance and image quality. The author of this work is keen in processing data that should be obtained from other space-based sensors of the Sun. He will be glad to receive any comments on possible improvements of the results obtained and, of course, incentives to greater efforts.

The Parker Solar Probe starts the next solar encounter …

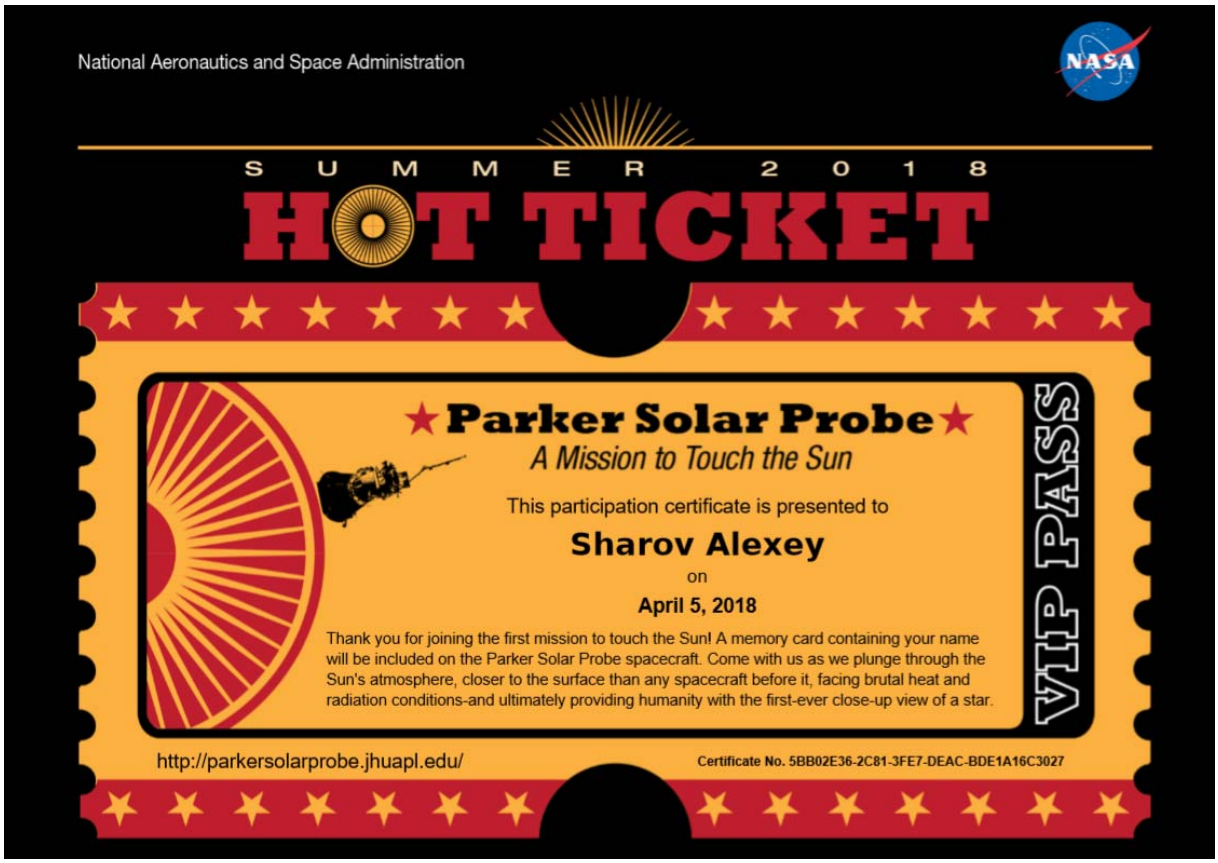

Figure X. Parker Solar Probe: participation certificate presented to the author on 05.04.2018

Conclusions

The master's thesis devoted to studying the variability of solar granulation over the 24th cycle of solar activity has been successfully completed. The main objectives of the study have been achieved and the results obtained have generally met expectations. The main working hypothesis about a significant temporal correlation between the solar granulation scale and the sunspot number index has been positively proven. The unprecedented series of space-borne imagery taken by the Hinode Solar Optical Telescope in 2006 - 2016 and the time series of daily sunspot numbers from the Royal Observatory of Belgium have provided a solid experimental basis and factual material for initial theoretical investigations and complex empirical studies on the dynamic behaviour of solar granulation in relation to sunspot activity.

The study was focussed on the development of an efficient algorithm for the automatic identification of granular cells in the Hinode images, its implementation and practical application to the precise granulometric measurements and the temporal cross-correlation analysis of the results with the SSN time series. This research task is deemed to have been solved and the final results are of practical importance and of particular scientific interest. The main results of the study can be summarized as follows.

1. New in-depth knowledge about the solar surface convection and the dynamic behaviour of solar granulation over an activity cycle was summarized, documented and presented in the form of the present thesis.
2. An initial theoretical study based on the mixing-length theory was carried out and the first analytical formulations showing the inverse proportionality between the local flux of the convective energy and the granular size were written and tested.
3. The definitions of granules and granular cells in the solar surface convection were critically reviewed and the use of granular cells in morphometric measurements was preferred.
4. An efficient marker-controlled watershed (MCW) algorithm for the automatic segmentation and identification of granules and granular cells in the Hinode imagery was designed, implemented, tested and practically applied to the granulometric measurements and analyses.
5. A total of 7 image sequences with 30-, 27- and 1-day cadence, which all contained 710 high-quality Hinode images, were compiled, homogenized, processed and corrected for the variable Sun-Earth distance.
6. The resultant granulation parameters, including mean area, perimeter, equivalent diameter, and contrast were analysed, validated and compared with the monthly and daily SSN using methods of visual control and cross-correlation analysis.
7. A new parameter of granular extent that varies in phase with sunspot activity was introduced and its practical value for solar granulometry was statistically argued.
8. An important scientific question regarding the inverse relationship between the granulation scale and sunspot numbers was positively resolved.
9. The approximately 14-day delay in the cause-and-effect relationship between the SSN and the granulation parameters was revealed with the cross-correlation analysis and a plausible explanation for this delay was given.
10. The processing efficiency of the WCM method was tested and rated as superior compared to the working analogue for the photometric segmentation of solar granulation images.

All in all, the results look very promising and deserve to be published in a per-reviewed journal and/or conference proceedings.

References

Abramenko V. et al. (2012): Detection of small-scale granular structures in the quiet Sun with the new solar telescope. Astrophys. J.Lett. 756:L27, 6 p.

Al-Janabi K. et al. (2019): Achievements of Hinode in the first eleven years. Review. *Publ. Astron. Soc. Japan*, 71 (5), R!, 1-118.

Antia H. & Basu S. (2000): Temporal variations of the rotation rate in the solar interior. *Astrophys. J.,* 541, 442-448.

Arbeláez P. et al. (2010): Contour detection and hierarchical image segmentation. IEEE Trans. PA&MI, 33, 5, 898-916.

Arganda-Carreras I. et al. (2019): MorphoLibJ: integrated library and plugins for mathematical morphology with ImageJ. *Bioinformatics,* 32, 22, 3532–3534.

Balogh A. et al. (2014): Introduction to the solar activity cycle: Overview of causes and consequences. *Space Sci. Rev.* 186, 1-15.

Bahng J. and Schwarzschild M. (1961). Lifetime of Solar Granules. *Astrophys. J.,* vol. 134, p.312-322.

Bartholomew C. (1976): Discovery of the Solar Granulation. *Quart. J. Royal Astron. Soc*., 17, 263-288.

Berdyugina S. & Usoskin I. (2004): Persistent active longitudes on the Sun. In: Strassmeier K. & Washuettl A. (Eds). Sunspots and Straspots. Proc. 1st Potsdam Thinkshop, 31-32.

Berger T., Slater G. (2009): Hinode Solar Optical Telescope: Data analysis guide. V.3.3, 40 p.

Beucher S. (2000): The watershed transformation applied to image segmentation. *Scanning Microscopy*, 1-25.

Bovelet B. & Wiehr E. (2001): A new algorithm for pattern recognition and its application to granulation and limb faculae. *Solar Physics*, 201, 13–26.

Bray R. and Loughed R. (1964): A new determination of the granule/intergranule contrast. Solar Physics, 54, 319–326.

Bruevich E. & Yakunina G. (2013): Correlation study of six solar activity indices in the cycles 21-23. *Sun and Geosphere* 8(2): 83-90.

Cameron R. & Schüssler M. (2015): The crucial role of surface magnetic fields for the solar dynamo. *Science,* 347, 6228, 1333-1335.

Cattaneo F. et al. (2003): On the interaction between convection and magnetic fields. *Astrophys. J.,* 588: 1183–1198.

eoPortal (2019): Solar B / Hinode Mission https://directory.eoportal.org/web/eoportal/satellite-missions/s/solar-b (accessed on 28.11.2019).

Ermolli I. et al. (2014): Solar cycle indices from the photosphere to corona: Measurements and underlying physics. *Space Sci. Rev.* 186, 1-15.

Forsyth D. & Ponce J. (2003): *Computer vision, a modern approach.* Printice Hall.

Gadun A. et al. (2000): Size-dependent properties of simulated 2D solar granulation.*Astron. Astrophys. Suppl. Ser.* 146, 267-291.

Godoli G. & Allen C. (1964): The indices of solar activity. *Planet. Space. Sci*, 12, 349-354.

Gonzales R. & Woods C. (1993): *Digital Image Processing.* Addison-Wesley Publ. 716 p.

Gough D. (2000): Towards understanding solar convection and activity. *Solar Physics*, 192, 3-26.

Hanslmeier A. (2007): *The Sun and Space Weather*. Springer.

Hanslmeier A. et al. (2000): Dynamics of the upper solar photosphere. A&A, v.356, 308-314.

Hanslmeier A. et al. (2006): Observation of turbulence in solar surface convection: line parameter correlations. *Solar Phys.* 249, 293-306.

Hanslmeier A. et al. (2009): Solar convection dynamics derived from long time series observations. *Cent. Eur. Astrophys. Bull.* 33, 1, 39 – 50.

Hanslmeier A. et al. (2010): Hinode –Synoptic observations of convection dynamics. *Cent. Eur. Astrophys. Bull.* 34, 1, 81 – 88.

Hinode review team (2019): Achievements of Hinode in the first eleven years. Review. Publ. Astron. Soc. Japan, 71 (5), R!, 1-118.

Hirzberger J. (2001): Time evolution of solar granulation. In: Rimmele T, Balasubramaniam K., Radick R. (Eds). High resolution solar physics: Theory, observations and techniques. ASP Conf. Series, v.183, 507-514.

Hirzberger J. (2002): On the brightness and velocity structure of solar granulation. *A & A*, 392, 1105-1118.

Hirzberger J. et al. (1999): Granulation in active regions as compared to quiet regions. *Astr. Ges. Abstr. Ser.*, 15, p 88. P02.

Ichimoto K. et al. (2008): Polarization calibration of the Solar Optical Telescope onboard Hinode. *Solar Phys.* 249, 2, 179 – 207.

Jin C-L. et al. (2009): Interaction between granulation and small-scale magnetic flux observed by Hinode. *Res. Astron. Astrophys.* Vol. 9 No. 8, 921 – 932.

Lemmerer B. (2010): Analysis and Segmentation of the Solar Convection. Masterarbeit, KFU-IGAM, 63 p.

Lemmerer B. et al. (2019): Two-dimensional segmentation of small convective patterns in radiation hydrodynamics simulations. *Astronomy & Astrophysics*, 10 p.

Livingston W. (1983): Magnetic Fields and Convection. In: Solar and stellar magnetic fields: origins and coronal effects. New Obs. Symp. – Int. Astron. Union, v 102, 149-153.

Macris C. et al. (1983): Variation of the mesh of the granular network along the solar cycle. In: S. Keil (Ed.) Small-Scale Dynamical Processes in Quiet Stellar Atmospheres. Proc. Conf. p. 265.

MathWorks (2019): Marker-Controlled Watershed Segmentation. MATLAB, Open Live Script, https://de.mathworks.com/help/images/marker-controlled-watershed-segmentation (accessed 09.09.2019).

McClure R., Rast M. and Pillet V. (2018): Doppler events in the solar photosphere: The coincident superposition of fast granular flows and p-mode coherence patches. *Solar Physics*, 10 p. DOI: 10.1007.

Meyer F. (1994): Topographic distance and watershed lines. *Signal Processing* 38, 113-125.

Meyer F. & Beucher S. (1990): Mosrphological segmentation. *JVCIR*, v.1, 1, 21-46.

Müller D. et al. (2001): Time-slice diagrams of solar granulation. *Solar Physics* 203, 211-232.

Muller R. (1989): Observations of the solar granulation at the Pic du Midi Observatory and with THEMIS. In: Rutten R. and Severino g. (Eds.). Solar and stellar granulation. Kluwer, 9-12.

Muller R. (1989): Solar granulation: Overview. In: Rutten R. and Severino g. (Eds.). Solar and stellar granulation. Kluwer, 101-123.

Muller R., Hanslmeier A. and M. Saldaña-Muñoz (2007): Variations of the granulation related to the solar cycle and with respect to its position on the solar disk. *A&A*, v.475, 2, 717-722.

Muller R., Hanslmeier A. and D.Utz (2017): Latitude dependence of the solar granulation during the minimum of activity in 2009. *A&A,* 598, A6, 9 p.

Muller R., Utz D. and A. Hanslmeier (2011): Non-Varying Granulation and Photospheric Network During the Extended 2007 – 2009 Solar Minimum. Solar Physics, 274, 87–97.

Muller R., Hanslmeier A. and Utz D. (2017): Latitude dependence oft he solar granulation during the minimum activity in 2009. *Astron. & Astrophys.* 598, A6, 9 p.

Muller R. et al. (2018): Does the solar granulation change with the activity cycle? *A&A* 616, A87, 6 p.

Muller R. & Roudier Th. (1984): Variability of the quiet photospheric network. *Solar Physics*, volume 94, 33–47.

Nelson G. & Musman S. (1978): The scale of solar granulation. *Astrophys. J.,* 222, L69-L72.

Noever D. (1994): Solar granulation and statistical crystallography: a modelling approach using size-shape relations. *A & A*, 282, 252-261.

Nordlund A., Stein R., Asplund M. (2009) Solar surface convection. Living Rev. Solar Phys. 6, 2, 1-117.

Pevtsov A. et al. (2011): Long-term trendas in sunspot magnetic fields. Astrophys. J.Lett., 742:L36, 4 p.

Pötzi W., Hanslmeier A.and Brandt P.(2000). Granular evolution from2D(X,T)-slices and from tracking granules. In: The Solar cycle and Terrestrial climate. Proc.1st Solar& Space Weather Euroconference. ESA SP 463, 407-410.

Pötzi W. (2009): Granulation properties in DOT images from solar maximum to minimum. *Cent. Eur. Astrophys. Bull.* 33, 1, 59 – 68.

Roudier Th. et al. (2018): Structure and evolution of solar supergranulation using SDO/HMI data. *A&A*, 'roudier'2014.

Roudier Th. & Muller R. (1986): Structure of the solar granulation. *Solar Physics*, 107, 11-26.

Sakurai T. (Ed.) (2008): The Hinode Mission. *Solar Physics*, 249, Issue 2, 1-26.

Saldaña-Muñoz M., Muller R. and A.Hanslmeier (2004): Variation of the solar granulation structure with the solar activity cycle. *Hvar Observatory Bulletin*, vol. 28, no. 1, 9-17.

Schrijver C. et al. (1997): Modeling the distribution of magnetic fluxes in field concentrations in a solar active region. *Solar Physics*, volume 175, 329–340.

Sonka M., Hlavac V. and R.Boyle (1999): Image Processing, Analysis, and Machine Vision. 2nd Edition. Brooks/Cole, PWS Publishing, 770 p.

Schüssler M. (2002): Solar Convection & Magnetism. IMPRS Intro Course, Germerode, 49 p.

Spiegel E. & Weiss N. (1980): Magnetic activity and variations in solar luminosity. *Nature*, volume 287, 616–617.

Sharov A., Gutjahr K. (2001): Some methodological enhancements to INSAR surveying of polar ice caps. In: G.Begni (Ed). Observing our environment from space. Proc. 21st EARSeL Symp., Balkema Publishers, p. 65 – 72.

Sharov A. et al. (2002): Methodical alternatives to the glacier motion measurement from differential SAR interferometry. IAPRS, XXXIV, v.3A, 324 – 329.

Shimizu T. (2008): Image stabilization system for Hinode (Solar-B) Solar Optical Telescope. *Solar Physics*, volume 249, 221–232.

Shimojo M. (2006): The list of SOLAR-B "Hinode" mission-wide FITS keywords. V. 1.3. NAOJ, 34 p.

Spruit H., Nordlund A. and Title A. (1990): Solar convection. *Ann. Rev. Astron. Astrophys*. 28: 263-301.

Stein R. (2012): Magneto-convection. *Phil. Trans. R.Soc*., 370, 3070-3087.

Szelisky R. (2011): *Computer Vision: Algorithms and Applications, Texts in Computer Science*. Springer, London.

Takayoshi O. (2018): Three-dimensional convective velocity fields in the solar photosphere. PhD Dissertation. SOKENDAI, 119 p.

Tsuneta S. et al. (2008): The Solar Optical Telescope for the Hinode Mission: An Overview. Solar Physics, volume 249, 167–196.

Yu D. et al. (2011): Physical properties of large and small granules in quiet Sun regions. Astrophys. J., 734:58, 10 p.

Veronig A. (2019): *Data processing in solar and space physics*. Parts A1 / A2. IGAM, 98 p.

Wedemeyer-Böhm S. (2008): Point spread functions for the Solar Optical Telescope onboard Hinode. *Astronomy & Astrophysics*, No.09819, 16 p.

Working Document (1983): The Physics of activity cycles and the dynamical behaviour of the convection zone. In: Challenges to Astronomy and Astrophysics. Working Document, 22-24.

Zaqarashvili T. et al. (2015): Long-term variation in the Sun's activity caused by magnetic Rossby waves in the tachocline. *Astrophys. J. Lett.* 805:L14, 5 p.

Zirin H. (1988): High-resolution continuum observations of the Sun. In: Theoretical problems in high-resolution solar physics, NASA-Goddard Flight Centre, 2, 79-88.

Annex A: SOGIS Source Code written in MATLAB

```
% Solar Granulation Image Segmentation (SOGIS): September 2019 - March 2020
% by Alexey Sharov, MNr. 09330221; Master's Thesis on "SOLAR GRANULOMETRY"

%     ---------------------------------------------------------------------
%   |         Project SolCon, KFU Graz @ TU Graz                          |
%   |             aleksey.sharov@joanneum.at                              |
%    ---------------------------------------------------------------------

clearvars
close all
clc

% profile on % performance profiling

tic

% 0.1 Data path definition / File Folder Contents
% bVerbose = true;        % code generation stage

fileFolder = 'D:\DIPLOMA\HITS_2011_1234\';
dirOutput = dir(fullfile(fileFolder,'*.tif'));
fileNames = {dirOutput.name}; % list folder contents
numFrames = numel(fileNames);

FileRange = 1:numFrames;
% FileRange = 1:2; % selecting files (change it here)

for FileID = FileRange
   Caption{FileID} = fileNames{FileID}(3:10);
end

% Image Batch Processing (HINODE image time series = HITS)

for FileID = FileRange

   tic                                                  % time count

% 1. Read in the *.tif Image and convert it to Grayscale
% I = imread('D:\DIPLOMA\HITS_27_OK_tiff\FG20160217_204344.8.tif');

I = imread(fullfile(fileFolder,fileNames{FileID}));
% figure
% imshow(I,[]), title('HINODE FG-image No...');

   % 2. Gradient Magnitude as the Segmentation Function (MathWorks 2019)
   hy = fspecial('sobel');
   hx = hy';
   Iy = imfilter(double(I), hy, 'replicate');
   Ix = imfilter(double(I), hx, 'replicate');
   gradmag = sqrt(Ix.^2 + Iy.^2);
   % figure
   % imshow(gradmag,[]), title('Gradient magnitude (gradmag)');
   % Direct segmentation of gradmag produces 'over-segmentation'

   % 2.1 Enhance Contrast (switched off due to “no filtering” concept)
   % Improve the intensity contrast of the gradient image using
   % contrast-limited adaptive histogram equalization. Rescale the
```

```
   % image intensity with IMADJUST which fills the data type's entire
   % dynamic range.
   % gradmage = adapthisteq(gradmag,'NumTiles',[10 10]);
   % gradmage = imadjust(gradmage);
   % imshow(gradmage,[]), title('Gradient magnitude enhanced (gradmage)');

   % 3. Mark the Foreground Objects

   % See (MathWorks 2019): Open Live Script
   % https://de.mathworks.com/help/images/marker-controlled-watershed-
   % segmentation.html;jsessionid=f6e06bc3f6eba0c66477b9488389
   % 3.1 Opening = erosion followed by dilation
   se = strel('disk', 1);
   Io = imopen(I, se);
   % figure
   % imshow(Io), title('Opening (Io)');

   % 3.2 Opening-by-reconstruction (erosion followed by morphological
   % reconstruction; the result is not good)
   Ie = imerode(I, se);
   Iobr = imreconstruct(Ie, I);
   % figure
   % imshow(Iobr), title('Opening-by-reconstruction (Iobr)')

   % 3.3 Regular morphological closing
   % Opening & Closing can remove the dark spots and bright marks.
   Ioc = imclose(Io, se);
   % figure
   % imshow(Ioc), title('Opening-closing (Ioc)')

% 3.4 Opening-closing by reconstruction

   Iobrd = imdilate(Iobr, se);
   Iobrcbr = imreconstruct(imcomplement(Iobrd), imcomplement(Iobr));
   Iobrcbr = imcomplement(Iobrcbr);
   % figure
   % imshow(Iobrcbr), title('Opening-closing by reconstruction (Iobrcbr)')

   % Reconstruction-based opening and closing are more effective than
   % standard opening and closing at removing small blemishes without
   % affecting the overall shapes of the objects (Mathworks 2019).

% 3.5 Calculate the regional maxima of Iobrcbr to obtain foreground markers
   % fgm = imregionalmax(Iobrcbr);
   % figure
   % imshow(fgm), title('Regional maxima of opening-closing by
reconstruction (fgm)')

   % 3.6 Superimpose the foreground marker image on the original image
   % I2 = I;
   % I2(fgm) = 255;
   % figure
   % imshow(I2), title('Regional maxima superimposed on original image
(I2)')

   % Some of the mostly-occluded and shadowed objects are not marked.
   % These objects will not be segmented properly in the end result.
   % The foreground markers in some objects go right up to the objects'
   % edge. Clean the edges of the marker blobs and then shrink them a bit.
```

```
% 3.7 Closing followed by an Erosion (optionally)
% se2 = strel(ones(3,3));
% fgm2 = imclose(fgm, se2);
% fgm3 = imerode(fgm2, se2);

% This procedure leaves isolated pixels that must be removed.
% Do this using bwareaopen, which removes all blobs that have fewer
% than a certain number of pixels, e.g. 5.
% fgm4 = bwareaopen(fgm3, 5);
% I3 = I;
% I3(fgm4) = 255;
% figure
% imshow(I3),
% title('Modified regional maxima superimposed on original image (fgm4)')

% 4. Compute Background Markers
% In the cleaned-up image, Iobrcbr, dark pixels belong to background,
% Now I start with a thresholding operation: bgr pixels are in black.
bw = imbinarize(Iobrcbr);
% figure
% imshow(bw), title('Threshold opening-closing by reconstruction (bw)')

% 4.1. Edge detection on bw
edgebw = edge(bw, 'canny');
% figure
% imshow(edgebw), title('Edge detection on bw (edgebw)')

% 4.2 Rejecting bw regions which touch the frame
bwc = imclearborder(bw);
% figure
% imshow(bwc), title('Thresholded ocr with clear borders (bgmic)')

% I"thin" the background by computing  % the "skeleton by influence
% zones", or SKIZ, of the foreground of bw.

% 5. Computing the watershed transform of the distance transform of bw,
% watershed ridge lines (DL == 0, MathWorks 2019)
D = bwdist(bw);
DL = watershed(D);
bgm = DL == 0;
% figure
% imshow(bgm), title('Watershed ridge lines (bgm)')

% 5.1 Inverting watershed image
bgmi = (~bgm);
% figure
% imshow(bgmi), title('Inverted watershed ridge lines (bgmi)')

% 5.2 Rejecting regions which touch the frame
bgmic = imclearborder (bgmi);
% figure
% imshow(bgmic), title('Inverted watershed with clear borders (bgmic)')

% 5.2 Overlaying original image (I) with watersheds (bgm)
imgResultR = I;
imgResultG = I;
imgResultB = I;
imgResultR(bgm) = 255;
imgResultG(bgm) = 0;
imgResultB(bgm) = 0;
```

```
   imgResult1 = cat(3,imgResultR,imgResultG,imgResultB);
   % figure
   % imshow(imgResult1,[]); title('Resultant segmentation (bgm)');

   % 5.1 Overlaying original image (I) with Canny edges (edgebw, optional)
   % imgResultR = I;
   % imgResultG = I;
   % imgResultB = I;
   % imgResultR(edgebw) = 0;
   % imgResultG(edgebw) = 255;
   % imgResultB(edgebw) = 255;
   % imgResult2 = cat(3,imgResultR,imgResultG,imgResultB);
   % figure
   % imshow(imgResult2,[]); title('Resultant segmentation (edgebw)');

   % 6. Compute the Watershed Transform of the Segmentation Function.
   % The image can be modified so that it has regional minima only in %
certain desired locations. Here you can use
   % imimposemin to modify the gradient magnitude image so that its only
   % regional minima occur at foreground and background marker pixels.

% gradmag2 = imimposemin(gradmag, bgm | fgm4);

   % Finally we compute the watershed-based segmentation (fewer regions).
   L = watershed(gradmag); % L = watershed(gradmag2);
   mbgm = L == 0;

   % 6.1 Overlaying original image (I) with watersheds (L), optionally
   % imgResultR = I;
   % imgResultG = I;
   % imgResultB = I;
   % imgResultR(mbgm) = 0;
   % imgResultG(mbgm) = 255;
   % imgResultB(mbgm) = 255;
   % imgResult = cat(3,imgResultR,imgResultG,imgResultB);
   % figure
   % imshow(imgResult,[]), title('Resultant segmentation (mbgm)')

   % 7. Visualizing the result (switched-off to reduce the execution time)
   % 7.1 Superimposing foreground and background markers, and segmented
   % object boundaries on the original image. I use dilation as needed to
   % make certain aspects, such as the object boundaries, more visible.
   % Object boundaries are located where L == 0.
   % I5 = I;
   % I5(imdilate(L == 0, ones(3, 3)) | bgm | fgm4) = 255;
   % figure
   % imshow(I5)
   % title('Markers and object boundaries superimposed on original image
(I5)')

   % This visualization illustrates how the locations of the fg and bg
   % markers affect the result. In a couple of locations, partially
   % occluded darker objects were merged with their brighter neighbouring
   % objects because occluded objects did not have foreground markers.

   % 7.2 Visualization by displaying the label matrix as a colour image.
   % Label matrices, such as those produced by watershed and bwlabel,
   % can be converted to truecolor images by using label2rgb
   % Lrgb = label2rgb(L, 'jet', 'w', 'shuffle');
   % figure
   % imshow(Lrgb), title('Coloured watershed label matrix (Lrgb)')
```

```
   % 7.3 Using transparency to superimpose the pseudo-colour label matrix
   % on top of the original intensity image (MathWorks 2019).
   % figure
   % imshow(I)
   % hold on
   % himage = imshow(Lrgb);
   % himage.AlphaData = 0.3;
   % title('Lrgb superimposed transparently on original image')

   % 8 Measuring region properties of segmented image
   % 8.1 Using bw
   % [La, Num] = bwlabeln(bw);
   % RegProp = regionprops(bw, 'area', 'equivdiameter', 'extent',
'perimeter', 'pixelidxlist');

   % RegPropEdge = regionprops(edgebw, 'area', 'extent', 'perimeter');
   % ME = mean(RegPropEdge)

   % 8.2 Using bgmi (inverted bgm)
   [Lw, Num] = bwlabeln(bgmi);
   RegPropW = regionprops(bgmi, 'area', 'equivdiameter', 'extent',
'perimeter', 'pixelidxlist');
   % PAR = [RegPropW.Perimeter]/[RegPropW.Area]
   % PAR = struct(RegPropW.Perimeter/RegPropW.Area);
   % hFig = figure;
   % imshow(Lw,[]);
   % impixelinfo(hFig);

   for RegionN = 1:numel(RegPropW)
      % Determining contrast of each granule as std
RegPropW(RegionN).Contrast= std(double(I(RegPropW(RegionN).PixelIdxList)));
   end

% 9. Getting data from RegProp structure structName.fieldName into matrix
   RegPropWM.Area(FileID) = mean([RegPropW.Area]);
   RegPropWM.EquivDiameter(FileID) = mean([RegPropW.EquivDiameter]);
   RegPropWM.Extent(FileID) = mean([RegPropW.Extent]);
   RegPropWM.Perimeter(FileID) = mean([RegPropW.Perimeter]);
   RegPropWM.Contrast(FileID) = mean([RegPropW.Contrast]);

   % Calculating Perimeter to Area Ratio
   MPAR(FileID) = mean([RegPropW.Perimeter])/mean([RegPropW.Area]);

   % 10. Seasonal correction due to variable Earth-Sun distance (R)
   % 10.1 Re-Determining time system
   tf = isdatetime(Caption(FileRange)); % Caption is not a datetime array!

   % Determining Matlab datetime for data takes (FileID);
   dt(FileID) = datetime(datetime(str2double(Caption{FileID}(1:4)),...
   str2double(Caption{FileID}(5:6)), str2double(Caption{FileID}(7:8))));
   tt = isdatetime(dt); % dt is a datetime array!

   % Determining Julian Day / No. of days since noon UTC 24-Nov-4714 BCE
   JD(FileID) = juliandate(datetime(str2double(Caption{FileID}(1:4)),...
   str2double(Caption{FileID}(5:6)),str2double(Caption{FileID}(7:8))));

   % Determining JD for the HINODE Epoch of 20060104_1530 (perihelion)
   t1 = datetime('2006-01-04'); %
   % jd1 = juliandate(t1);  % pday = 345.0
```

```
    jd1 = juliandate(t1); % Julian Day

    % Return the number of days since January 0, 0000.
    DN(FileID) = datenum(dt(FileID));

    % Return the number of days since the perihelion Epoch of Jan. 4, 2006
    DNE(FileID) = JD(FileID)-jd1; % Day number counted from the epoch

    % Sun - Earth distance (HINODE Epoch: 2006-01-04, first perihelion date)
    % R = a(1-e*e)/(1+e*cos(nu))= 1.49558/(1+0.0167*cos(nu));
    % a = 1.496*10^11 [m] = 1 AU - semi-major axis; e = 0.0167 eccentricity
    % FileID = 1 (20061215_1613) perihelion: 20060104_1530; R = 0.9833270 AU
    % FileID = 2 (20070111_2204) perihelion: 20070103_1943; R = 0.9832602 AU
    % pday = 345.0; % time in days since perihelion for the first scene
    % pday = 8.1;    % time in days since perihelion for the second scene
    % nu = 2*pi/360*pday*360/365.25 in [degrees] = 2*pi*pday*0.98656
    % nu = pi/180*0.9856*((FileID - 1)*27.3 + pday); % true anomaly;
    nu = pi/180*0.9856*DNE(FileID);
    R(FileID) = 0.99721/(1+0.0167*cos(nu));

    % Calculating corrected region properties (for the Sun-Earth distance)
    RegPropWMR.Area = [RegPropWM.Area] .* R;
    RegPropWMR.EquivDiameter = [RegPropWM.EquivDiameter] .* R;
    RegPropWMR.Extent = [RegPropWM.Extent] .* R;
    RegPropWMR.Perimeter = [RegPropWM.Perimeter] .* R;
    RegPropWMR.Contrast = [RegPropWM.Contrast] .* R;

    % 11. Control by differencing
    % C1 = imsubtract(imgResult2,imgResult);
    % figure
    % imshow(C1, []), title('Difference (edgebw - mbgm)');
      C2 = imsubtract(bgmic,bwc);
    % figure
    % imshow(C2), title('Difference (bgmic - bwc)');

end % for FileID = 1:numel(fileNames)

toc

% 12. Plotting mean properties (area, eq. diameter, extent, perimeter)
figure;
Plot_A = plot(FileRange, RegPropWM.Area(FileRange),'r-');
title('Granulometric Characteristics: Area');
ylabel('Mean Area')
hold on;
% Plot_d = plot(FileRange, RegPropWM.EquivDiameter, 'b-');
% title('Granulometric Characteristics: Equivalent diameter');
% ylabel('Mean Diameter')
% Plot_p = plot(FileRange, RegPropWM.Perimeter, 'g-');
% xlabel('Date')

figure;
Plot_AR = plot(FileRange, RegPropWMR.Area(FileRange),'r-');
title('Granulometric Characteristics: Corrected Area');
ylabel('Mean Area')
% hold on;

% Why gca - continuous axes?
set(gca,'XTick',FileRange);
set(gca,'XTickLabelRotation',60)
xticklabels(Caption(FileRange))
```

```
figure;
Plot_PAR = plot(RegPropWM.Perimeter(FileRange),
RegPropWM.Area(FileRange),'r*');
title('Granulometric Characteristics: MA vs MP');
xlabel('Mean Perimeter, [pix]')
ylabel('Mean Area')

% 12.1 Plotting region properties vs Region ID
% figure
% Plot_reg = plot(FileRange, RegPropW.Extent, 'b-');

% 12.2 Plotting Sun Spot Numbers (SSN)
% ds = datastore('D:\DIPLOMA\SSN\SSN_1996_2019_ed.txt');
% ds_104 = datastore('D:\DIPLOMA\SSN\SSN_273_noadd.txt');
% ds_month_mean =
datastore('D:\DIPLOMA\SSN\SSN_monthly_mean_1995_2019.txt');
% ds_month_smooth =
datastore('D:\DIPLOMA\SSN\SSN_monthly_smooth_1995_2019.txt');
% ds_ms_104 = datastore('D:\DIPLOMA\SSN\SSN_ms_2006_2016_104_ed.txt');
% dsd = datastore('D:\DIPLOMA\SSN\SSN_012012_Daily.txt');
% dsd_02 = datastore('D:\DIPLOMA\SSN\SSN_022012.txt');
% dsd_123 = datastore('D:\DIPLOMA\SSN\SSN_Q2012_Daily.txt');
dsd_1234 = datastore('D:\DIPLOMA\SSN\SSN_2011_1234.txt');

% SSN = read(ds);
% SSN_104 = read(ds_104);
% SSN_m = read(ds_month_mean);
% SSN_ms = read(ds_month_smooth);
% SSN_ms_104 = read(ds_ms_104);
% SSN_30 = read(dsd);
% SSN_31 = read(dsd_02);
SSN_1234 = read(dsd_1234);

% figure;
% Plot_SSN_r = plot(SSN.Var4,SSN.Var5, 'r-');
figure;
Plot_SSN1234 = plot(SSN_1234.Var4,SSN_1234.Var5, ':r*');

% 12.3 Plotting SSNms+50 and SSN+50 vs MAR, MEDR et al.
% figure;
% Plot_MAvsSSN123 = plotyy(DNE,RegPropWM.Area(FileRange),DNE,SSN_123.Var5);
figure;
Plot_MARvsSSN1234 =
plotyy(DNE,RegPropWMR.Area(FileRange),DNE,SSN_1234.Var5);
figure;
Plot_MEDRvsSSN1234 =
plotyy(DNE,RegPropWMR.EquivDiameter(FileRange),DNE,SSN_1234.Var5);
figure;
Plot_CONvsSSN1234 =
plotyy(DNE,RegPropWM.Contrast(FileRange),DNE,SSN_1234.Var5);
figure;
Plot_EXTRvsSSN1234 =
plotyy(DNE,RegPropWMR.Extent(FileRange),DNE,SSN_1234.Var5);
figure;
Plot_MPARvsSSN1234 = plotyy(DNE,MPAR(FileRange),DNE,SSN_1234.Var5);

% 12.4 Making scatterplot MAR(var-mean) vs SSN(var - mean)
MA = mean(RegPropWMR.Area(FileRange));
```

```
MSSN = mean(SSN_1234.Var5);

figure;
Plot_Scat1234M = plot(RegPropWMR.Area(FileRange)-MA,SSN_1234.Var5-MSSN,
'b*');

figure;
Plot_Scat1234 = plot(RegPropWMR.Area(FileRange),SSN_1234.Var5, 'b*');

% 13. Calculating correlation coefficient R
R = corrcoef(SSN_1234.Var5,RegPropWMR.Area);

% 14. Calculating and plotting normalized cross-correlation btw. MAR - SSN
r = xcorr(SSN_1234.Var5,RegPropWMR.Area(FileRange),'coeff');
figure;
Plot_xcorr1234 = plot(r,':b*');

% [r,lags] = xcorr(SSN_1234.Var5,RegPropWMR.Area(FileRange),'coeff');

% -------------------------------- EOF ------------------------------------

% profile viewer

% 15. Calculating correlation coefficients as a function of lag btw SSN-MAR
   LagRange = floor(numel(DNE)/2);
   CorrCoeff = nan(1,LagRange);

   MeanArea = mean(RegPropWMR.Area);

   for Lag = 0:LagRange-1

  % padded with last value of series
  % Area = [RegPropWMR.Area(Lag+1:end),RegPropWMR.Area(end) * ones(1,Lag)];

      % padded with zeros
      % Area = [RegPropWMR.Area(Lag+1:end),zeros(1,Lag)];

      % padded with mean value of series
      Area = [RegPropWMR.Area(Lag+1:end), MeanArea * ones(1,Lag)];

      Coeff = corrcoef(SSN_1234.Var5,Area);
      CorrCoeff(Lag+1) = Coeff(1,2);
   end

% Plot CorrCoeff manually from the list of variables

   % --------------------------------EOF-----------------------------------

   % --------------------------------LIBRARY-------------------------------

% NormOpt = 'normalized'; % default 'none'
% r = xcorr(SSN_1234.Var5,RegPropWMR.Area(FileRange),NormOpt);

% Legend: executables, input parameters, comments
```

Annex B. Additional graphs of granulation parameters

This section contains additional graphs and tables that have no place in the main text of the work, but can be useful for checking, validating and reproducing the main results.

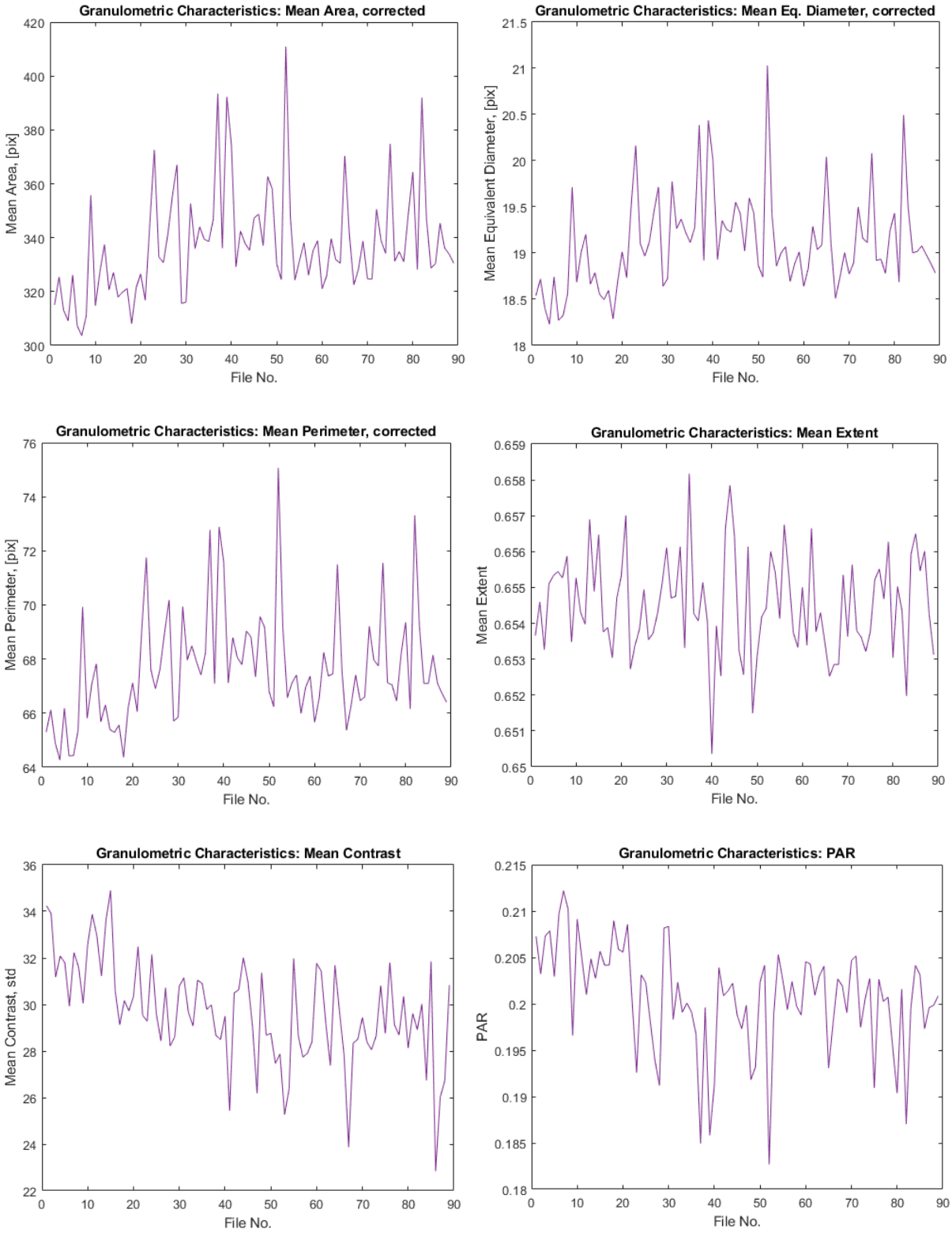

Figure A. Granulometric characteristics of the corrected HITS-30-other time series including mean area, perimeter and contrast in the left column and mean equivalent diameter, extent and perimeter-to-area ratio in the right column

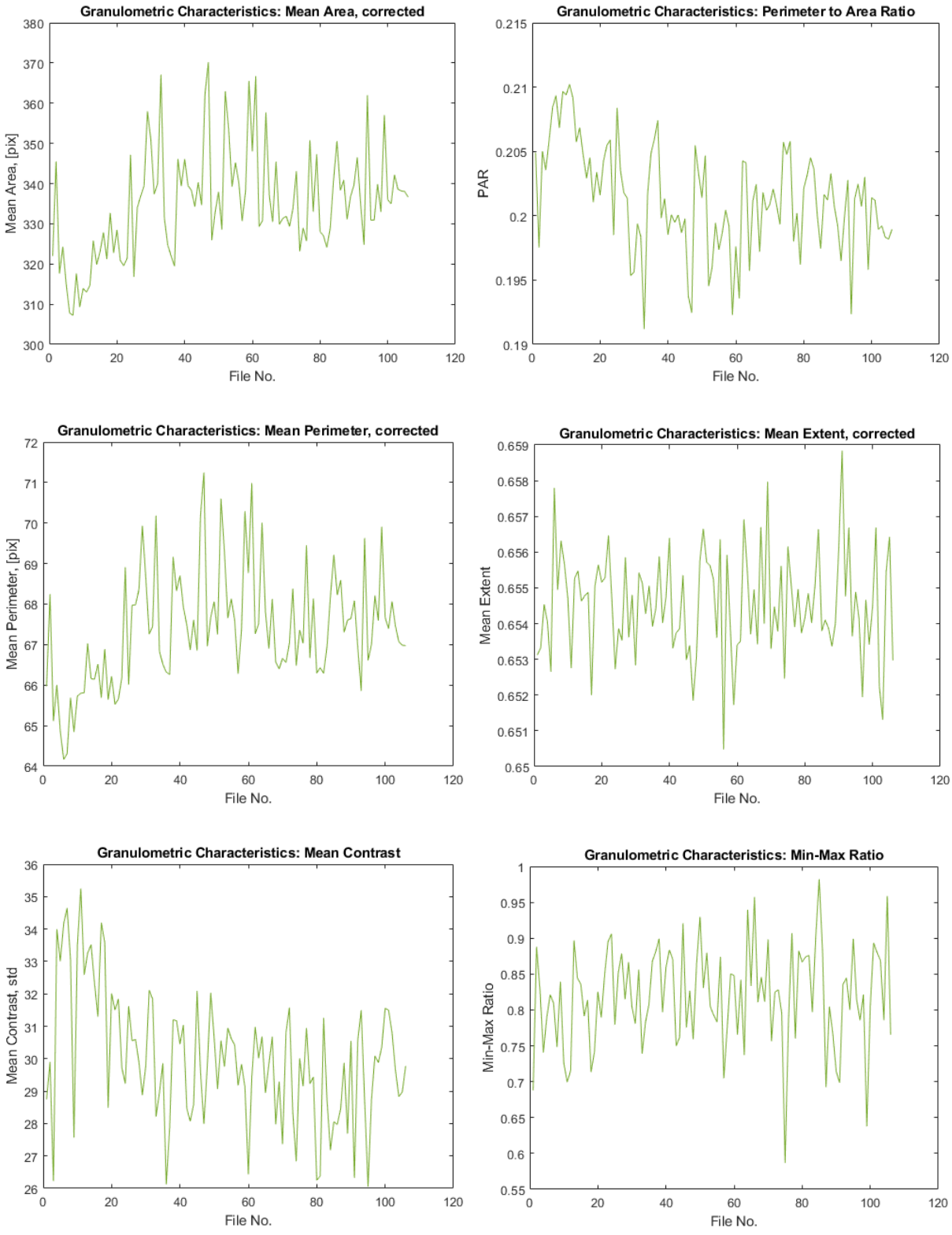

Figure B. Temporal behaviour of the mean granulometric properties in the corrected HITS-273-other time series with the mean area, perimeter and contrast in the left column; PAR, mean extent and min-max ratio in the right column

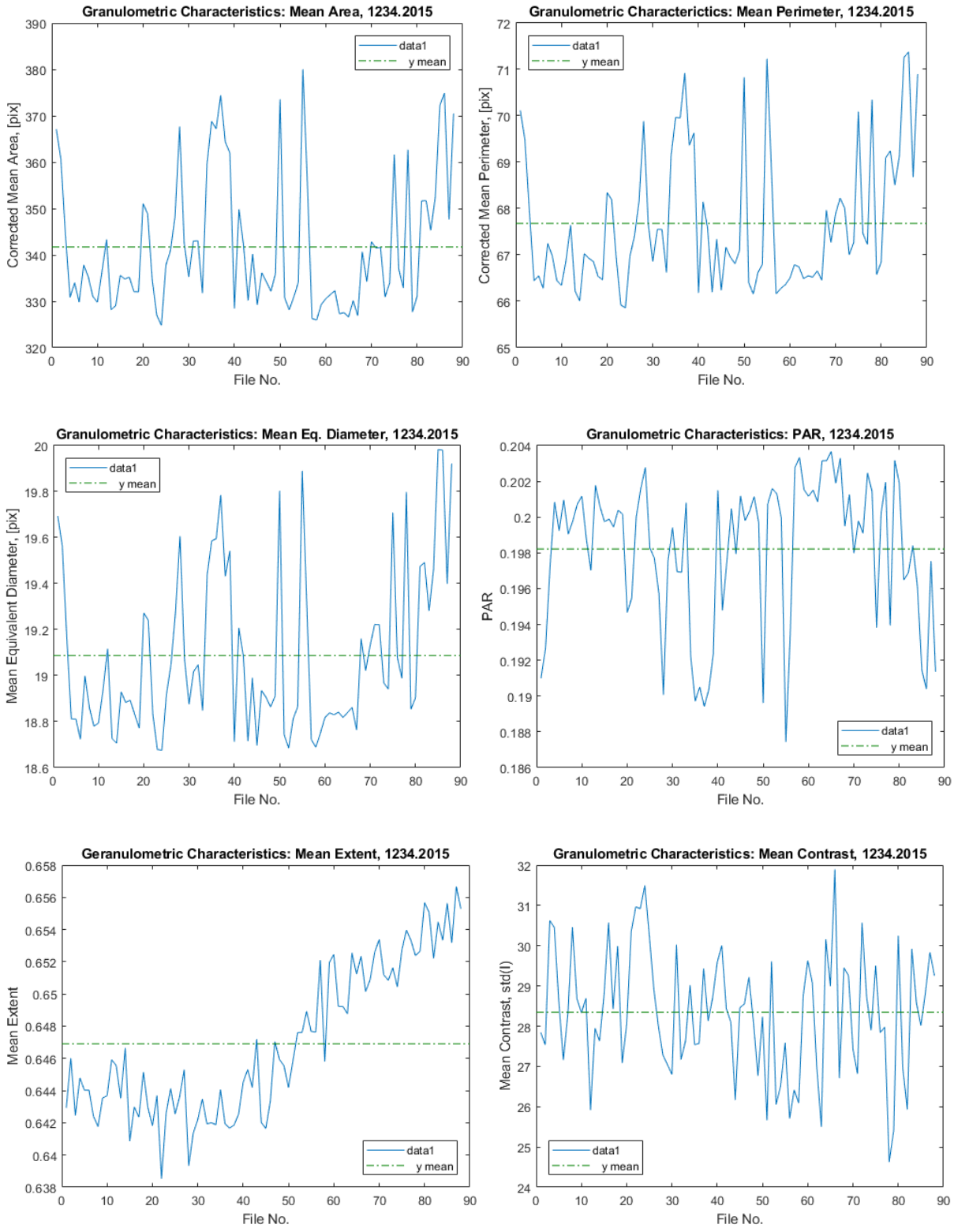

Figure C. Corrected morphometric parameters of granular cells derived from the daily HITS-2015-1234: mean area, perimeter, equivalent diameter, PAR, extent and contrast.

Full version of Table 6. Mean morphometric parameters of solar granulation [1 pixel = 0.104”]

Mean area, pixel	Peak area, pixel	Mean D_e, pixel	Peak D_e, pixel	Mean perim. pixel	Peak perim. pixel	PAR	Mean extent	Peak extent	Mean contr.
Granular cells, synodic and monthly HITS									
340		19.1		68.1		0.200	0.654		29.7
345		19.2		68		0.201	0.6545		30
339		19.1		67.8		0.200	0.6545		30.1
338		19.2		67.7		0.200	0.655		30
340*	100	19.2	12	67.9	40	0.200	0.6545	0.66	30.0
Granular cells, daily HITS									
348		19.3		68.6		0.197	0.648		29.3
336		19.0		67.1		0.200	0.644		29.1
342		19.1		67.7		0.198	0.647		28.4
342	100	19.1	12	67.8	50	0.198	0.646	0.68	28.9
Granules, synodic HITS									
162	30	12.7	5	53.8	20	0.332	-	0.60	15.5

*) Averages of mean values are given in red

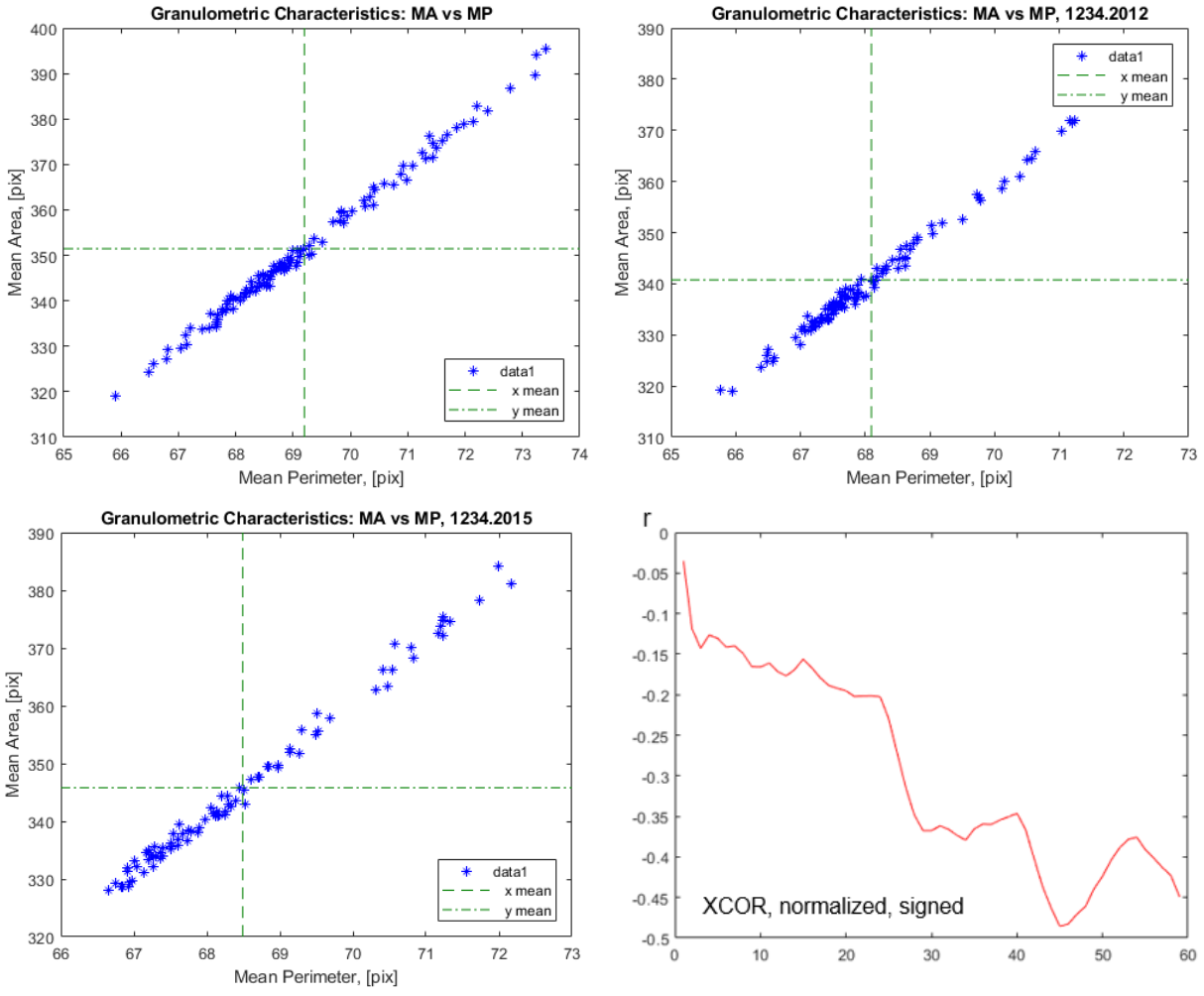

Figure D. Scatterplots of mean area vs mean perimeter in the daily HITS and inverted XCOR function for the SSN and GTS-A time series of 1234.2012 (bottom right)

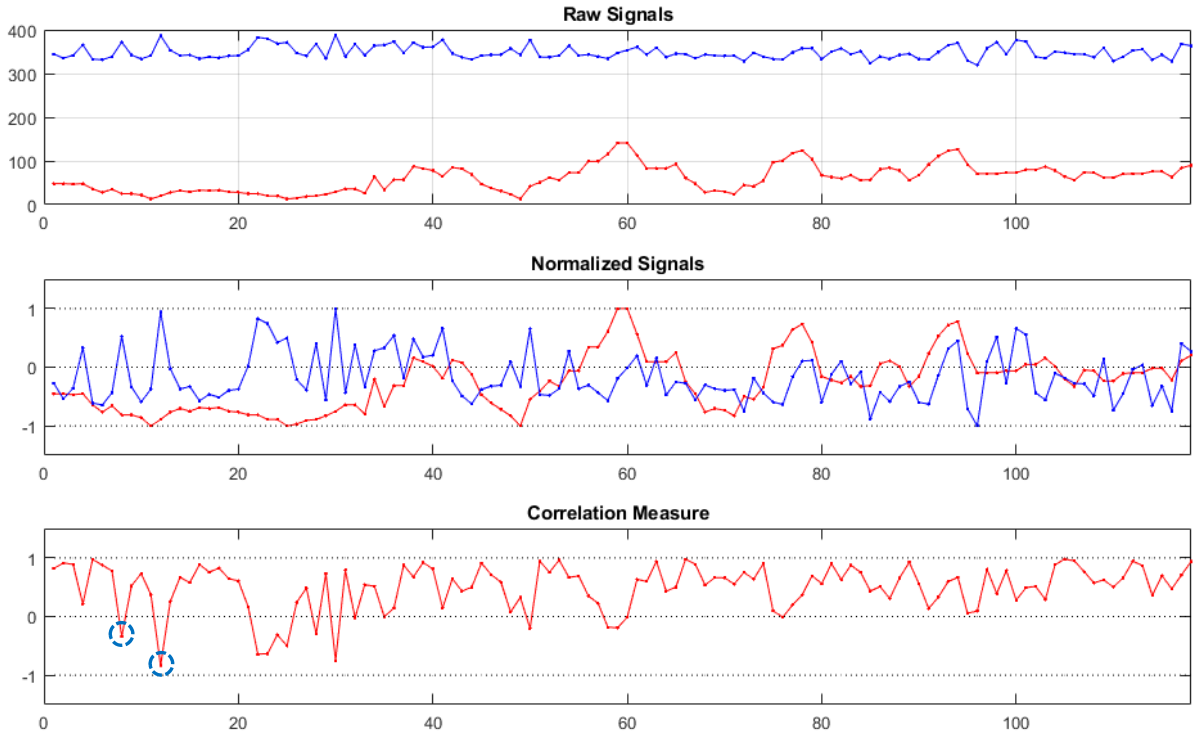

Figure E. Cross-correlation between the aligned SSN (red) and GTS-A (blue) time series of 1234.2011: original signals (top), normalized signals (mid) and correlation measure (bottom). Blue circles indicate two first negative extremes in the correlation measure.